APPLICATION OF A TWO-LEVEL TARGETER FOR LOW-THRUST SPACECRAFT TRAJECTORIES

A Thesis

Submitted to the Faculty

of

Purdue University

by

Collin E. York

In Partial Fulfillment of the

Requirements for the Degree

of

Master of Science in Aeronautics and Astronautics

December 2018

Purdue University

West Lafayette, Indiana

THE PURDUE UNIVERSITY GRADUATE SCHOOL
STATEMENT OF THESIS APPROVAL

Professor Kathleen C. Howell, Chair
School of Aeronautics and Astronautics
Dr. Christopher N. D'Souza
NASA Johnson Space Center
Professor Belinda Marchand
School of Aeronautics and Astronautics
Professor David A. Spencer
School of Aeronautics and Astronautics
Professor Carolin E. Frueh
School of Aeronautics and Astronautics

Approved by:

Professor Weinong Wayne Chen
Aeronautics and Astronautics Associate Head for Graduate Education

For my wife, Caroline, who inspires me every day.

ACKNOWLEDGMENTS

First, I must thank my wife, Caroline, for her endless love and support. When I had the crazy idea to change careers and, in the process, our lives, you immediately encouraged me to take the plunge. That encouragement never wavered as time passed, and it never faltered when I had to travel to Houston for months out of the year. I attribute my accomplishments to you just as much as myself.

I owe a significant debt of gratitude to my parents, Terry and Joy, who instilled in me the value of education from the very beginning. Thank you for encouraging me to explore my passions. Thank you for reading that first book on space to me over and over again. Thank you for always believing in me and teaching me to never stop believing in myself. Thank you.

I would also like to thank my advisor, Professor Kathleen C. Howell. Thank you for welcoming me into your research group and for your mentorship over the past two years. Your technical insight and motivation to obtain a deeper understanding of the problem contributed significantly to my research and the way that I approach my work.

Of course, many thanks go to the members of my research group. I appreciate your support and willingness to answer questions over the years. The friendship and exchange of ideas that you provided were invaluable to me. Thank you, Brian McCarthy, for being a truly incredible friend. While I am not sure they really will give each of us half of a diploma, I am thankful that we shared in this experience together.

In addition, I am grateful for the contributions of my committee members. I thank Dr. Christopher D'Souza for his exceptional mentorship both in the drafting of my thesis as well as my time spent at NASA's Johnson Space Center. I must also thank Professor Belinda Marchand and Dr. Sara Scarritt for providing their expertise and laying the groundwork for my research. I would like to acknowledge Professors Carolin Frueh and David Spencer whose questions and feedback have inspired me to seek out new knowledge.

Thank you to Purdue University and the School of Aeronautics and Astronautics for their roles in the completion of my degree. For providing funding and the opportunity to teach, I thank the Department of Mathematics. I also greatly appreciate support provided by the NASA JSC NNX13AK60A grant.

TABLE OF CONTENTS

Page

LIST OF TABLES

LIST OF FIGURES

Figure Page

ABSTRACT

York, Collin E. MSAA, Purdue University, December 2018. Application of a Two-Level Targeter for Low-Thrust Spacecraft Trajectories. Major Professor: Kathleen C. Howell.

Applications of electric propulsion to spaceflight in multi-body environments require a targeting algorithm to produce suitable trajectories on the ground and on board spacecraft. The two-level targeter with low thrust (TLT-LT) provides a framework to implement differential corrections in computationally-limited autonomous spacecraft applications as well as the larger design space of pre-mission planning. Extending existing two-level corrections algorithms, applications of the TLT-LT to spacecraft with a range of propulsive capabilities, from nearly-impulsive to low-thrust, are explored. The process of determining partial derivatives is generalized, allowing reduced logical complexity and increased flexibility in designing sequences of thrusting and ballistic segments. Various implementation strategies are explored to enforce constraints on time and other design variables as well as to improve convergence behavior through the use of dynamical systems theory and attentuation factors. The TLT-LT is applied to both nearly-impulsive and low-thrust spacecraft applications in the circular restricted three-body problem to demonstrate the flexibilty of the framework to correct trajectories across the spectrum of thrust magnitude. Finally, parameter continuation is employed to extend a family of trajectories from a solution with nearly-impulsive thrust events to the low-thrust regime, and the characteristics of this transition are investigated.

1. Introduction

1.1 Motivation

As NASA prepares for cislunar operations of manned spacecraft and eventual missions to the vicinity of Mars under the Exploration program, low thrust spacecraft feature as potential solutions to facilitate crewed and uncrewed missions. Current NASA applications under investigation involve the delivery of the Gateway space station to a Near Rectilinear Halo-Orbit and the transfer of Gateway to other lunar orbits via low thrust propulsion systems. The application, for example, of electric propulsion systems to human spaceflight problems in these new multi-body environments requires a differential corrections algorithm to generate and correct suitable trajectories both on the ground and on board spacecraft.

In the planning stage of a mission, a capable targeting algorithm is a key component to develop a reference solution with a baseline control history. Targeting applications in the design phase are characterized by large initial discontinuities for initial guesses and design variables that are not limited to operational control inputs. During flight, a targeter must have the ability to modify this reference solution on board a spacecraft in response to navigation, thrust, and other errors. In this scenario, a reduced set of design variables may be available for targeting, reflecting the smaller set of opertionally-feasible spacecraft control inputs. With limitations in flight hardware capability, a targeting algorithm with reduced computational load is also required. Additionally, the necessity for on-board convergence of a navigable trajectory is critical in the event of lost or limited communications with a human crew. The complexity of both ground and on-board applications is compounded by the nature of low thrust trajectories. Since traditional chemical rockets supply a relatively large acceleration over a short burn duration, trajectory designers traditionally model such thrust events as impulsive velocity changes. However, electric propulsion generates relatively low accelerations over significant durations in relation to the total time of flight, causing the spacecraft to deviate from its ballistic trajectory more gradually but less intuitively. A differential corrections algorithm with the capability to determine pre-planned reference trajectories, converge predictably with minimal computational on-board processing, and handle impulsive and low thrust segments of a mission is required to address these problems.

1.2 Previous Contributions

In his work *PhilosophæNaturalis Principae Mathematica*, published in 1687, Isaac Newton developed a mathematical model for the motion of $\mathcal{N}$-bodies under the influence of gravitational forces [1], sparking centuries of investigations into the nature of solutions to this dynamical system. Though closed-form analytical solutions Simplifying this model to capture the motion of a body with negligible mass moving under the influence of two dominant gravitational bodies in circular orbits, the circular restricted three-body problem, formulated by Leonhard Euler in 1722 [2], provides insight into the motion of spacecraft in the Earth-Moon system. Investigating this three-body model, Joseph-Louis Lagrange and Leonhard Euler determined the existence of triangluar and colinear equilibrium conditions, respectively. Allowing insight into the underlying dynamics, the lone integral of the motion, the Jacobi Constant, was derived by Carl Gustav Jacob Jacobi in 1836 [3]. In *Theory of Orbits*, published in 1967, Victor Szebehely offers a comprehensive discussion of the circular restricted three-body problem and the search for periodic solutions [3].

Differential corrections methods based on work developed by Newton [1] prove critical to the determination of solutions to nonlinear systems, such as the one described by the circular restricted three-body problem. A subset of differential corrections methods, labelled shooting schemes, are presented by Keller, Shipman, and Roberts as strategies to solve two point boundary value problems [4–6]. One such type of differential corrections algorithm with computational and convergence characteristics compatible with on-board targeting is the *two-level targeter* (TLT), a multiple shooting process for implusive thrust trajectories, developed by Pernicka and Howell and expanded upon by Marchand [7, 8]. The iterative first level within the TLT corrects the trajectory for position continuity by altering velocity at each discretized node or *patch point*, and the second level targets velocity continuity by updating patch point positions and times. Scarritt extends the TLT algorithm to include finite burns, propulsive events modeled as accelerations over finite time intervals to improve model fidelity, introducing parameters such as thrust angle and burn duration to the Level-I design variables [9].

1.3 Current Work

The objective of this research investigation is to develop an effective two-level differential corrections algorithm which can target trajectories that include nearly-impulsive as well as low-thrust thrust events. Additionally, procedural strategies for implementing the algorithm, such as weighting design variables and deconflicting constraints, are presented. A set of applications with varying propulsion capabilities and initial constraint violations is tested to demonstrate the capabilities of the algorithm.

This investigation is organized as follows:

- **Chapter 2:** Dynamical Models — The differential equations governing the motion of bodies in a gravitation field are introduced, and the dynamical system associated with the circular restricted three-body problem is derived. The concept of characteristic quantities of the system is employed to non-dimensionalize the equations of motion, and the integral of the motion and equilibrium points are determined. Finally, the circular restricted three-body problem is augmented to include accelerations due to a propulsive force.

- **Chapter 3:** Differential Corrections — This chapter details the process of deriving linear variational equations for a nonlinear system and introduces multiple differential corrections strategies. Single shooting algorithms are developed with fixed and variable time and expanded into multiple shooting methods with discretized nodes. A particular implementation of multiple shooting, two-level targeting that distributes the correction process between multiple stages is forumlated for spacecraft trajectories with instantaneous velocity changes.

- **Chapter 4:** Low-Thrust Two-Level Corrections — A framework for modeling frequently employed trajectory segments as thrust, coast, and split arcs is developed and shown to reduce to a common form. Expanding on the impulsive two-level corrections strategies, a two-level targeter with low thrust capability is derived to correct for position, velocity, and mass continuity.

- **Chapter 5:** Implementation Strategies — Algorithm design choices and strategies for a two-level corrections algorithm for spacecraft with low-thrust propulsion systems are explored. Processes for addressing design variable constraints, determining design vector update solutions based on dynamic sensitivity, and applying attentuation factors are outlined.

- **Chapter 6:** Mission Applications — To verify the effectivenss of the low-thrust two-level corrections algorithm in computing suitable trajectories, three applications of varying propulsive capability are explored. First, a traditional low-thrust transfer between periodic orbits about libration points is corrected. Additionally, a nearly-impulsive finite burn trajectory is targeted from an impulsive reference solution. Finally, the nearly-impulsive solution is incrementally altered through a continuation process on engine parameters to create trajectories that approach what is typically considered low thrust.

- **Chapter 7:** Summary — The final chapter includes a summary of the investigation. Recommendations for future work are presented based on the findings of this analysis.

2. Dynamical Models

Dynamical models of varying levels of fidelity offer different insights into trajectory design problems. Incorporating the gravitational influences of an arbitrarily large number of bodies delivers a comprehensive model for spacecraft motion. Though all the forces are included in such a description of the system, this formulation of the problem does not possess a closed-form analytical solution and yields little insight into the general flow. In regimes where one graviational body is dominant, such as low Earth orbit, the mathematical model that represents the two-body problem yields closed-form analytical solutions for spacecraft motion through the use of integrals of motion. As more bodies increasingly influence the system, the two body model loses accuracy, and models of higher fidelity are more successful in approximating suitable trajectories. As mission applications evolve into multi-body regimes, e.g., a regime with two significant gravitional fields, the circular restricted three-body problem better reflects the evolution of spacecraft paths and the underlying flow is evaluated via dynamical systems theory.

The development of electric propulsion systems over the last few decades introduces low thrust alternatives to chemical rockets and adds another influence on the motion. Traditionally, mathematical models incorporate chemical engines to deliver impulsive velocity changes; however, low thrust engines produce continuous accelerations. Thus, the dynamical model is augmented to include accelerations from the propulsion system.

2.1 The $\mathcal{N}$-Body Problem

Newtonian mechanics details the development of a dynamical model for a system comprised of $\mathcal{N}$ bodies, each approximated as spherically symmetric. An illustration of the special case with $\mathcal{N} = 3$ appears in Figure 2.1 with unit vectors $\hat{\boldsymbol{X}}$, $\hat{\boldsymbol{Y}}$, and $\hat{\boldsymbol{Z}}$ representing an inertial reference frame I. The movement of the body of interest

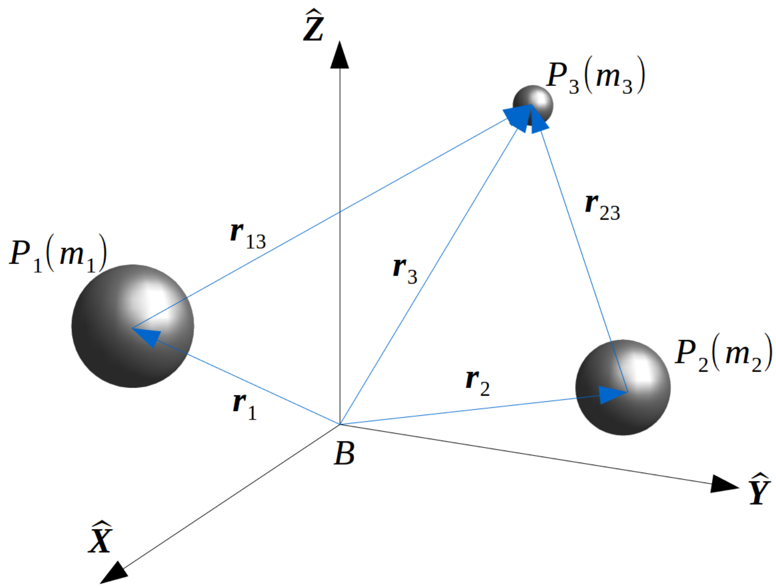

Figure 2.1. Generalized 3-Body Gravitational Model in the Inertial Frame

P_i with mass m_i relative to an inertially-fixed base point under the influence of only gravitational forces is represented via the vector differential equation

$$\tilde{m}_i \frac{{}^I \mathrm{d}^2 \tilde{\boldsymbol{r}}_i}{\mathrm{d}\tilde{t}^2} = -\tilde{G} \sum_{\substack{j=1 \\ j \neq i}}^{N} \frac{\tilde{m}_i \tilde{m}_j}{\tilde{r}_{ji}^3} \tilde{\boldsymbol{r}}_{ji} \tag{2.1}$$

where $\tilde{\boldsymbol{r}}_i$ is the position vector of P_i relative to an inertially-fixed base point, $\tilde{m}_j$ is the mass associated with each of the other primaries P_j, $\tilde{\boldsymbol{r}}_{ji}$ is the position vector from P_j to P_i, $\tilde{G}$ is the universal gravitational constant in the appropriate dimensional units, and B denotes the barycenter of the system. Note that in Equation (2.1), the left superscript I denotes derivatives, i.e., rates of change, as observed in the inertial reference frame, and unbolded quantities denote vector magnitudes. While this model for the $\mathcal{N}$-body problem incorporates an arbitrary number of bodies, the absence of a closed-form analytical solution and integrals of the motion limit its usefulness in understanding the fundamental dynamical properties of the system.

2.2 Circular Restricted Three-Body Problem

While the $\mathcal{N}$-body problem offers limited insight into the natural motion, a special case involving only three bodies lends information concerning the underlying flow through the search for integrals of the motion and equilibrium solutions. In systems with a small satellite and two major gravitational bodies, such as a spacecraft in star-planet or planet-moon systems, the circular restricted three body problem (CR3BP) supplies a framework for investigating spacecraft motion before transitioning to a higher-fidelity model.

The three-body problem consists of three bodies P_1, P_2, and P_3 with masses $\tilde{m}_1$, $\tilde{m}_2$, and $\tilde{m}_3$, respectively. A vector differential equation for the motion of P_3 relative to an inertially fixed point as viewed by an inertial observer is described through Equation (2.1) such that

$$\tilde{m}_3 \frac{{}^I\,\mathrm{d}^2\tilde{\boldsymbol{r}}_3}{\mathrm{d}\tilde{t}^2} = -\tilde{G}\frac{\tilde{m}_3\tilde{m}_1}{\tilde{r}_{13}^3}\tilde{\boldsymbol{r}}_{13} - \tilde{G}\frac{\tilde{m}_3\tilde{m}_2}{\tilde{r}_{23}^3}\tilde{\boldsymbol{r}}_{23} \tag{2.2}$$

for the case when $\mathcal{N} = 3$. This formulation consists of 18 state variables (3 bodies each with 3 position states and 3 velocity states) and only 10 known integrals of motion. Therefore, an analytical solution cannot be determined.

To further explore the problem, simplifying assumptions are enforced. The mass m_3 of body P_3 is assumed negligible in comparison to those of P_1 and P_2, and, therefore, P_3 does not influence the motions of P_1 and P_2. For example, a satellite in the vicinity of Earth and the Moon is easily reflected by this assumption. By convention, P_1 and P_2 are defined as the *primaries*, where P_1 is the larger body. This primary system satisfies the conditions for the two-body problem, and its motion is further assumed to be circular about its barycenter, B, with mean notion N.

2.2.1 Characteristic Quantities

The benefit of reformulating the CR3BP in terms of non-dimensional units is two-fold. First, the process scales the state variables such that they possess similar orders of magnitude, aiding in numerical analysis. This difference in state variable magnitude is illustrated in the Earth-Moon system, where the Moon orbits relative to the Earth with approximate distance and velocity of 384,000 km and 1 km/s, respectively. Second, thoughtful non-dimensionalization allows generalization of the problem through the mass parameter, μ. In this case, both benefits arise from selecting constant characteristic quantities related to the two-body dimensional mean motion of the primaries, N, for example,

$$N = \sqrt{\frac{\tilde{G}(\tilde{m}_1 + \tilde{m}_2)}{\tilde{r}_{12}^3}} \tag{2.3}$$

as quantities to non-dimensionalize the system. The characteristic mass, m^*, is defined as the sum of the primary masses, i.e.,

$$m^* = \tilde{m}_1 + \tilde{m}_2 \tag{2.4}$$

Illustrated in Figure 2.1, the characteristic length l^* is defined as the distance between the two primaries,

$$l^* = \tilde{r}_{12} \tag{2.5}$$

and represents the semi-major axis of the simplified primary system. The characteristic time, t^*, is written

$$t^* = \sqrt{\frac{{l^*}^3}{\tilde{G}m^*}} \tag{2.6}$$

such that the non-dimensional gravitational constant, G, is equal to unity and represents the reciprical of the primaries' mean motion. This identity for the gravitational constant is proven as

$$G = \tilde{G}\frac{m^*{t^*}^2}{{l^*}^3} = 1 \tag{2.7}$$

Following from the definition of the characteristic quantities, the non-dimensional mean motion of primary system, n, is also equal to one, i.e.,

$$n = Nt^* = \sqrt{\frac{\tilde{G}m^*}{{l^*}^3}\frac{{l^*}^3}{\tilde{G}m^*}} = 1 \tag{2.8}$$

The selection of characteristic quantities leads to a non-dimensional period of 2π for the primary system.

The vector differential equation defining motion in the system is rewritten in a non-dimensional form using the characteristic quantities of the primary system and a mass parameter. Defining this non-dimensional mass parameter, μ, as the ratio of the mass of P_2 to the primary system mass, written

$$\mu = \frac{\tilde{m}_2}{m^*} \tag{2.9}$$

yields additional quantities relating characteristic quantities and system distances

$$1 - \mu = \frac{\tilde{m}_1}{m^*} \tag{2.10}$$

$$\frac{\tilde{r}_1}{l^*} = \mu \tag{2.11}$$

$$\frac{\tilde{r}_2}{l^*} = 1 - \mu \tag{2.12}$$

Furthermore, non-dimensionalization of the position vectors,

$$\boldsymbol{\rho} = \frac{\tilde{\boldsymbol{r}}_3}{l^*} \tag{2.13}$$

$$\boldsymbol{d} = \frac{\tilde{\boldsymbol{r}}_{13}}{l^*} \tag{2.14}$$

$$\boldsymbol{r} = \frac{\tilde{\boldsymbol{r}}_{23}}{l^*} \tag{2.15}$$

along with the introduction of a non-dimensional time variable, t,

$$t = \frac{\tilde{t}}{t^*} \tag{2.16}$$

allows for substitution into Equation (2.2), yielding a non-dimensional second order vector differential equation,

$$\frac{{}^I\mathrm{d}^2\boldsymbol{\rho}}{\mathrm{d}t^2} = -\frac{1-\mu}{d^3}\boldsymbol{d} - \frac{\mu}{r^3}\boldsymbol{r} \tag{2.17}$$

This formulation accomplishes the goals of non-dimensionalization and generalization of the problem in terms of one parameter.

2.2.2 Rotating Frame

Within the CR3BP, the Keplerian motion of the primary system is circular and confined to the $\hat{\boldsymbol{X}}$-$\hat{\boldsymbol{Y}}$ plane. Projected on the orbital plane in Figure 2.2, reference frame R, rotating through angle θ with P_2 and with non-dimensional angular velocity $n\hat{\boldsymbol{Z}}$, is defined with an origin at the barycenter and a unit vector $\hat{\boldsymbol{x}}$ fixed on the line between P_1 and P_2. The unit vector $\hat{\boldsymbol{z}}$, congruent with $\hat{\boldsymbol{Z}}$, is out of the primary

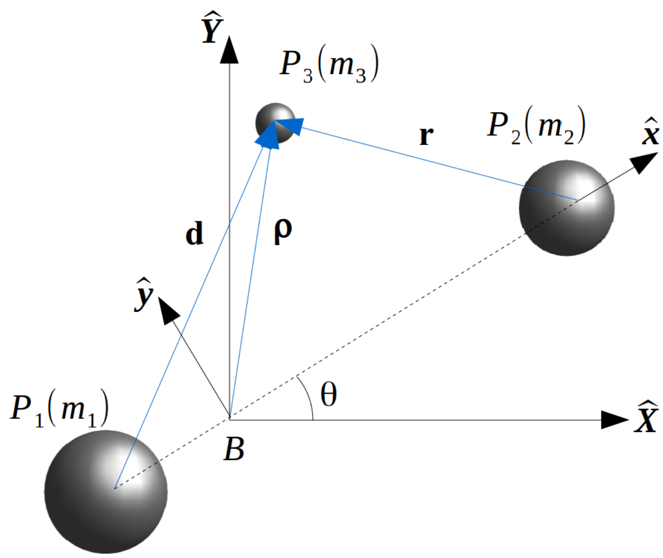

Figure 2.2. Three Bodies Relative to the Inertial and Rotating Frames

plane and parallel to the primary orbital angular momentum vector. Finally, unit vector $\hat{\boldsymbol{y}}$ completes the right-handed system and exists in the $\hat{\boldsymbol{X}}$-$\hat{\boldsymbol{Y}}$ plane. The angle θ is defined such that the two reference frames align at an initial time. The non-dimensional position vector $\boldsymbol{\rho}$ is decomposed into its components as expressed in the rotating frame. Further analysis warrants a transition to the rotating frame R. The position vector from the barycenter to P_3, $\boldsymbol{\rho}$, is defined in the rotating frame as

$$\boldsymbol{\rho} = x\hat{\boldsymbol{x}} + y\hat{\boldsymbol{y}} + z\hat{\boldsymbol{z}} \tag{2.18}$$

with $\boldsymbol{v}$ being the non-dimensional time derivative with respect to an observer in the rotating frame,

$$\boldsymbol{v} = \frac{{}^{R}\mathrm{d}\boldsymbol{\rho}}{\mathrm{d}t} = \dot{x}\hat{\boldsymbol{x}} + \dot{y}\hat{\boldsymbol{y}} + \dot{z}\hat{\boldsymbol{z}} \tag{2.19}$$

In this notation, a dot denotes the non-dimensional time derivative with respect to an observer in the rotating frame.

Due to the terms in the force model and their representation in terms of a rotating frame, a kinematic expansion is required to relate the derivatives with respect to a rotating observer to those with respect to an inertial observer. The Basic Kinematic Equation is employed to expand the left side of Equation (2.17), generating expressions,

$$\frac{{}^{I}\mathrm{d}\boldsymbol{\rho}}{\mathrm{d}t} = \frac{{}^{R}\mathrm{d}\boldsymbol{\rho}}{\mathrm{d}t} + {}^{I}\boldsymbol{\omega}^{R} \times \boldsymbol{\rho} \tag{2.20}$$

$$\frac{{}^{I}\mathrm{d}^2\boldsymbol{\rho}}{\mathrm{d}t^2} = \frac{{}^{R}\mathrm{d}^2\boldsymbol{\rho}}{\mathrm{d}t^2} + 2{}^{I}\boldsymbol{\omega}^{R} \times \frac{{}^{R}\mathrm{d}\boldsymbol{\rho}}{\mathrm{d}t} + {}^{I}\boldsymbol{\omega}^{R} \times {}^{I}\boldsymbol{\omega}^{R} \times \boldsymbol{\rho} \tag{2.21}$$

for the first and second non-dimensional time derivatives relative to an inertial observer. Employing the definition ${}^{I}\boldsymbol{\omega}^{R} = n\hat{\boldsymbol{z}}$, where n is constant, Equation (2.21) yields

$$\frac{{}^{I}\mathrm{d}^2\boldsymbol{\rho}}{\mathrm{d}t^2} = (\ddot{x} - 2n\dot{y} - n^2x)\hat{\boldsymbol{x}} + (\ddot{y} + 2n\dot{x} - n^2y)\hat{\boldsymbol{y}} + \ddot{z}\hat{\boldsymbol{z}} \tag{2.22}$$

for the inertial acceleration of $\boldsymbol{\rho}$ as expressed in the rotating coordinate system. Since the right sides of Equations (2.17) and(2.21) must be equal, and recalling that $n = 1$, the expressions are rearranged to generate a second-order vector derivative in terms of the scalar components of the state variables $\boldsymbol{\rho}$ and $\mathbf{v}$ as well as the parameter μ, i.e.,

$$\ddot{\boldsymbol{\rho}} = \begin{bmatrix} \ddot{x} \\ \ddot{y} \\ \ddot{z} \end{bmatrix} = \begin{bmatrix} 2\dot{y} + x - \frac{(1-\mu)(x+\mu)}{d^3} - \frac{\mu(x-1+\mu)}{r^3} \\ -2\dot{x} + y - \frac{(1-\mu)y}{d^3} - \frac{\mu y}{r^3} \\ -\frac{(1-\mu)z}{d^3} - \frac{\mu z}{r^3} \end{bmatrix} = \mathbf{f}(\boldsymbol{\rho}, \boldsymbol{v}) \tag{2.23}$$

where $\mathbf{f}(\boldsymbol{\rho}, \boldsymbol{v})$ offers a convenient notation for the nonlinear vector expression. Additionally, the function notation demonstrates that the system is not a function of time when converted to the rotating frame and, therefore, an autonomous system. Even in a first-order state space representation, the differential equations remain coupled and nonlinear; a closed-form analytical solution is not available.

2.2.3 Integrals of the Motion

In the CR3BP, one integral of the motion emerges from the formulation of the differential equations, i.e., the *Jacobi Constant*. This single constant of the motion assists in determining equilibrium solutions and bounded regions for motion of the infinitesimal third body. In pursuit of this integral of the motion, an alternative representation of the differential equations in terms of a "pseudo-potential" function, U^*, proves useful. This pseudo-potential function augments the gravitational potential energy with rotational energy that accommodates the rotation of the frame in the new formulation of the differential equations and is defined as

$$U^* = \frac{1-\mu}{d} + \frac{\mu}{r} + \frac{x^2+y^2}{2} \tag{2.24}$$

Thus, an equivalent representation of the Equation (2.23), expressed in scalar form, appears as

$$\ddot{x} - 2\dot{y} = \frac{\partial U^*}{\partial x} \tag{2.25}$$

$$\ddot{y} + 2\dot{x} = \frac{\partial U^*}{\partial y} \tag{2.26}$$

$$\ddot{z} = \frac{\partial U^*}{\partial z} \tag{2.27}$$

Operating on the differential equations in Equation (2.25)-(2.27) via a scalar dot product with the velocity relative to a rotating observer results in

$$\ddot{x}\dot{x} + \ddot{y}\dot{y} + \ddot{z}\dot{z} = \frac{\partial U^*}{\partial x}\dot{x} + \frac{\partial U^*}{\partial y}\dot{y} + \frac{\partial U^*}{\partial z}\dot{z} \tag{2.28}$$

where the terms containing $\dot{x}\dot{y}$ cancel. This scalar equation is straightfoward to integrate analytically.

Since the pseudo-potential is a function of only x, y, and z, the right side of Equation (2.28) represents the total derivative of U^* with respect to non-dimensional time. Taking the integral with respect to τ and some algebriac manipulation yields

$$C = 2U^* - v^2 \tag{2.29}$$

where C is the constant of integration, and v denotes the norm of the $\boldsymbol{v}$. The constant C is, in fact, the Jacobi Constant and provides the only known integral of motion for the CR3BP. The Jacobi Constant represents an energy-like quantity for the CR3BP in the rotating frame.

2.2.4 Equilibrium Solutions

Additional insight into the dynamical environment of the CR3BP is gained from the equilibrium solutions. An equilibrium solution satisfies the governing differential equations when all derivatives with respect to a rotating observer are zero. Enforcing this condition on Equations (2.25)-(2.27) provides a convenient representation, written as

$$\left.\frac{\partial U^*}{\partial x}\right|_{\boldsymbol{\rho}_{eq}} = -\frac{(1-\mu)(x_{eq}+\mu)}{d_{eq}^3} - \frac{\mu(x_{eq}-1+\mu)}{r_{eq}^3} + x_{eq} = 0 \tag{2.30}$$

$$\left.\frac{\partial U^*}{\partial y}\right|_{\boldsymbol{\rho}_{eq}} = -\frac{(1-\mu)y_{eq}}{d_{eq}^3} - \frac{\mu y_{eq}}{r_{eq}^3} + y_{eq} = 0 \tag{2.31}$$

$$\left.\frac{\partial U^*}{\partial z}\right|_{\boldsymbol{\rho}_{eq}} = -\frac{(1-\mu)z_{eq}}{d_{eq}^3} - \frac{\mu z_{eq}}{r_{eq}^3} = 0 \tag{2.32}$$

where the subscript eq refers to equilibrium states. The conditions in Equation (2.32) are only satsified when $z_{eq} = 0$; therefore, all equilibrium solutions exist in the orbital plane of the primaries.

Noting that $y_{eq} = 0$ satisfies Equation (2.31), the equilibrium solutions on the $\hat{\boldsymbol{x}}$-axis are explored. With this assumption, Equation (2.30) is revised and rewritten in the form

$$-\frac{(1-\mu)(x_{eq}+\mu)}{|x_{eq}+\mu|^3} - \frac{\mu(x_{eq}-1+\mu)}{|x_{eq}-1+\mu|^3} + x_{eq} = 0 \tag{2.33}$$

which includes three regions for possible solutions, $-\infty < x_{eq} < -\mu$, $-\mu < x_{eq} < 1-\mu$, and $1-\mu < x_{eq} < \infty$. Since Equation (2.33) lacks an analytical solution, iterative numerical methods prove successful in approximating solutions in these three regions, labelled the collinear libration points. These three points are denoted L_1, L_2, and L_3, in order of decreasing Jacobi Constant. Two additional equilibrium solutions also exist, located off of the $\hat{\boldsymbol{x}}$-axis when $d_{eq} = r_{eq} = 1$. By substituting into Equations (2.30) and (2.31), these libration points, i.e., L_4 and L_5, are determined at the vertex of an equilateral triangle formed with additional vertices at P_1 and P_2. The L_4 point has an off-axis component $y_{eq} > 0$, and the L_5 point is its reflection across the $\hat{\boldsymbol{x}}$-axis. Figure 2.3 illustrates all five libration points, also commonly labelled Lagrange points, in the Earth-Moon system. The determination of libration points for a given system serves as a starting point for exploring the associated periodic orbits in the rotating frame and the bounded regions of space.

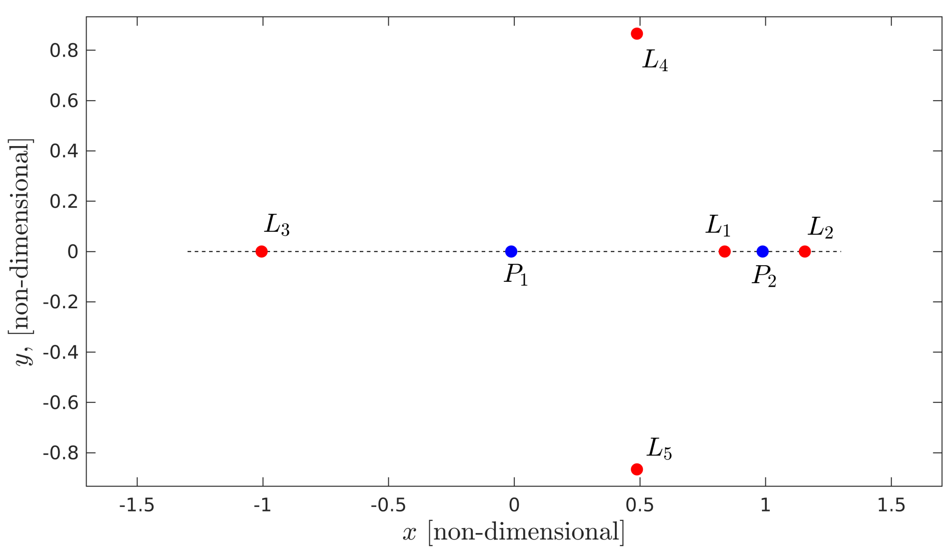

Figure 2.3. Libration Points in the Earth-Moon System to Scale

2.3 CR3BP Model with Low Thrust

With the recent interest in electric propulsion applications, dynamical models for low thrust spacecraft in multi-body environments aid in generating suitable trajectories. One such set of equations of motion represents a generalized low thrust spacecraft in a dynamical regime consistent with the CR3BP. Expanding on a generalized thrust force, assumptions and mathematical descriptions are applied to the vector and engine models to allow further investigation. Finally, the parameters that define the thrust characteristics are incorporated as control inputs, and the efficacy of using these controls in a CR3BP environment is investigated.

2.3.1 Low Thrust CR3BP Equations of Motion

The inclusion of low thrust propulsion systems warrants augmentation of the dynamical model to include an additional thrust force. In this investigation, the low thrust spacecraft is assumed to incorporate a dimensional variable thrust vector, $\bar{\boldsymbol{T}}$. Simplify the spacecraft mass notation such that, $\tilde{m}_3$, is denoted $\tilde{m}$. Then, a new dynamical model,

$$\frac{{}^{I}\,\mathrm{d}^2\tilde{\boldsymbol{r}}_3}{\mathrm{d}\tilde{t}^2} = -\tilde{G}\frac{\tilde{m}_1}{\tilde{r}_{13}^3}\tilde{\boldsymbol{r}}_{13} - \tilde{G}\frac{\tilde{m}_2}{\tilde{r}_{23}^3}\tilde{\boldsymbol{r}}_{23} + \frac{\tilde{\boldsymbol{T}}}{\tilde{m}} \tag{2.34}$$

includes the effect of gravitational and thrusting forces on acceleration of the spacecraft position relative to the primary system barycenter with respect to an inertial observer. Each term in Equation (2.34) has dimensions of [length] / [time]^2, so any non-dimensionalization of the [mass] dimension in $\tilde{\boldsymbol{T}}$ and $\tilde{m}$ cancels in the numerator and denominator of the thrust term, allowing arbitrary selection of such a quantity. To maintain well-conditioned states for numerical analysis, a new characteristic quantity, m_s^*, is introduced as

$$m_s^* = \tilde{m}(\tilde{t}_0) \tag{2.35}$$

and represents the spacecraft mass evaluated at the initial time, $\tilde{t}_0$. This quantity is employed to generate a non-dimensional thrust vector, i.e.,

$$\boldsymbol{T} = \tilde{\boldsymbol{T}} \frac{t^{*2}}{l^* m_s^*} \tag{2.36}$$

and the evolving non-dimensional spacecraft mass,

$$m = \frac{\tilde{m}}{m_s^*} \tag{2.37}$$

where $m = 1$ initially by definition.

To non-dimensionalize Equation (2.34), use m_s^* and the characteristic quantities from the standard CR3BP to produce a low thrust analog of Equation (2.17),

$$\frac{{}^I\,\mathrm{d}^2\boldsymbol{\rho}}{\mathrm{d}t^2} = -\frac{1-\mu}{d^3}\boldsymbol{d} - \frac{\mu}{r^3}\boldsymbol{r} + \frac{\boldsymbol{T}}{m} \tag{2.38}$$

The addition of a thrust term to the right side of the differential equation does not change the kinematic expansion on the left side, as noted in Equation (2.22). Substituting in the kinematic expansion yields

$$\ddot{\boldsymbol{\rho}} = \mathbf{f}(\boldsymbol{\rho}, \boldsymbol{v}) + \frac{\boldsymbol{T}}{m} \tag{2.39}$$

using the shorthand function notation of the CR3BP equations of motion, $\mathbf{f}(\boldsymbol{\rho}, \boldsymbol{v})$. When $\boldsymbol{T} = \mathbf{0}$, this dynamical model is identical to the standard CR3BP.

2.3.2 Thrust Vector and Engine Model

The thrust vector is modelled with variable magnitude in a spherical coordinate system that is based in the rotating frame R. To represent physical limits on engine output, thrust magnitude is bounded to the closed interval $[0, T_{max}]$, where T_{max} is the maximum achieveable thrust. The thrust parameter, γ, is introduced, to model this constraint, leading to a mathematical description of a bounded variable thrust magnitude,

$$T = T_{max} \sin^2(\gamma) \tag{2.40}$$

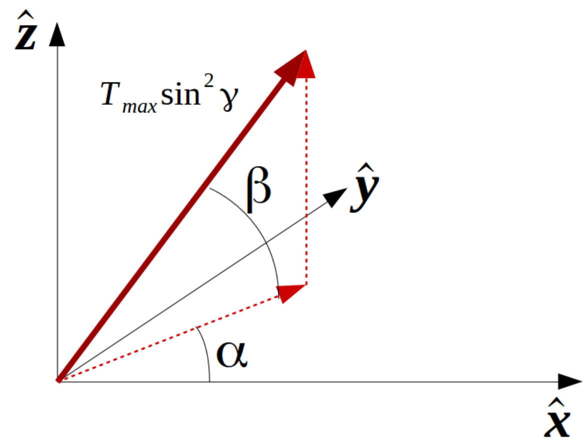

Figure 2.4. Vector Representation of the Thrust Vector Direction and Magnitude

Illustrated in Figure 2.4, an in-plane angle, α, describes the projection of $\boldsymbol{T}$ onto the $\hat{\boldsymbol{x}}$-$\hat{\boldsymbol{y}}$ plane with $\alpha = 0$ when aligned with the $\hat{\boldsymbol{x}}$ axis. The out-of-plane angle, β, is measured relative to the $\hat{\boldsymbol{x}}$-$\hat{\boldsymbol{y}}$ plane. Together with the expression for thrust magnitude in Equation (2.40), these variables supply a complete representation of the thrust vector,

$$\boldsymbol{T} = T_{max} \sin^2(\gamma) \begin{bmatrix} \cos(\alpha)\cos(\beta) \\ \sin(\alpha)\cos(\beta) \\ \sin(\beta) \end{bmatrix} \tag{2.41}$$

written in vector form.

Since a low thrust engine operates by expending mass, the spacecraft mass, m, is not assumed as constant and is represented as an additional state variable. For this investigation, the non-dimensional specific impulse, I_{sp}, of the engine is constant, and the mass rate of change with respect to non-dimensional time is expressed as

$$\dot{m} = \frac{T}{I_{sp} g_0} \tag{2.42}$$

where g_0 is the non-dimensional constant standard acceleration due to gravity. The dimensional standard acceleration due to gravity, $\tilde{g}_0$, is 9.80665 m/s^2. A propulsion system that satisfies this assumption is deemed a *constant specific impulse* (CSI) engine.

3. Differential Corrections Methods

For dynamical systems that lack closed-form analytical solutions, e.g., the CR3BP, numerical methods are required to generate trajectories that satisfy the governing differential equations. Additionally, constraints on the spacecraft motion, such as bounded fly-by altitude or the necessity to arrive at a specific location at a given time, may be required for nearly all mission scenarios. Though many techniques exist to produce satisfactory trajectories, differential corrections algorithms based on Newton's method are employed in this investigation to approximate solutions that satsify the constraints to within a given tolerance.

A constraint vector, $\mathbf{F}$, comprised of m scalar constraints, is defined as a function of the design vector, $\mathbf{X}$, possessing n design variables. Each constraint is formulated such that its fullfillment,

$$\mathbf{F}(\mathbf{X}) = \mathbf{0} \tag{3.1}$$

results in the zero vector. Originating with a design vector, $\mathbf{X}_i$, that does not satisfy the constraints, an iterative process is employed to update the design vector with the goal of converging the constraint vector to satisfy Equation (3.1) to within a given tolerance. Neglecting higher order terms, a Taylor series expansion of the constraint vector yields a first-order approximation,

$$\mathbf{F}_{i+1} \approx \mathbf{F}_i + \mathrm{D}\mathbf{F}(\mathbf{X}_{i+1} - \mathbf{X}_i) \tag{3.2}$$

where subscripts denote subsequent iterations i and $i+1$. The Jacobian of the constrants with respect to the design variables is denoted $\mathrm{D}\mathbf{F}$. The total change in the vector of design variables, $\mathrm{d}\mathbf{X}$, is defined as the difference between the design vector at iteration i and $i+1$, i.e.,

$$\mathrm{d}\mathbf{X} = \mathbf{X}_{i+1} - \mathbf{X}_i \tag{3.3}$$

By setting $\mathbf{F}_{i+1} = \mathbf{0}$, the linear approximation from Equation (3.2) is reformulated to solve for $\mathrm{d}\mathbf{X}$, yielding expressions for two conditions. To simplify the notation, $\mathbf{F}_i$ is replaced by simply $\mathbf{F}$, because $\mathbf{F}_{i+1}$ is eliminated from the expression. Thus, Equation (3.2) simplifies to

$$\mathbf{0} = \mathbf{F} + \mathrm{D}\mathbf{F}\,\mathrm{d}\mathbf{X} \tag{3.4}$$

First, if $n = m$ and $\mathrm{D}\mathbf{F}$ is non-singluar, then $\mathrm{d}\mathbf{X}$ is evaluated as

$$\mathrm{d}\mathbf{X} = -\mathrm{D}\mathbf{F}^{-1}\mathbf{F} \tag{3.5}$$

This solution is only valid when the number of design variables and constrants are equal, leading to a *uniquely determined* system.

However if $n > m$, the system is said to be *underdetermined*, and an infinite number of solutions exist. To reduce the step size in $\mathbf{X}$, an optimization problem is formulated to obtain the minimum-norm solution for the update to the design vector, i.e.,

$$\begin{aligned} &\text{Minimize} && \mathrm{d}\mathbf{X}^T\,\mathrm{d}\mathbf{X} \\ &\text{Subject to} && \mathbf{F} = -\mathrm{D}\mathbf{F}\,\mathrm{d}\mathbf{X} \end{aligned} \tag{3.6}$$

A vector of Lagrange multipliers, $\boldsymbol{\lambda}$, is employed to generate a cost functional, J, mathematically described by

$$J = \mathrm{d}\mathbf{X}^T\,\mathrm{d}\mathbf{X} + \boldsymbol{\lambda}^T(\mathrm{D}\mathbf{F}\,\mathrm{d}\mathbf{X} + \mathbf{F}) \tag{3.7}$$

To obtain the solution with the minimum cost, the partial derivatives of J with respect to $\mathrm{d}\mathbf{X}$ and $\boldsymbol{\lambda}$ are both equal to zero, expressed

$$\left(\frac{\partial J}{\partial(\mathrm{d}\mathbf{X})}\right)^T = 2\,\mathrm{d}\mathbf{X} - \mathrm{D}\mathbf{F}^T\boldsymbol{\lambda} = \mathbf{0} \tag{3.8}$$

$$\left(\frac{\partial J}{\partial\boldsymbol{\lambda}}\right)^T = \mathrm{D}\mathbf{F}\,\mathrm{d}\mathbf{X} + \mathbf{F} = \mathbf{0} \tag{3.9}$$

respectively. By algebriac manipulation, Equation (3.8) is solved for $\mathrm{d}\mathbf{X}$, yielding

$$\mathrm{d}\mathbf{X} = \frac{\mathrm{D}\mathbf{F}^T\boldsymbol{\lambda}}{2} \tag{3.10}$$

and substituted into Equation (3.9) to develop an expression for $\boldsymbol{\lambda}$, i.e.,

$$\boldsymbol{\lambda} = -2(\mathrm{D}\mathbf{F}\mathrm{D}\mathbf{F}^T)^{-1}\mathbf{F} \tag{3.11}$$

Manipulation of Equation (3.10) produces an expression for $\boldsymbol{\lambda}$ which when substituted into Equation (3.11) yields the minimum-norm solution for d$\mathbf{X}$, i.e.,

$$\mathrm{d}\mathbf{X} = -\mathrm{D}\mathbf{F}^T(\mathrm{D}\mathbf{F}\mathrm{D}\mathbf{F}^T)^{-1}\mathbf{F} \tag{3.12}$$

This solution is valid for all cases with more design variables than constraints.

In the final case, when $n < m$, the system is *overdetermined*, and no solution for d$\mathbf{X}$ exists which satisfies all constraints. In this case, an optimization problem is posed in search of the solution which minimizes the norm of the difference between $\mathbf{F}$ and $-\mathrm{D}\mathbf{F}\,\mathrm{d}\mathbf{X}$, i.e.,

$$\begin{aligned} &\text{Minimize} \qquad && (\mathbf{F} + \mathrm{D}\mathbf{F}\,\mathrm{d}\mathbf{X})^T(\mathbf{F} + \mathrm{D}\mathbf{F}\,\mathrm{d}\mathbf{X}) \\ &\text{Subject to} && \mathbf{F} = -\mathrm{D}\mathbf{F}\,\mathrm{d}\mathbf{X} \end{aligned} \tag{3.13}$$

A cost functional J_O is defined with Lagrange multipliers, expressed

$$J_O = (\mathbf{F} + \mathrm{D}\mathbf{F}\,\mathrm{d}\mathbf{X})^T(\mathbf{F} + \mathrm{D}\mathbf{F}\,\mathrm{d}\mathbf{X}) + \boldsymbol{\lambda}^T(\mathbf{F} + \mathrm{D}\mathbf{F}\,\mathrm{d}\mathbf{X}) \tag{3.14}$$

Again, the optimal solution is determined by setting the partial derivatives of J_O with respect to d$\mathbf{X}$ and $\boldsymbol{\lambda}$ to zero, represented mathematically as

$$\left(\frac{\partial J_O}{\partial(\mathrm{d}\mathbf{X})}\right)^T = 2\mathrm{D}\mathbf{F}^T\mathrm{D}\mathbf{F}\,\mathrm{d}\mathbf{X} + 2\mathrm{D}\mathbf{F}^T\mathbf{F} + \mathrm{D}\mathbf{F}^T\boldsymbol{\lambda} = \mathbf{0} \tag{3.15}$$

$$\left(\frac{\partial J_O}{\partial \boldsymbol{\lambda}}\right)^T = \mathrm{D}\mathbf{F}\,\mathrm{d}\mathbf{X} + \mathbf{F} = \mathbf{0} \tag{3.16}$$

By solving Equation (3.16) for $\mathbf{F}$ and substituting into Equation (3.15), the Lagrange multipliers are proven equal to the zero vector. By setting $\boldsymbol{\lambda} = \mathbf{0}$, the least squares solution is determined from Equation (3.15), i.e.,

$$\mathrm{d}\mathbf{X} = -(\mathrm{D}\mathbf{F}^T\mathrm{D}\mathbf{F})^{-1}\mathrm{D}\mathbf{F}^T\mathbf{F} \tag{3.17}$$

resulting in an update to the design vector that produces the minimum residual error in $\mathbf{F}$. In practice, the design variables should be selected avoid to the case of an overdetermined system, if possible, because a solution within a given error tolerance is not guaranteed.

3.1 State Transition Matrix

In the analysis of nonlinear systems of differential equations, linearization with respect to a reference solution lends preliminary insight into nonlinear behavior. The linear system represents the actual system only in the vicinity of the reference solution, when perturbations are relatively small. Linear variational equations are typically adequate for differential corrections methods.

A general system of differential equations is explored to derive equations that govern the evolution of variations over time. A state vector, $\mathbf{x}$, evolves in time, governed by the vector differential equation

$$\dot{\mathbf{x}} = \mathbf{f}(\mathbf{x}, t) \tag{3.18}$$

where $\mathbf{f}$ need not be linear. The state vector is a function of the initial state, $\mathbf{x}_0$, at the initial time, t_0, and of the terminal time, t. A solution to the differential equations,

$$\mathbf{x}(\mathbf{x}_0, t) = \mathbf{x}'(\mathbf{x}'_0, t) + \delta\mathbf{x}(t) \tag{3.19}$$

is defined as the sum of the contemporaneous variation, $\delta\mathbf{x}$, and the reference solution, $\mathbf{x}'$. The schematic in Figure 3.1 reflects the relationship between the reference solution, contemporaneous variation, and nearby solution. Both sides of Equation

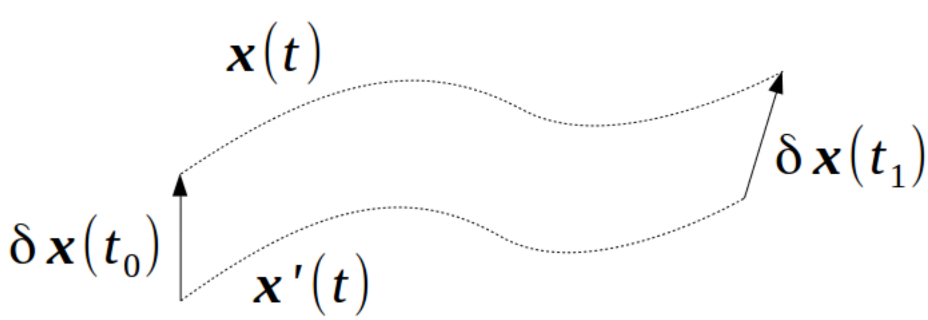

Figure 3.1. State Vector Solution Defined as a Perturbation from a Reference Solution.

(3.19) are differentiated with respect to time, yielding

$$\dot{\mathbf{x}}(\mathbf{x}_0, t) = \dot{\mathbf{x}}'(\mathbf{x}'_0, t) + \delta\dot{\mathbf{x}}(t) \tag{3.20}$$

An alternative representation of the first derivative of the state vector is derived by substituting Equation (3.19) into Equation (3.18),

$$\dot{\mathbf{x}}'(\mathbf{x}'_0, t) + \delta\dot{\mathbf{x}}(t) = \mathbf{f}(\mathbf{x}'(\mathbf{x}'_0, t) + \delta\mathbf{x}(t)) \tag{3.21}$$

A Taylor expansion on the right side, about the reference solution, results in

$$\dot{\mathbf{x}}'(\mathbf{x}'_0, t) + \delta\dot{\mathbf{x}}(t) = \mathbf{f}(\mathbf{x}'(\mathbf{x}'_0, t)) + \left.\frac{\partial \mathbf{f}}{\partial \mathbf{x}}\right|_{\mathbf{x}'(\mathbf{x}'_0, t)} \delta\mathbf{x}(t) + \mathcal{O}^2 \tag{3.22}$$

where $\mathcal{O}^2$ represents terms of order 2 and greater. Neglecting these higher order terms and using Equation (3.18) to equate $\dot{\mathbf{x}}'(\mathbf{x}'_0, t) = \mathbf{f}(\mathbf{x}'(\mathbf{x}'_0, t))$, leads to a linear approximation for the time derivaive of the variation, i.e.,

$$\delta\dot{\mathbf{x}}(t) \approx \left.\frac{\partial \mathbf{f}}{\partial \mathbf{x}}\right|_{\mathbf{x}'(\mathbf{x}'_0, t)} \delta\mathbf{x}(t) = \mathcal{A}(t)\delta\mathbf{x}(t) \tag{3.23}$$

where $\mathcal{A}(t)$ is the Jacobian for $\mathbf{f}$ with respect to the state vector evaluated on a given reference solution. The solution to Equation (3.23) appears in the form

$$\begin{aligned} \delta\mathbf{x}(t) &= \frac{\partial \mathbf{x}(t)}{\partial \mathbf{x}(t_0)}\delta\mathbf{x}(t_0) \\ &= \Phi(t, t_0)\delta\mathbf{x}(t_0) \end{aligned} \tag{3.24}$$

providing a linear mapping between the initial and final state variations. The transformation $\frac{\partial \mathbf{x}(t)}{\partial \mathbf{x}(t_0)}$ is evaluated along the reference solution and denoted the *state transition matrix* (STM), $\Phi(t, t_0)$. As this linear map is a function of time, its time derivative is evaluated as follows

$$\frac{\mathrm{d}}{\mathrm{d}t}\frac{\partial \mathbf{x}}{\partial \mathbf{x_0}} = \frac{\partial}{\partial \mathbf{x}_0}\frac{\mathrm{d}\mathbf{x}}{\mathrm{d}t} = \frac{\partial \mathbf{f}}{\partial \mathbf{x}_0} = \frac{\partial \mathbf{f}}{\partial \mathbf{x}}\frac{\partial \mathbf{x}}{\partial \mathbf{x}_0} = \mathcal{A}(t)\frac{\partial \mathbf{x}}{\partial \mathbf{x}_0} \tag{3.25}$$

with the simplified representation,

$$\dot{\Phi} = \mathcal{A}(t)\Phi \tag{3.26}$$

Various integration techniques are used to compute the STM as it evolves through time.

Several properties of the state transition matrix are useful. A linear mapping from time t_0 to t_0 results in an initial value of the STM equal to the identity matrix, i.e.,

$$\Phi(t_0, t_0) = \frac{\partial \mathbf{x}(t_0)}{\partial \mathbf{x}(t_0)} = I \tag{3.27}$$

Additionally, propagation of variations from time t_0 to time t_2 are also represented as the multiplication of two STMs, by introducing an intermediate time t_1, i.e.,

$$\Phi(t_2, t_0) = \frac{\partial \mathbf{x}(t_2)}{\partial \mathbf{x}(t_0)} = \frac{\partial \mathbf{x}(t_2)}{\partial \mathbf{x}(t_1)} \frac{\partial \mathbf{x}(t_1)}{\partial \mathbf{x}(t_0)} = \Phi(t_2, t_1)\Phi(t_1, t_0) \tag{3.28}$$

Finally, the inverse of an STM from t_0 to t_1 reflects an STM propagated backward in time from t_1 to t_0,

$$\Phi(t_0, t_1) = \frac{\partial \mathbf{x}(t_0)}{\partial \mathbf{x}(t_1)} = \left(\frac{\partial \mathbf{x}(t_1)}{\partial \mathbf{x}(t_0)}\right)^{-1} = \Phi(t_1, t_0)^{-1} \tag{3.29}$$

These properties allow reformulation of various differential corrections applications.

3.2 Single Shooting

A *single shooting* algorithm is commonly formulated to solve a two point boundary value problem (TPBVP), where the design variables include initial and final conditions along a single trajectory arc and the constraints frequently involve initial and/or final conditions. The constraint vector is defined uniquely for each application. After propagation, the error in the constraint vector is used in the linear representation of the dynamical system to update the design vector iteratively until the norm of the contraint vector is satisfied to within an established tolerance. In the following examples, a spacecraft on a ballistic path with its motion governed by the dynamical differential equations in the CR3BP in Equation (2.23) must match its position, $\boldsymbol{\rho}_1$, at the final time, t_1, with the desired position, $\boldsymbol{\rho}_{1,d}$. The constraint is then described mathematically as

$$\mathbf{F} = \boldsymbol{\rho}_1 - \boldsymbol{\rho}_{1,d} = \mathbf{0} \tag{3.30}$$

To accomplish this goal, the initial spacecraft velocity with respect to an observer rotating with the primary system, $\boldsymbol{v}_0$, is varied while the initial position, $\boldsymbol{\rho}_0$ is held constant. In dimensional units, the initial state,

$$\tilde{\boldsymbol{\rho}}_0 = \begin{bmatrix}192200 & 192200 & 0\end{bmatrix}^T \text{ km; } \tilde{\boldsymbol{v}}_0 = \begin{bmatrix}-0.5123 & 0.1025 & 0\end{bmatrix}^T \text{ km/s} \tag{3.31}$$

propagates from $\tilde{t}_0 = 0$ to $\tilde{t}_1 = 4.3425$ days with a desired final state,

$$\tilde{\boldsymbol{\rho}}_{1,d} = \begin{bmatrix}-153760 & 0 & 0\end{bmatrix}^T \text{ km} \tag{3.32}$$

With this sample scenario, single shooting methods involving fixed and variable propagation times are explored.

3.2.1 Contemporaneous Variations

An example of a single shooting corrections strategy with fixed propagation time is developed for the scenario in Equations (3.31) and (3.32). First, an implicit constraint is enforced by fixing the times, t_0 and t_1, as constants; therefore, the total variation in the state variable is equal its contemporaneous variation. The total variation for an arbitrary state vector, $\mathrm{d}\mathbf{x}$, at a fixed time is equal to the contemporaneous state variation, $\delta\mathbf{x}$, i.e.,

$$\mathrm{d}\mathbf{x} = \delta\mathbf{x} \tag{3.33}$$

as illustrated in Figure 3.2, where time and the scalar state variable are defined on the horizontal and vertical axes, respectively. The design vector in this mission scenario, written

$$\mathbf{X} = \boldsymbol{v}_0 \tag{3.34}$$

is comprised solely of the initial velocity. From the constraint vector in Equation (3.30) and this design vector in Equation (3.34), the Jacobian is expressed as

$$\mathrm{D}\mathbf{F} = \frac{\partial(\boldsymbol{\rho}_1 - \boldsymbol{\rho}_{1,d})}{\partial\mathbf{X}} = \frac{\partial\boldsymbol{\rho}_1}{\partial\mathbf{X}} - \frac{\partial\boldsymbol{\rho}_{1,d}}{\partial\mathbf{X}} = \frac{\partial\boldsymbol{\rho}_1}{\partial\mathbf{X}} \tag{3.35}$$

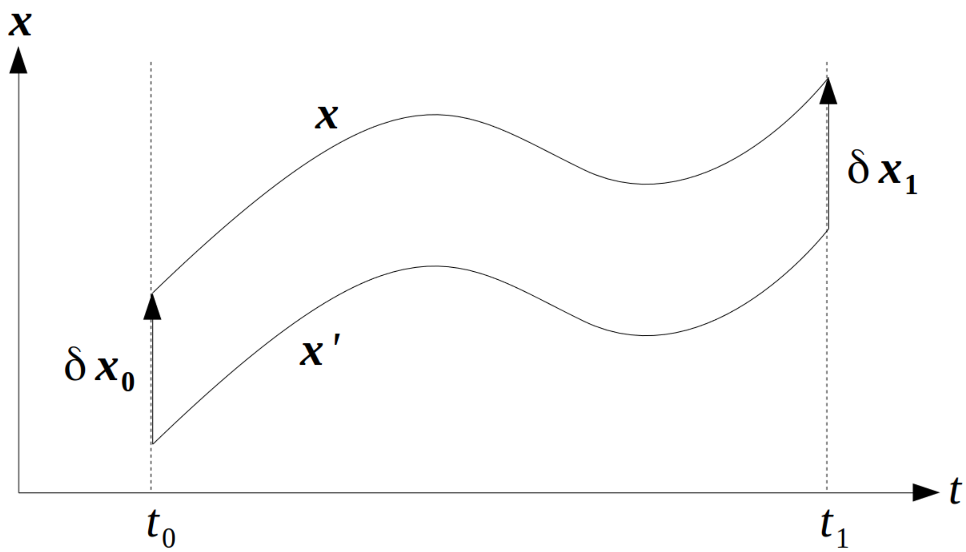

Figure 3.2. Contemporaneous State Variations

where the term associated with the desired final position, $\frac{\partial \boldsymbol{\rho}_{1,d}}{\partial \mathbf{X}}$, is the zero vector by the definition of a constant. The total variation over the full design vector, d$\mathbf{X}$, is formulated as

$$\mathrm{d}\mathbf{X} = \mathrm{d}\boldsymbol{v}_0 = \delta \boldsymbol{v}_0 \tag{3.36}$$

where the total variation is equal to the contemporaneous variation as well as the total variation in the initial velocity, due to the fixed-time assumption.

The STM provides a mapping of the initial variations onto the final variations based on the linear system dynamics relative to the initial guess reference trajectory, consistent with Equation (3.24). The mathematical representation for this linear map,

$$\begin{bmatrix} \delta \boldsymbol{\rho}_1 \\ \delta \boldsymbol{v}_1 \end{bmatrix} = \Phi(t_1, t_0) \begin{bmatrix} \delta \boldsymbol{\rho}_0 \\ \delta \boldsymbol{v}_0 \end{bmatrix} = \begin{bmatrix} A_{01} & B_{01} \\ C_{01} & D_{01} \end{bmatrix} \begin{bmatrix} \delta \boldsymbol{\rho}_0 \\ \delta \boldsymbol{v}_0 \end{bmatrix} \tag{3.37}$$

illustrates that the STM may be subdivided as a block matrix, where the matrix components A_{01}, B_{01}, C_{01}, and D_{01} are the partial derivative matrices $\frac{\partial \boldsymbol{\rho}_1}{\partial \boldsymbol{\rho}_0}$, $\frac{\partial \boldsymbol{\rho}_1}{\partial \boldsymbol{v}_0}$, $\frac{\partial \boldsymbol{v}_1}{\partial \boldsymbol{\rho}_0}$, and $\frac{\partial \boldsymbol{v}_1}{\partial \boldsymbol{v}_0}$, respectively. The relationship between the final position and the initial velocity is extracted, leading to

$$\delta \boldsymbol{\rho}_1 = B_{01} \delta \boldsymbol{v}_0 \tag{3.38}$$

where the fixed initial position, i.e., $\delta \boldsymbol{\rho}_0 = \mathbf{0}$, simplifies the expression. Since B_{01} is a non-singluar square matrix, the required variation in initial velocity to match the desired final position in the approximate linear system is evaluated as

$$\mathrm{d}\mathbf{X} = \mathrm{d}\boldsymbol{v}_0 = -B_{01}^{-1}\,\mathrm{d}\boldsymbol{\rho}_0 = -\mathrm{D}\mathbf{F}^{-1}\mathbf{F} \tag{3.39}$$

and matches the general form in Equation (3.5). Since time is constant, the contemporaneous variations are replaced with the total variations.

For the given initial conditions and constraints, the iterations resulting from the single shooting algorithm in Equation (3.39) are illustrated in Figure 3.3. After 6

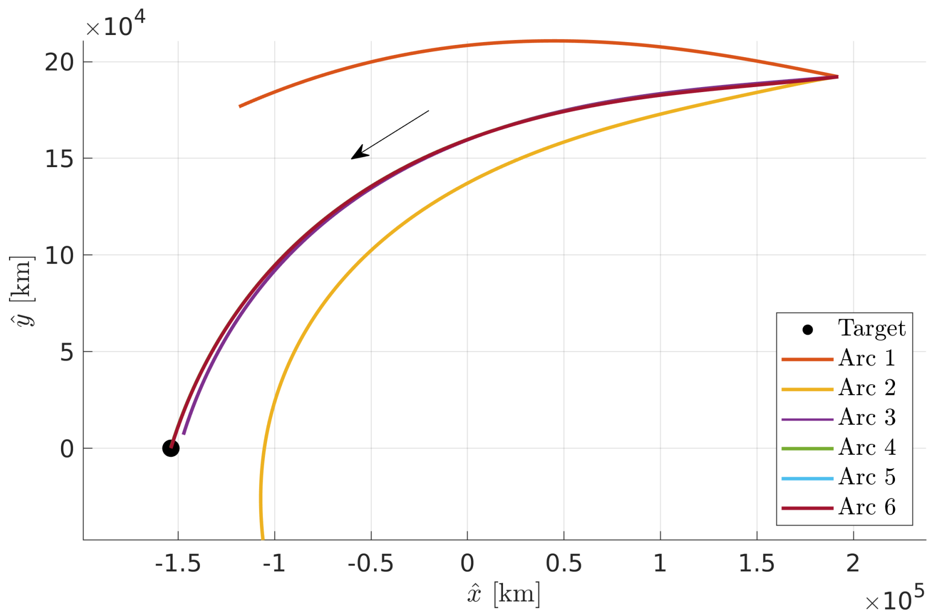

Figure 3.3. Fixed-Time Single Shooting Algorithm Example

iterations, the error in the final position reduces from 1.8022 km to 1.5050 mm, which falls within the selected 3.844 m convergence tolerance. Convergence on a targeted final position requires an adjustment to the initial guess for the initial velocity of approximately 174 m/s. Plotted in Figure 3.4, the error in the scalar constraint reduces quadratically with each iteration.

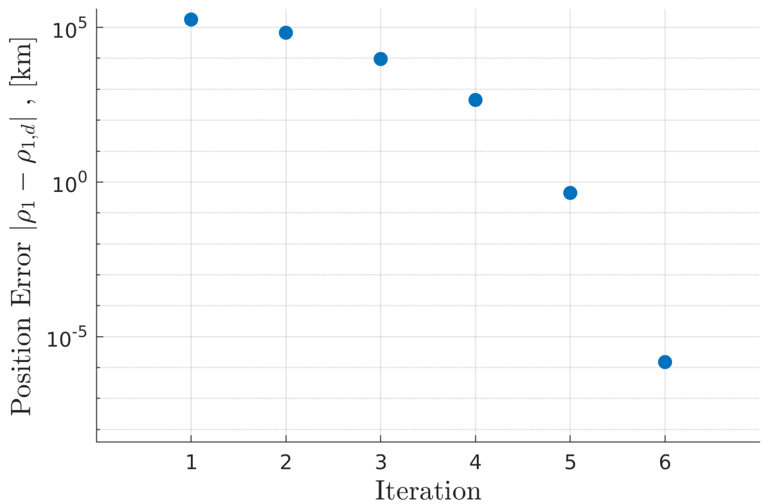

Figure 3.4. Quadratic Trend in Constraint Error

3.2.2 Non-contemporaneous Variations

Rather than assuming a constant time of flight (TOF), the same targeting scenario is explored with a variable final time. For a general state vector, $\mathbf{x}$, the total variation, $\mathrm{d}\mathbf{x}$, is the sum of the contemporaneous variation, $\delta\mathbf{x}$, and the component due to the change in time, $\mathrm{d}t$, expressed as

$$\mathrm{d}\mathbf{x} = \delta\mathbf{x} + \frac{\mathrm{d}\mathbf{x}}{\mathrm{d}t}\,\mathrm{d}t = \delta\mathbf{x} + \dot{\mathbf{x}}\,\mathrm{d}t \tag{3.40}$$

and illustrated in Figure 3.5. The objective is no longer to match $\boldsymbol{\rho}_1$ and $\boldsymbol{\rho}_{1,d}$ at a fixed final time but to match the positions at some variable final time. The new design vector is reformulated as

$$\mathbf{X} = \begin{bmatrix} \boldsymbol{v}_0 \\ t_1 \end{bmatrix} \tag{3.41}$$

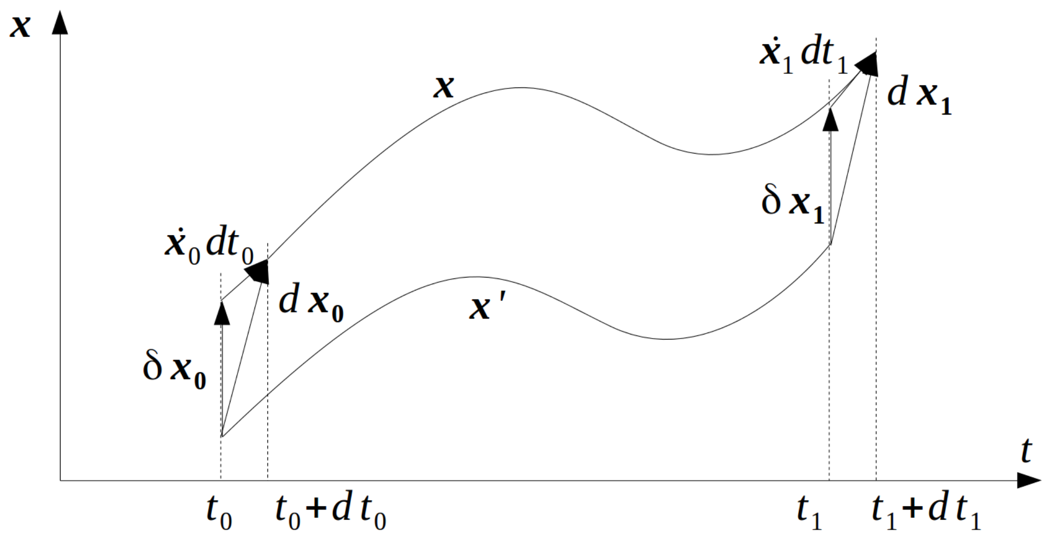

Figure 3.5. Non-Contemporaneous State Variations

Given the constraint vector, $\mathbf{F}$, in Equation (3.30), the Jacobian is expressed

$$\begin{aligned} \mathrm{D}\mathbf{F} &= \frac{\partial \boldsymbol{\rho}_1}{\partial \mathbf{X}} \\ &= \begin{bmatrix} \frac{\partial \boldsymbol{\rho}_1}{\partial \boldsymbol{v}_0} & \frac{\partial \boldsymbol{\rho}_1}{\partial t_1} \end{bmatrix} \end{aligned} \tag{3.42}$$

where partials associated with the constant $\boldsymbol{\rho}_{1,d}$ are equal to zero. The new design variable variation vector is written as

$$\mathrm{d}\mathbf{X} = \begin{bmatrix} \mathrm{d}\boldsymbol{v}_0 \\ \mathrm{d}t_1 \end{bmatrix} \tag{3.43}$$

since initial velocity and final time may vary.

As in the fixed-time case, the STM relates contemporaneous variations in the initial state to those in the final state. With initial time fixed, the contemporaneous varations at t_0 are equal to the total variations at that instant, i.e.,

$$\begin{aligned} \delta\boldsymbol{\rho}_0 &= \mathrm{d}\boldsymbol{\rho}_0 \\ \delta\boldsymbol{v}_0 &= \mathrm{d}\boldsymbol{v}_0 \end{aligned} \tag{3.44}$$

However, the contemporaneous variations at t_1 may be rewritten in terms of the total variations, i.e.,

$$\begin{aligned} \delta\boldsymbol{\rho}_1 &= \mathrm{d}\boldsymbol{\rho}_1 - \boldsymbol{v}_1\,\mathrm{d}t_1 \\ \delta\boldsymbol{v}_1 &= \mathrm{d}\boldsymbol{v}_1 - \boldsymbol{a}_1\,\mathrm{d}t_1 \end{aligned} \tag{3.45}$$

by using Equation (3.40). Employing the definitions in Equations (3.44) and (3.45), the STM yields a mathematical relationship between the initial and final total variations,

$$\begin{bmatrix} \mathrm{d}\boldsymbol{\rho}_1 - \boldsymbol{v}_1\,\mathrm{d}t_1 \\ \mathrm{d}\boldsymbol{v}_1 - \boldsymbol{a}_1\,\mathrm{d}t_1 \end{bmatrix} = \begin{bmatrix} A_{01} & B_{01} \\ C_{01} & D_{01} \end{bmatrix} \begin{bmatrix} \mathrm{d}\boldsymbol{\rho}_0 \\ \mathrm{d}\boldsymbol{v}_0 \end{bmatrix} \tag{3.46}$$

where $\boldsymbol{a}_1$ is the acceleration of the spacecraft at t_1 expressed in terms of the rotating frame as viewed by an observer in the rotating frame. Since initial position is fixed, i.e., $\mathrm{d}\boldsymbol{\rho}_0 = \mathbf{0}$, an expression for the constraint in terms of the design variable variations,

$$\mathrm{d}\boldsymbol{\rho}_1 = B_{01}\,\mathrm{d}\boldsymbol{v}_0 + \boldsymbol{v}_1\,\mathrm{d}t_1 \tag{3.47}$$

is extracted. In matrix form, the expression for the constraint is

$$\mathbf{F} = \boldsymbol{\rho}_1 - \boldsymbol{\rho}_{1,d} = \begin{bmatrix} B_{01} & \boldsymbol{v}_1 \end{bmatrix} \begin{bmatrix} \mathrm{d}\boldsymbol{v}_0 \\ \mathrm{d}t_1 \end{bmatrix} = \mathrm{D}\mathbf{F}\,\mathrm{d}\mathbf{X} \tag{3.48}$$

It is now in the form for application in the differential corrections algorithm. With a constraint vector of length $m = 3$ and design vector of $n = 4$ length, the linear system is underdetermined, and, therefore, the minimimum norm solution,

$$\begin{bmatrix} \mathrm{d}\boldsymbol{v}_0 \\ \mathrm{d}t_1 \end{bmatrix} = -\begin{bmatrix} B_{01} & \boldsymbol{v}_1 \end{bmatrix}^T \left(\begin{bmatrix} B_{01} & \boldsymbol{v}_1 \end{bmatrix} \begin{bmatrix} B_{01} & \boldsymbol{v}_1 \end{bmatrix}^T \right)^{-1} \mathrm{d}\boldsymbol{\rho}_1 \tag{3.49}$$

is employed to construct an appropriate variation in the design vector.

For the given initial conditions and constraints in the sample targeting problem, the iterations of the single shooting algorithm, as described in Equation (3.49), are illustrated in Figure 3.6. After 6 iterations, the error in the final position reduces from 1.8022 km to 7.3859 cm, a result that falls within the selected 3.844 m convergence tolerance, with the TOF extended by 1.0366 hours. To achieve convergence, an

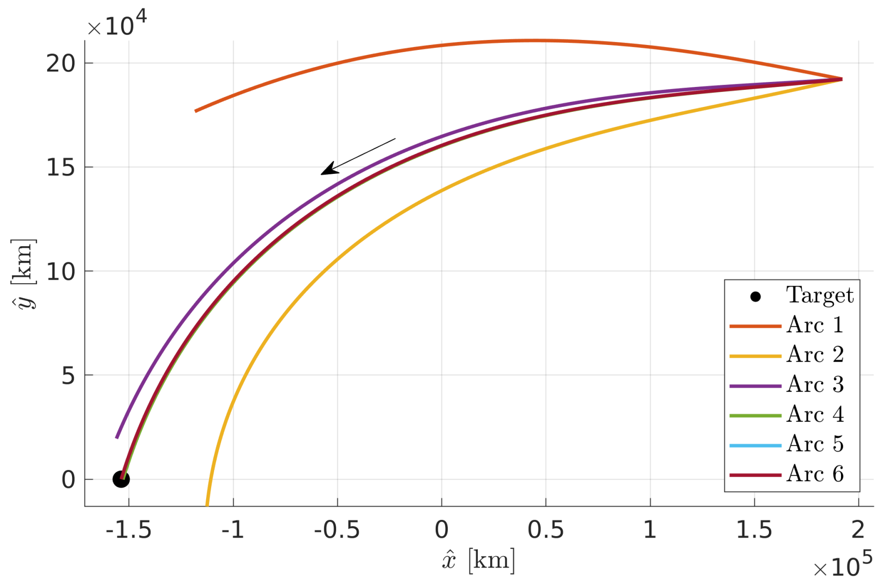

Figure 3.6. Variable-Time Single Shooting Algorithm Example

adjustment to the initial guess for the initial velocity of approximately 171 m/s is required. By allowing the TOF to vary, a smaller update to initial velocity is required than in the fixed-time case. As apparent in Figure 3.7, the order of magnitude of the error in the norm of the constraint vector reduces roughly quadratically with each subsequent iteration.

3.3 Multiple Shooting

In complex dynamical regimes or when long propagation times result in compounding the numerical error, the subdivision of a trajectory into multiple arcs aids in the differential corrections process and retaining numerical accuracy. A series of k nodes, denoted *patch points*, and $k-1$ propagation times define the overall trajectory, as demonstrated in Figure 3.8. A propagation time, τ_i, is defined as

$$\tau_i = t_{i+1} - t_i \tag{3.50}$$

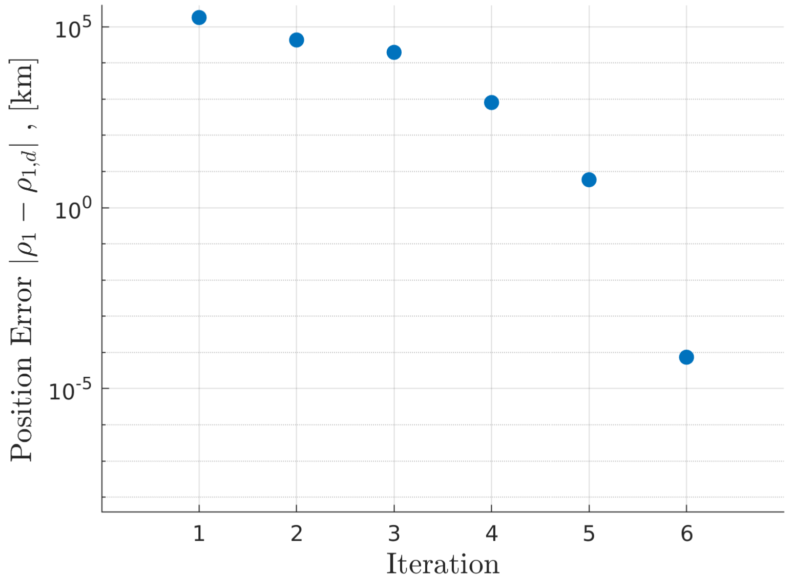

Figure 3.7. Quadratic Trend in Variable-Time Constraint Error

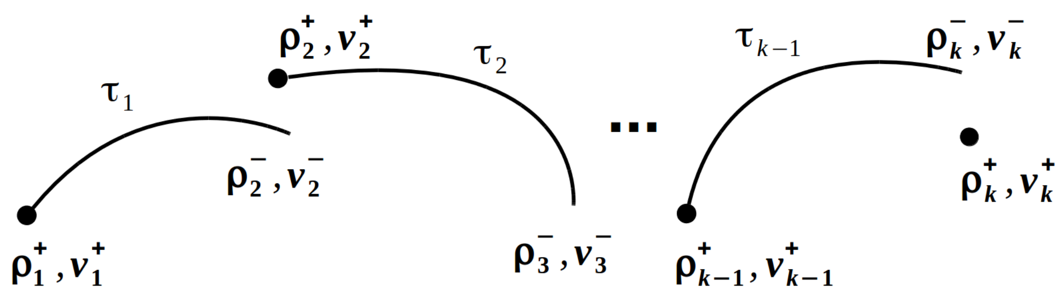

Figure 3.8. Schematic of Patch Points and Propagation Times

for each arc. A superscript plus (+) denotes the state propagating forward in time away from the patch point, and the superscript minus (−) signifies the terminal state of the arc approaching the patch point.

A differential corrections algorithm that solves TPBVPs for multiple patch points in parallel is labelled a *multiple shooting* algorithm. In such an algorithm, the design variable vector is represented

$$\mathbf{X} = \begin{bmatrix} \boldsymbol{\rho}_1^+ & \boldsymbol{v}_1^+ & \dots & \boldsymbol{\rho}_k^+ & \boldsymbol{v}_k^+ & \tau_1 & \dots & \tau_{k-1} \end{bmatrix}^T \tag{3.51}$$

with a constraint vector,

$$\mathbf{F} = \begin{bmatrix} \boldsymbol{\rho}_2^- - \boldsymbol{\rho}_2^+ \\ \boldsymbol{v}_2^- - \boldsymbol{v}_2^+ \\ \vdots \\ \boldsymbol{\rho}_k^- - \boldsymbol{\rho}_k^+ \\ \boldsymbol{v}_k^- - \boldsymbol{v}_k^+ \end{bmatrix} \tag{3.52}$$

defined to enforce state continuity at the patch points. The Jacobian matrix is constructed assuming that the incoming states depend only on the preceding patch point states and the corresponding propagation time, e.g. $\boldsymbol{\rho}_i^-(\boldsymbol{\rho}_{i-1}^+, \boldsymbol{v}_{i-1}^+, \tau_{i-1})$, and the outgoing states depend only on themselves.

For illustrative purposes, representative initial guess and converged trajectories are plotted in Figures 3.9 and 3.10, respectively. The initial guess possesses noticeable discontinuities between the blue propagated arcs and the black patch points. The multiple shooting algorithm iteratively updates the outgoing patch point states and propagation times in the design vector, $\mathbf{X}$, until the discontinuities are reduced substantially, falling within the convergence tolerance. This converged solution satsifies the both the governing equations and the constraint vector.

3.4 Two-Level Targeting

For on-board spacecraft operations where computational capacity may be limited, multiple shooting differential corrections algorithms that simultaneously target full state continuity at a large number of patch points may not be a feasible solution. For the case in Equation (3.52), inversion of a $6(k-1)$ square matrix is required to generate an update to the design vector. By decomposing the differential corrections

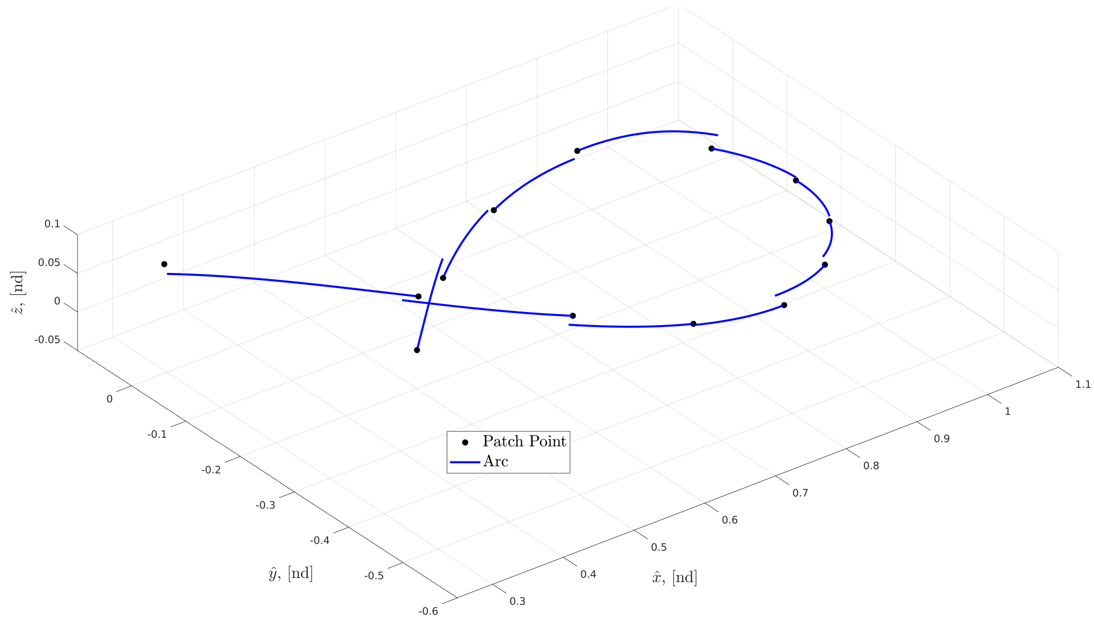

Figure 3.9. Initial Discontinuities between Propagated Incoming States and Outgoing Patch Point States

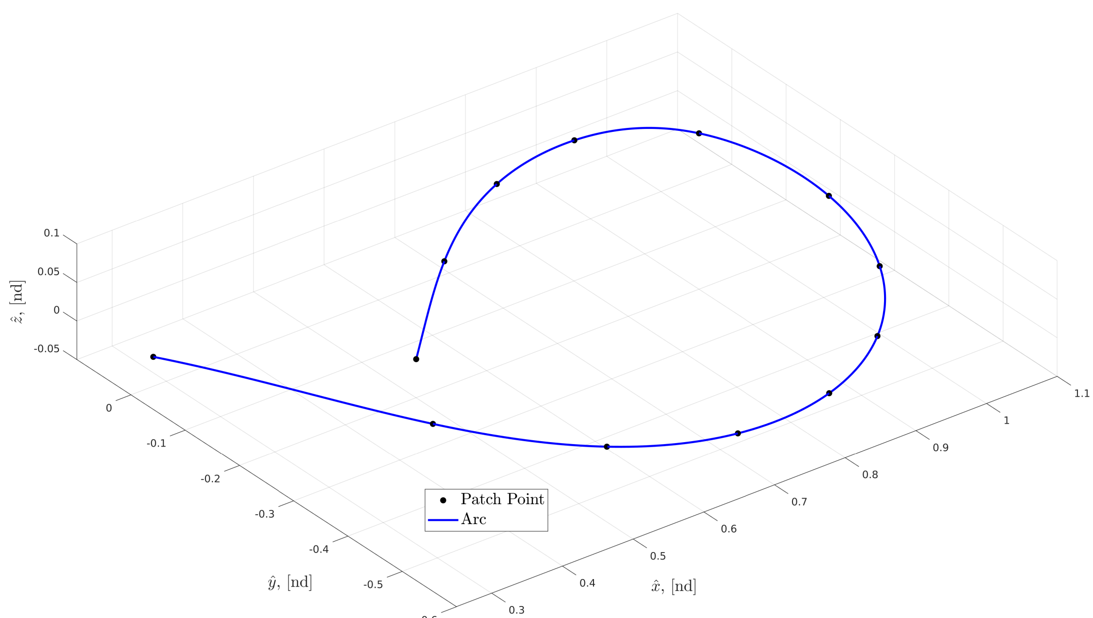

Figure 3.10. Convergence of the Multiple Shooting Algorithm

process into different parts, the size of the Jacobian and, therefore, the computational load in calculating its matrix inverse is decreased. Additionally, monotonic convergence behavior is more frequently observed in multi-stage corrections processes than in standard multiple shooting algorithms. In on-board applications where communication with ground stations may be limited or lost, the predictability in convergence gained from a staged targeting algorithm is valuable. One such corrections strategy with two levels is called a *Two-Level Targeter* (TLT). As originally formulated, the TLT is decomposed into Level-I which corrects for position continuity and Level-II which targets velocity continuity [7,8]. To model manuevers at patch points by chemical propulsion systems that occur over time intervals significantly smaller than the arc propagation times, the thrusting acceleration over a small duration may be represented as an instantaneous velocity change, labelled a Delta-V or impuslive maneuver. A two-level corrections algorithm that uses this assumption is named an impuslive TLT.

3.4.1 Impulsive Level-I

In Level-I of an impulsive TLT algorithm, position continuity within the convergence tolerance is achieved for each arc in series. An initially discontinuous set of arcs appears in Figure 3.11. Starting with the first patch point, the spacecraft trajectory is propagated from the initial patch point, $\mathcal{P}_o$, at time t_o to the next patch point, $\mathcal{P}_p$, at time t_p. The design vector,

$$\mathbf{X} = \boldsymbol{v}_o^+ \tag{3.53}$$

consists of the outgoing velocity vector at $\mathcal{P}_o$. This quantity is varied within a single shooting algorithm to achieve position continuity at $\mathcal{P}_p$, mathematically described by the constraint vector,

$$\mathbf{F} = \boldsymbol{\rho}_p^- - \boldsymbol{\rho}_p^+ = \mathbf{0} \tag{3.54}$$

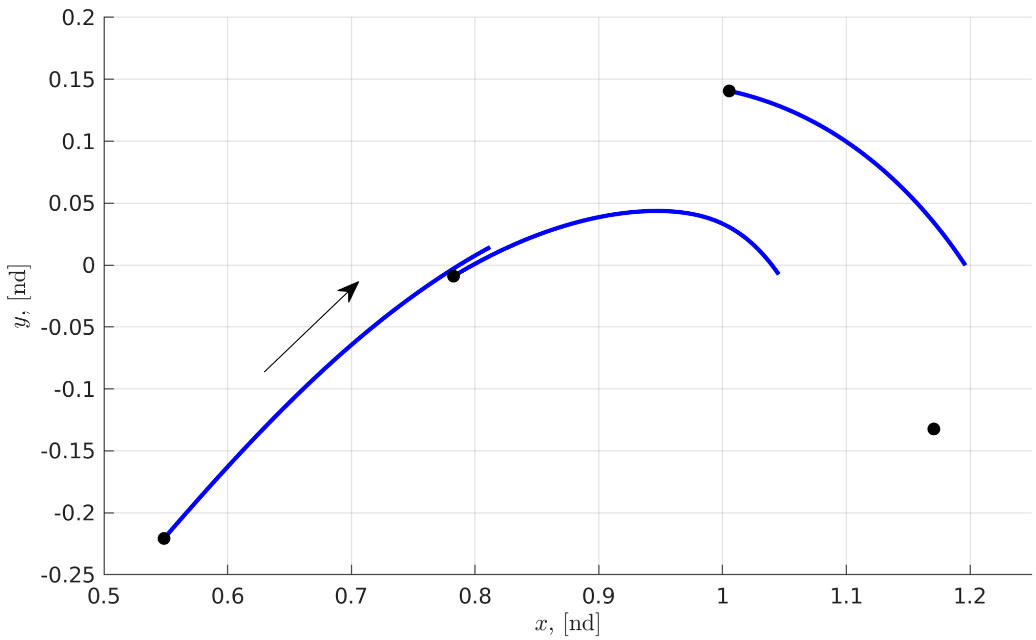

Figure 3.11. Initial Conditions for TLT Example

In practical terms, Level-I represents an impulsive manuever to target a new upstream position. The remaining component necessary to formulate an iterative Newton algorithm is the Jacobian,

$$\mathrm{D}\mathbf{F} = \frac{\partial \boldsymbol{\rho}_p^-}{\partial \boldsymbol{v}_o^+} \tag{3.55}$$

that models the outgoing position at $\mathcal{P}_p$ as a constant.

The STM is used to solve an iterative single shooting algorithm. The initial position, $\boldsymbol{\rho}_o^+$, and patch point times are constant, resulting in $\delta\boldsymbol{\rho}_o^+ = \mathbf{0}$ and $\mathrm{d}t_o = \mathrm{d}t_p = 0$. By employing the STM and simplifying, the variations at $\mathcal{P}_o$ and $\mathcal{P}_p$ are related by

$$\begin{bmatrix} \mathrm{d}\boldsymbol{\rho}_p^- \\ \mathrm{d}\boldsymbol{v}_p^- \end{bmatrix} = \Phi(t_p, t_o) \begin{bmatrix} \mathrm{d}\boldsymbol{\rho}_0^+ \\ \mathrm{d}\boldsymbol{v}_0^+ \end{bmatrix} = \begin{bmatrix} A_{op} & B_{op} \\ C_{op} & D_{op} \end{bmatrix} \begin{bmatrix} \mathrm{d}\boldsymbol{\rho}_0^+ \\ \mathrm{d}\boldsymbol{v}_0^+ \end{bmatrix} \tag{3.56}$$

This relationship leads to determination of the Jacobian,

$$\frac{\partial \boldsymbol{\rho}_p^-}{\partial \boldsymbol{v}_o^+} = B_{op} \tag{3.57}$$

which is substituded into Equation (3.5) to yield

$$d\boldsymbol{v}_o^+ = -B_{op}^{-1}\, d\boldsymbol{\rho}_p^- \tag{3.58}$$

Each iteration in the single shooting algorithm is denoted a *local iteration*. Once the **F** constraint is within the specified convergence tolerance, the algorithm is repeated for the next patch point in the series. The previous $\mathcal{P}_p$ becomes the new $\mathcal{P}_o$, and the next patch point is renamed $\mathcal{P}_p$. Once all the patch points have reached convergence through these sequential single shooting processes, Level-I is finished for a single *global iteration*.

3.4.2 Impulsive Level-II

Following completion of Level-I for a global iteration, the algorithm executes one multiple shooting correction in Level-II. The goal of Level-II is reduce velocity discontinuities by shifting patch point positions and times. For a trajectory comprised of k patch points, velocity continuity at the interior patch points is enforced by creating a constraint vector, i.e.,

$$\mathbf{F} = \begin{bmatrix} \boldsymbol{v}_2^- - \boldsymbol{v}_2^+ \\ \vdots \\ \boldsymbol{v}_{k-1}^- - \boldsymbol{v}_{k-1}^+ \end{bmatrix} \tag{3.59}$$

As apparent in Figure 3.12, all patch points may be considered continuous in position, expressed

$$\boldsymbol{\rho}_i = \boldsymbol{\rho}_i^+ = \boldsymbol{\rho}_i^- \tag{3.60}$$

and, therefore, no superscript is necessary for the position vectors. Thus, the design variable vector is formulated

$$\mathbf{X} = \begin{bmatrix} \boldsymbol{\rho}_1 \\ t_1 \\ \vdots \\ \boldsymbol{\rho}_k \\ t_k \end{bmatrix} \tag{3.61}$$

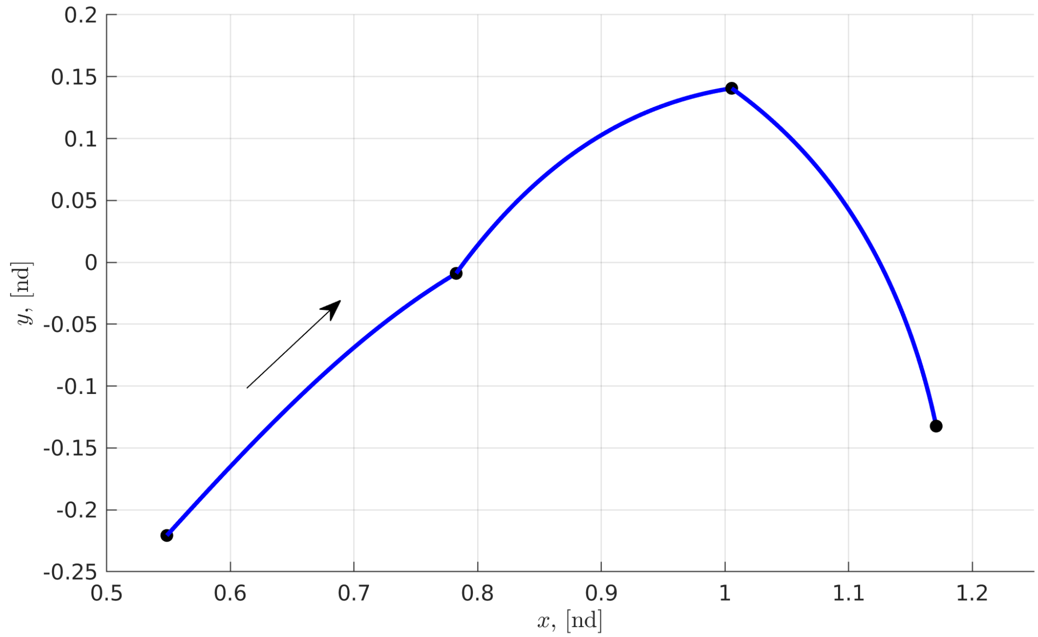

Figure 3.12. Position Continuity Following TLT Level-I Convergencence

and consists of the positions and times for all k patch points.

To construct the Level-II corrections algorithm, the Jacobian, D$\mathbf{F}$, is constructed in pieces. An interior patch point from $\mathbf{F}$ is deemed the present patch point, $\mathcal{P}_p$, with corresponding preceeding and subsequent patch points, denoted $\mathcal{P}_o$ and $\mathcal{P}_f$, respectively. States at $\mathcal{P}_p$ are assumed to depend only on states and times at $\mathcal{P}_o$, $\mathcal{P}_p$, and $\mathcal{P}_f$. The constraint and design vectors are rewritten as

$$\mathbf{F} = \begin{bmatrix} \vdots \\ \boldsymbol{v}_p^- - \boldsymbol{v}_p^+ \\ \vdots \end{bmatrix} \tag{3.62}$$

$$\mathbf{X} = \begin{bmatrix} \vdots \\ \boldsymbol{\rho}_o \\ t_o \\ \boldsymbol{\rho}_p \\ t_p \\ \boldsymbol{\rho}_f \\ t_f \\ \vdots \end{bmatrix} \tag{3.63}$$

respectively, to reflect this notation. The Jacobian,

$$\mathrm{D}\mathbf{F} = \begin{bmatrix} \vdots \\ \frac{\partial(\boldsymbol{v}_p^- - \boldsymbol{v}_p^+)}{\partial \mathbf{X}} \\ \vdots \end{bmatrix} \tag{3.64}$$

is built row by row. Further simplifying assumptions lead to derivation of the partial derivatives. The incoming velocity at $\mathcal{P}_p$, $\boldsymbol{v}_p^-$, is only a function of $\mathcal{P}_o$ and $\mathcal{P}_p$, and the outgoing velocity at $\mathcal{P}_p$, $\boldsymbol{v}_p^+$, is only a function of $\mathcal{P}_p$ and $\mathcal{P}_f$. From these assumptions, the Jacobian row of interest is reformulated as

$$\mathrm{D}\mathbf{F} = \begin{bmatrix} \vdots & & & & & & & \vdots \\ \mathbf{0} & \frac{\partial \boldsymbol{v}_p^-}{\partial \boldsymbol{\rho}_o} & \frac{\partial \boldsymbol{v}_p^-}{\partial t_o} & (\frac{\partial \boldsymbol{v}_p^-}{\partial \boldsymbol{\rho}_p} - \frac{\partial \boldsymbol{v}_p^+}{\partial \boldsymbol{\rho}_p}) & (\frac{\partial \boldsymbol{v}_p^-}{\partial t_p} - \frac{\partial \boldsymbol{v}_p^+}{\partial t_p}) & -\frac{\partial \boldsymbol{v}_p^+}{\partial \boldsymbol{\rho}_f} & -\frac{\partial \boldsymbol{v}_p^+}{\partial t_f} & \mathbf{0} \\ \vdots & & & & & & & \vdots \end{bmatrix} \tag{3.65}$$

in terms of the individual vector derivatives.

First, the partial derivatives of $\boldsymbol{v}_p^-$ with respect to the design variables are determined. The STM maps contemporaneous variations at $\mathcal{P}_p^-$ backwards in time to $\mathcal{P}_o^+$. Since patch point times are variable, substitution for total variations based on Equation (3.40) yields

$$\begin{bmatrix} \mathrm{d}\boldsymbol{\rho}_o^+ - \boldsymbol{v}_o^+ \,\mathrm{d}t_o \\ \mathrm{d}\boldsymbol{v}_o^+ - \boldsymbol{a}_o^+ \,\mathrm{d}t_o \end{bmatrix} = \begin{bmatrix} A_{po} & B_{po} \\ C_{po} & D_{po} \end{bmatrix} \begin{bmatrix} \mathrm{d}\boldsymbol{\rho}_p^- - \boldsymbol{v}_p^- \,\mathrm{d}t_p \\ \mathrm{d}\boldsymbol{v}_p^- - \boldsymbol{a}_p^- \,\mathrm{d}t_p \end{bmatrix} \tag{3.66}$$

where the backward-time STM is generated through inversion, i.e.,

$$\begin{bmatrix} A_{po} & B_{po} \\ C_{po} & D_{po} \end{bmatrix} = \begin{bmatrix} A_{op} & B_{op} \\ C_{op} & D_{op} \end{bmatrix}^{-1} \tag{3.67}$$

based on the property of STMs proven in Equation (3.29). From the position continuity assumption in Equation (3.60), the superscripts on the position vectors may be disregarded ($\mathrm{d}\boldsymbol{\rho}_i = \mathrm{d}\boldsymbol{\rho}_i^+ = \mathrm{d}\boldsymbol{\rho}_i^-$). Selecting the components of Equation (3.66) relating the first row on the left side, a relationship is determined between variations in only the constraint and design variables,

$$\mathrm{d}\boldsymbol{\rho}_o - \boldsymbol{v}_o^+ \,\mathrm{d}t_o = A_{po}(\mathrm{d}\boldsymbol{\rho}_p - \boldsymbol{v}_p^- \,\mathrm{d}t_p) + B_{po}(\mathrm{d}\boldsymbol{v}_p^- - \boldsymbol{a}_p^- \,\mathrm{d}t_p) \tag{3.68}$$

Rearranging this equation yields partial derivatives,

$$\begin{aligned} \frac{\partial \boldsymbol{v}_p^-}{\partial \boldsymbol{\rho}_o} &= B_{po}^{-1} \\ \frac{\partial \boldsymbol{v}_p^-}{\partial t_o} &= -\, B_{po}^{-1}\boldsymbol{v}_o^+ \\ \frac{\partial \boldsymbol{v}_p^-}{\partial \boldsymbol{\rho}_p} &= -\, B_{po}^{-1}A_{po} \\ \frac{\partial \boldsymbol{v}_p^-}{\partial t_p} &= B_{po}^{-1}A_{po}\boldsymbol{v}_p^- + \boldsymbol{a}_p^- \end{aligned} \tag{3.69}$$

that aid in construction of the Jacobian in Equation (3.65).

Since the constraint vector is formulated in terms of both incoming and outgoing velocity at the patch point, the mapping of changes in the design vector to changes in $\boldsymbol{v}_p^+$ is required. For the partial derivatives of $\boldsymbol{v}_p^+$ with respect to the design variables, another variational relationship,

$$\begin{bmatrix} \mathrm{d}\boldsymbol{\rho}_f^- - \boldsymbol{v}_f^- \,\mathrm{d}t_f \\ \mathrm{d}\boldsymbol{v}_f^- - \boldsymbol{a}_f^- \,\mathrm{d}t_f \end{bmatrix} = \begin{bmatrix} A_{pf} & B_{pf} \\ C_{pf} & D_{pf} \end{bmatrix} \begin{bmatrix} \mathrm{d}\boldsymbol{\rho}_p^+ - \boldsymbol{v}_p^+ \,\mathrm{d}t_p \\ \mathrm{d}\boldsymbol{v}_p^+ - \boldsymbol{a}_p^+ \,\mathrm{d}t_p \end{bmatrix} \tag{3.70}$$

employs the STM to map variations at $\mathcal{P}_p^+$ forward in time to $\mathcal{P}_f^-$. Selecting the portion related to the top row of the left side yields

$$\mathrm{d}\boldsymbol{\rho}_f - \boldsymbol{v}_f^- \,\mathrm{d}t_f = A_{pf}(\mathrm{d}\boldsymbol{\rho}_p - \boldsymbol{v}_p^+ \,\mathrm{d}t_p) + B_{pf}(\mathrm{d}\boldsymbol{v}_p^+ - \boldsymbol{a}_p^+ \,\mathrm{d}t_p) \tag{3.71}$$

where position is again assumed continuous at the patch points. From this equation, expressions of the partial derivatives of $\boldsymbol{v}_p^+$ with respect to the design variables is determined, i.e.,

$$\begin{aligned}
\frac{\partial \boldsymbol{v}_p^+}{\partial \boldsymbol{\rho}_f} =& B_{pf}^{-1} \\
\frac{\partial \boldsymbol{v}_p^+}{\partial t_f} =& -B_{pf}^{-1}\boldsymbol{v}_f^- \\
\frac{\partial \boldsymbol{v}_p^+}{\partial \boldsymbol{\rho}_p} =& -B_{pf}^{-1}A_{pf} \\
\frac{\partial \boldsymbol{v}_p^+}{\partial t_f} =& B_{pf}^{-1}A_{pf}\boldsymbol{v}_p^+ + \boldsymbol{a}_p^+
\end{aligned} \tag{3.72}$$

These partial derivatives allow construction of the D**F** matrix row for the designated patch point $\mathcal{P}_p$. To complete the D**F** matrix, the process is repeated with $\mathcal{P}_f$ becoming the new $\mathcal{P}_p$ and shifting all other subscripts accordingly. Once the Level-II Jacobian is fully allocated, the minimum-norm solution is computed to update the design vector. The updates to position and time variables lead to discontinuities entering the next global iteration of Level-I, illustrated in Figure 3.13. The entire TLT algorithm is

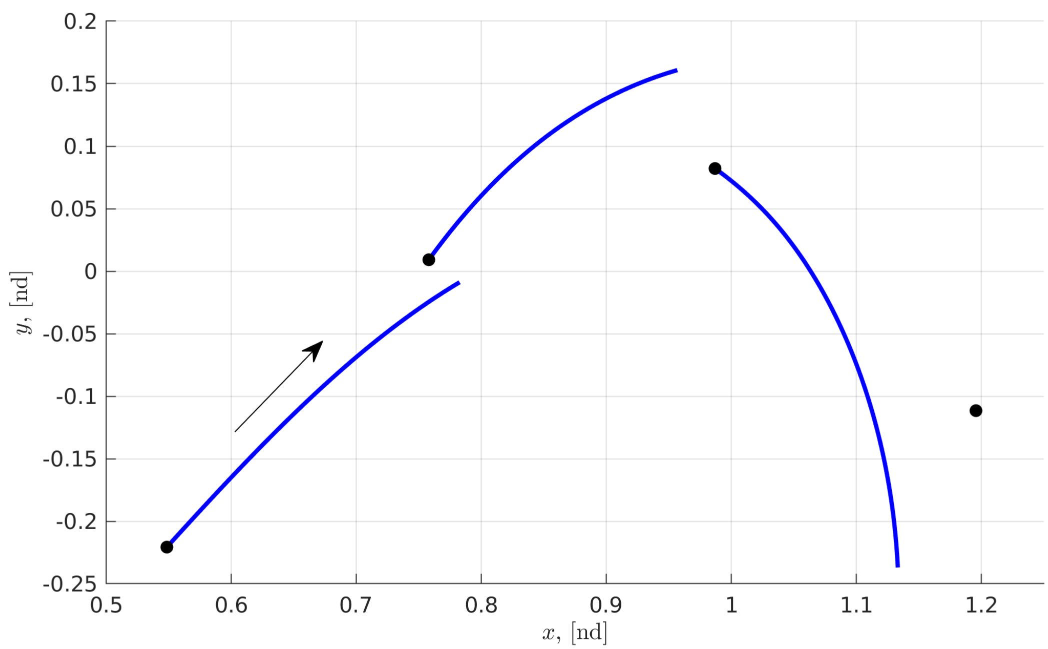

Figure 3.13. Patch Point Adjustment Following TLT Level-II

complete when constraints fall within the convergence criteria for both Level-I and Level-II.

Fundamental differences exist between the implementation and goals of Level-I and Level-II. In contrast to Level-I, which may consist of multiple local iterations for each global iteration, this Level-II step executes only once for each global iteration. Additionally, while Level-I is designed to reduce the norm of the constraint vector after each local iteration, the same may not be true of Level-II. Since position continuity is an assumption of Level-II, the function of Level-II is to reposition the patch points such that Level-II constraints are achieved when the position continuity is restored. The more visibly continuous slopes at the patch points are obvious in Figure 3.14, following the second global Level-I iteration. Thus, the velocity discontinuities

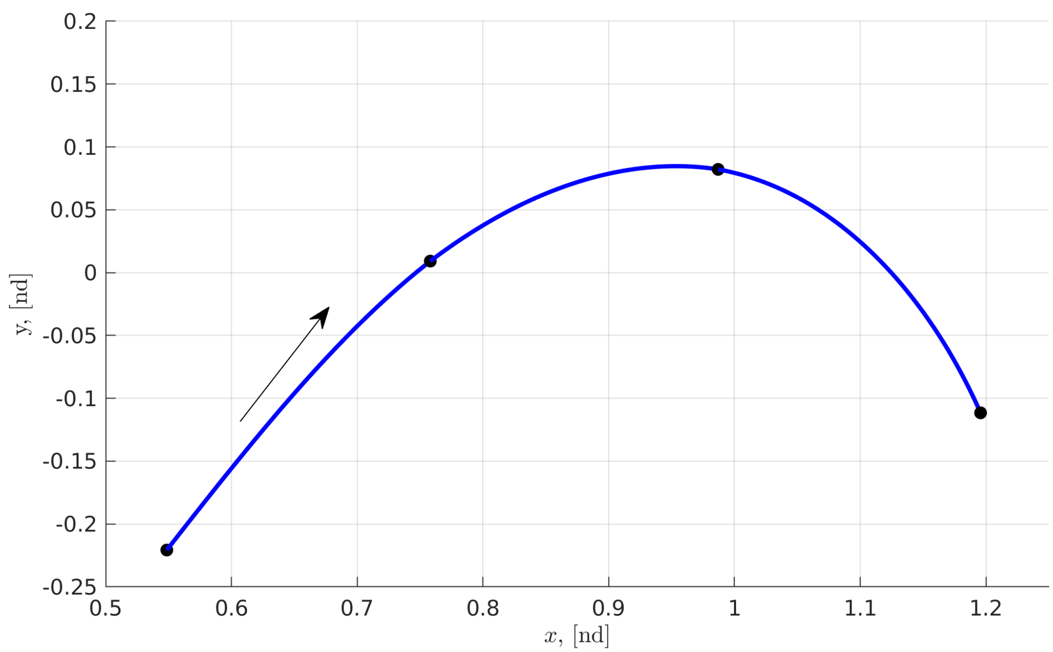

Figure 3.14. Position Convergence Following Second Level-I Iteration

may not reduce substantially immediately following a Level-II iteration; however, the benefit of the Level-II correction is expected to occur after reconvergence of Level-I.

4. Low-Thrust Two-Level Corrections

The *Two-Level Targeter with Low Thrust* (TLT-LT) expands the framework of the TLT algorithm framework to accommodate the additional complexity of low thrust propulsion systems. In this formulation, mass is added as a state variable due to the expenditure of propellant, and thrust magnitude and direction are also appended to the state vector as spacecraft control variables. The algorithm extends elements of the finite burn TLT, developed by Scarritt [9, 10], which seeks to model propulsive events as accelerations over finite time intervals to improve model fidelity.

4.1 Trajectory Type Classification

To facilitate inclusion of low thrust actuation into the two-level targeter, three types of arcs are defined: thrust, coast, and split. Illustrated in Figure 4.1, the thrust

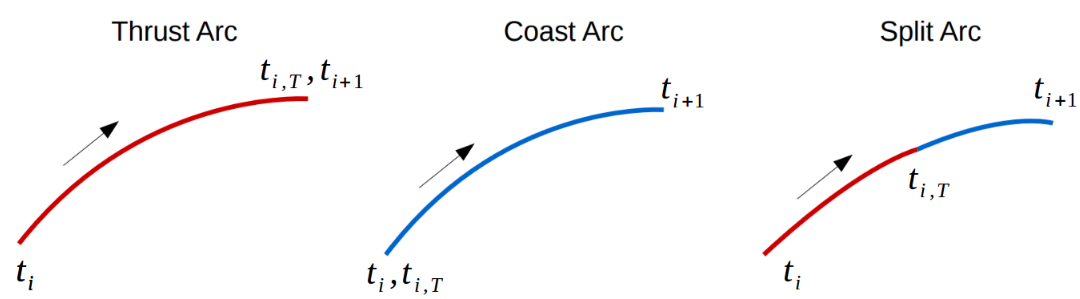

Figure 4.1. Three Arc Types in the TLT-LT

and coast arcs consist solely of thrust-aided and ballistic motion, respectively, over the entire arc duration from t_i to t_{i+1}. Introduced by Scarritt to apply continuous actuation over finite burn durations in the TLT [9, 10], the split arc type is defined by a thrust segment from initial time t_i to the thrust termination time $t_{i,T}$ and then a coast segment until t_{i+1}. For this investigation, thrust magnitude and direction are assumed constant along each thrust segment; however, these parameters can vary between thrust segments. For example, patch point $\mathcal{P}_1$ may include a different thrust magnitude than patch point $\mathcal{P}_2$, but neither thrust magnitude varies in time during the propagation of their respective arcs. However, the differential corrections process may modify these values at either patch point. Variables that satisfy this property of invariance internal to each arcs are denoted *arc-constant* variables.

All three arc types are defined as special examples of a split arc. A thrust arc is represented as a split arc where the burn termination time is the same as the arc termination time, i.e., $t_{i,T} = t_{i+1}$. Simiarly, a split arc with burn termination time equal to the initial time, i.e., $t_i = t_{i,T}$, functions as a coast arc. The simultaneous occurrence of burn termination and patch point times is shown in Figure 4.1 as times separated by a comma. The STM mapping variations between times t_i and t_{i+1} across a split arc is described as the product of STMs for the thrust and coast subarcs, mathematically expressed

$$\Phi(t_{i+1}, t_i) = \Phi(t_{i+1}, t_{i,T})\Phi(t_{i,T}, t_i) \tag{4.1}$$

based on the property of STMs in Equation (3.28). Over a coast arc, the thrust subarc-related $\Phi(t_{i,T}, t_i)$ maps variations over an instantaneous time interval and, therfore, $\Phi(t_{i,T}, t_i) = I$, using the property that an STM mapping variations from a time to itself is the identity matrix, demonstrated in Equation (3.27). Likewise, for a thrust arc, the coast subarc-related STM occurs over an instantaneous time interval, leading to $\Phi(t_{i+1}, t_{i,T}) = I$. Therefore, all three arc types and their STMs are represented using a split arc formulation, reducing algorithmic complexity.

4.2 Continuity Constraints

The baseline formulation of a two-level targeting algorithm incorporating low-thrust propulsion constrains position, velocity, and mass continuity. Consistent with the impulsive TLT, Level-I achieves position continuity, and Level-II targets velocity continuity at the patch points. Utilizing the additional control variables available in low thrust propulsion systems, Level-I includes thrust parameters as well as the initial velocity as design variables. In contrast, the design variables in Level-II, i.e., position and time, remain unchanged from the impulsive algorithm. Finally, mass continuity is enforced directly in Level-I by updating the mass of each patch point to be equal to the mass at the end of the incoming arc. This strategy of replacing the value for an arbitrary outgoing state, $\mathbf{x}_i^+$, with the value at the incoming state at the same patch point, $\mathbf{x}_i^-$, is labelled *feed-forward.* While additional constraints, e.g., altitude and orbital elements, may be added to the Level-II constraints, the default algorithm with only state continuity constraints is first developed.

4.2.1 Low Thrust Level-I

In general, the input to the TLT-LT consists of a discontinuous initial guess, discretized into three or more patch points, illustrated in Figure 4.2 where the red arrows indicate thrust direction and relative magnitude. Similar to the impulsive TLT Level-I, Level-I of the associated TLT-LT achieves positition continuity at patch point $\mathcal{P}_f$ through convergence of the constraint vector,

$$\mathbf{F}_I = \boldsymbol{\rho}_f^- - \boldsymbol{\rho}_f^+ \tag{4.2}$$

within a given tolerance, $\boldsymbol{\epsilon}_I$. As in the impulsive TLT, the TLT-LT Level-I process is completed in series with $\boldsymbol{\rho}_f^+$ assumed constant at each step. The design variable vector,

$$\mathbf{X}_I = \begin{bmatrix} \gamma_p^+ \\ \alpha_p^+ \\ \beta_p^+ \\ \boldsymbol{v}_p^+ \\ t_{p,T} \end{bmatrix} \tag{4.3}$$

is comprised of the outgoing thrust magnitude parameter, γ_p^+, thrust in-plane angle, α_p^+, thrust out-of-plane angle, β_p^+, and velocity, $\boldsymbol{v}_p^+$, at patch point $\mathcal{P}_p$. These thrust parameters are defined in Figure 2.4. The cut-off time for the burn segment following

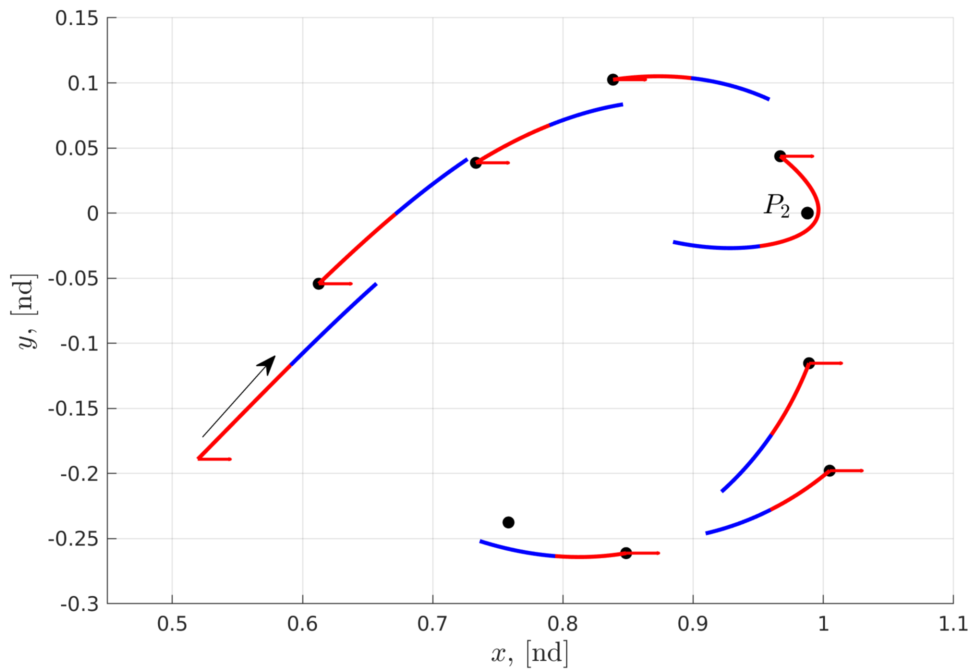

Figure 4.2. Initial Guess for the TLT-LT Example

$\mathcal{P}_p$ is designated $t_{p,T}$, as illustrated in Figure 4.1. For particular applications where varying velocity does not make sense from an operational perspective, e.g. the initial patch point based on the navigation state for an autonomous spacecraft in orbit, $\boldsymbol{v}_p^+$ is removed from the design vector, limiting the solution to a region reachable by only altering the burn parameters. However for early mission concept generation, allowing $\boldsymbol{v}_p^+$ to vary introduces an additional degree of freedom to explore solutions. These constraint and design variable vectors provide necessary components for the differential corrections procedure.

To initiate the differential corrections process, the linear relationship between the design variables and the constraints is defined. STMs are employed to compose the TLT-LT Level-I Jacobian,

$$\mathrm{D}\mathbf{F}_I = \frac{\partial(\boldsymbol{\rho}_f^- - \boldsymbol{\rho}_f^+)}{\partial \mathbf{X}_I} = \frac{\partial \boldsymbol{\rho}_f^-}{\partial \mathbf{X}_I} \tag{4.4}$$

for the differential corrections process. For the thrust arc leaving $\mathcal{P}_p$, the STM $\Phi(t_{p,T}, t_p)$ maps variations from the patch point to the end point following the thrust duration, mathematically represented as

$$\begin{bmatrix} \mathrm{d}\boldsymbol{\rho}_{p,T}^- - \boldsymbol{v}_{p,T}^- \,\mathrm{d}t_{p,T} \\ \mathrm{d}\boldsymbol{v}_{p,T}^- - \boldsymbol{a}_{p,T}^- \,\mathrm{d}t_{p,T} \\ \mathrm{d}m_{p,T}^- - \dot{m}_{p,T}^- \,\mathrm{d}t_{p,T} \\ \mathrm{d}\gamma_{p,T}^- - \dot{\gamma}_{p,T}^- \,\mathrm{d}t_{p,T} \\ \mathrm{d}\alpha_{p,T}^- - \dot{\alpha}_{p,T}^- \,\mathrm{d}t_{p,T} \\ \mathrm{d}\beta_{p,T}^- - \dot{\beta}_{p,T}^- \,\mathrm{d}t_{p,T} \end{bmatrix} = \begin{bmatrix} A_{pf} & B_{pf} & E_{pf} & F_{pf} & G_{pf} & H_{pf} \\ C_{pf} & D_{pf} & I_{pf} & J_{pf} & K_{pf} & L_{pf} \\ \vdots & & & & & \vdots \end{bmatrix} \begin{bmatrix} \mathrm{d}\boldsymbol{\rho}_p^+ - \boldsymbol{v}_p^+ \,\mathrm{d}t_p \\ \mathrm{d}\boldsymbol{v}_p^+ - \boldsymbol{a}_p^+ \,\mathrm{d}t_p \\ \mathrm{d}m_p^+ - \dot{m}_p^+ \,\mathrm{d}t_p \\ \mathrm{d}\gamma_p^+ - \dot{\gamma}_p^+ \,\mathrm{d}t_p \\ \mathrm{d}\alpha_p^+ - \dot{\alpha}_p^+ \,\mathrm{d}t_p \\ \mathrm{d}\beta_p^+ - \dot{\beta}_p^+ \,\mathrm{d}t_p \end{bmatrix} \tag{4.5}$$

Several assumptions allow simplification of this relationship. Thrust control variables are arc-constant with first derivatives fixed and equal to 0, i.e.,

$$\mathrm{d}\dot{\gamma} = \mathrm{d}\dot{\alpha} = \mathrm{d}\dot{\beta} = 0 \tag{4.6}$$

and the time at $\mathcal{P}_p$ is fixed ($\mathrm{d}t_p = 0$). Additionally, $\boldsymbol{\rho}_p^+$ and m_p^+ remain fixed, resulting in $\mathrm{d}\boldsymbol{\rho}_p^+ = \mathbf{0}$ and $\mathrm{d}m_p^+ = 0$. Finally, numerical methods propagate the subsequent coast subarc from the terminal position and velocity states of the thrust subarc; therefore,

$$\begin{aligned} \mathrm{d}\boldsymbol{\rho}_{p,T} &= \mathrm{d}\boldsymbol{\rho}_{p,T}^- = \mathrm{d}\boldsymbol{\rho}_{p,T}^+ \\ \mathrm{d}\boldsymbol{v}_{p,T} &= \mathrm{d}\boldsymbol{v}_{p,T}^- = \mathrm{d}\boldsymbol{v}_{p,T}^+ \end{aligned} \tag{4.7}$$

The reduced form of Equation (4.5),

$$\begin{bmatrix} \mathrm{d}\boldsymbol{\rho}_{p,T} - \boldsymbol{v}_{p,T} \,\mathrm{d}t_{p,T} \\ \mathrm{d}\boldsymbol{v}_{p,T} - \boldsymbol{a}_{p,T}^- \,\mathrm{d}t_{p,T} \\ \mathrm{d}m_{p,T}^- - \dot{m}_{p,T}^- \,\mathrm{d}t_{p,T} \\ \mathrm{d}\gamma_{p,T}^- \\ \mathrm{d}\alpha_{p,T}^- \\ \mathrm{d}\beta_{p,T}^- \end{bmatrix} = \begin{bmatrix} B_{pf} & F_{pf} & G_{pf} & H_{pf} \\ D_{pf} & J_{pf} & K_{pf} & L_{pf} \\ \vdots & & & \vdots \end{bmatrix} \begin{bmatrix} \mathrm{d}\boldsymbol{v}_p^+ \\ \mathrm{d}\gamma_p^+ \\ \mathrm{d}\alpha_p^+ \\ \mathrm{d}\beta_p^+ \end{bmatrix} \tag{4.8}$$

accommodates for these simplifying assumptions.

Following the burn end point $t_{p,T}$, another STM, $\Phi(t_f, t_{p,T})$, relates variations from the beginning of the coast arc to its termination. This mapping of contemporaneous variations, expressed

$$\begin{bmatrix} \mathrm{d}\boldsymbol{\rho}_f^- - \boldsymbol{v}_f^- \,\mathrm{d}t_f \\ \mathrm{d}\boldsymbol{v}_f^- - \boldsymbol{a}_f^- \,\mathrm{d}t_f \end{bmatrix} = \begin{bmatrix} \bar{A}_{pf} & \bar{B}_{pf} \\ \bar{C}_{pf} & \bar{D}_{pf} \end{bmatrix} \begin{bmatrix} \mathrm{d}\boldsymbol{\rho}_{p,T}^+ - \boldsymbol{v}_{p,T}^+ \,\mathrm{d}t_{p,T} \\ \mathrm{d}\boldsymbol{v}_{p,T}^+ - \boldsymbol{a}_{p,T}^+ \,\mathrm{d}t_{p,T} \end{bmatrix} \tag{4.9}$$

where the bar over submatrices reflects their origin as the coast subarc STM. Since the trajectory is ballistic across this coast subarc, thrust parameters and mass are removed. Since Level-I assumes fixed patch point times, the final time variation $\mathrm{d}t_f = 0$, and the continuity through the burn point defined by Equation (4.7), the mapping of contemporaneous across the coast subarc is simplified to

$$\begin{bmatrix} \mathrm{d}\boldsymbol{\rho}_f^- \\ \mathrm{d}\boldsymbol{v}_f^- \end{bmatrix} = \begin{bmatrix} \tilde{A}_{pf} & \tilde{B}_{pf} \\ \tilde{C}_{pf} & \tilde{D}_{pf} \end{bmatrix} \begin{bmatrix} \mathrm{d}\boldsymbol{\rho}_{p,T} - \boldsymbol{v}_{p,T} \,\mathrm{d}t_{p,T} \\ \mathrm{d}\boldsymbol{v}_{p,T} - \boldsymbol{a}_{p,T}^+ \,\mathrm{d}t_{p,T} \end{bmatrix} \tag{4.10}$$

Selecting the components relating to the Jacobian in Equation (4.4) yields the linear variational equation

$$\mathrm{d}\boldsymbol{\rho}_f^- = \bar{A}_{pf}(\mathrm{d}\boldsymbol{\rho}_{p,T} - \boldsymbol{v}_{p,T} \,\mathrm{d}t_{p,T}) + \bar{B}_{pf}(\mathrm{d}\boldsymbol{v}_{p,T} - \boldsymbol{a}_{p,T}^+ \,\mathrm{d}t_{p,T}) \tag{4.11}$$

With the inclusion of $\mathbf{X}_I$ terms in Equation (4.8) and $\mathbf{F}_I$ terms in Equation (4.11), the two equations can be linked. The expression $\mathrm{d}\boldsymbol{\rho}_{p,T} - \boldsymbol{v}_{p,T} \,\mathrm{d}t_{p,T}$ appears in both and is substituted directly. However, since the thrust magnitude changes from a non-zero to zero value across the transition from the thrust subarc to the coast subarc, the incoming and outgoing accelerations at $t_{p,T}$ are unequal, i.e., $\boldsymbol{a}_{p,T}^- \neq \boldsymbol{a}_{p,T}^+$. Therefore, the expression $\mathrm{d}\boldsymbol{v}_{p,T} - \boldsymbol{a}_{p,T}^+ \,\mathrm{d}t_{p,T}$ requires an algebriac manipulation,

$$\mathrm{d}\boldsymbol{v}_{p,T} - \boldsymbol{a}_{p,T}^+ \,\mathrm{d}t_{p,T} = \mathrm{d}\boldsymbol{v}_{p,T} - \boldsymbol{a}_{p,T}^- \,\mathrm{d}t_{p,T} + (\boldsymbol{a}_{p,T}^- - \boldsymbol{a}_{p,T}^+)\,\mathrm{d}t_{p,T} \tag{4.12}$$

that allows reformulation of Equation (4.11) as

$$\mathrm{d}\boldsymbol{\rho}_f^- = \bar{A}_{pf}(\mathrm{d}\boldsymbol{\rho}_{p,T} - \boldsymbol{v}_{p,T} \,\mathrm{d}t_{p,T}) + \bar{B}_{pf}(\mathrm{d}\boldsymbol{v}_{p,T} - \boldsymbol{a}_{p,T}^- \,\mathrm{d}t_{p,T}) + \bar{B}_{pf}(\boldsymbol{a}_{p,T}^- - \boldsymbol{a}_{p,T}^+)\,\mathrm{d}t_{p,T} \tag{4.13}$$

The expression $\mathrm{d}\boldsymbol{v}_{p,T} - \boldsymbol{a}_{p,T}^{-}\,\mathrm{d}t_{p,T}$ also appears in Equation (4.8), allowing for substitution to fully describe the constraint in terms of the design variables. By grouping terms, this map is expressed in matrix form,

$$\mathrm{d}\boldsymbol{\rho}_f^{-} = \mathrm{D}\mathbf{F}_I \begin{bmatrix} \mathrm{d}\gamma_p^{+} \\ \mathrm{d}\alpha_p^{+} \\ \mathrm{d}\beta_p^{+} \\ \mathrm{d}\boldsymbol{v}_p^{+} \\ \mathrm{d}t_{p,T} \end{bmatrix} \tag{4.14}$$

where the Jacobian is written

$$\begin{aligned} \mathrm{D}\mathbf{F}_I = [\bar{A}_{pf}F_{pf} + \bar{B}_{pf}J_{pf} \quad \bar{A}_{pf}G_{pf} + \bar{B}_{pf}K_{pf} \quad ... \\ \bar{A}_{pf}H_{pf} + \bar{B}_{pf}L_{pf} \quad \bar{A}_{pf}B_{pf} + \bar{B}_{pf}D_{pf} \quad \bar{B}_{pf}(\boldsymbol{a}_{p,T}^{-} - \boldsymbol{a}_{p,T}^{+})] \end{aligned} \tag{4.15}$$

Since the size of the vector $\mathbf{X}_I$ exceeds that of $\mathbf{F}_I$, the minimum-norm solution,

$$\mathrm{d}\mathbf{X}_I = -\mathrm{D}\mathbf{F}_I^T(\mathrm{D}\mathbf{F}_I\mathrm{D}\mathbf{F}_I^T)^{-1}\mathbf{F}_I \tag{4.16}$$

is employed to determine updates to the design vector.

Consistent with the impulsive TLT, this Newton process repeats for each local iteration until the constraint satisfies the convergence tolerance. Upon convergence, the Level-I algorithm is applied to the next arc in the series. An example of this continuity in position at the patch points is shown in Figure 4.3 where sharp corners illustrate the persisting discontinuity in velocity at the nodes. When position continuity is achieved for each arc, the algorithm continues to Level-II.

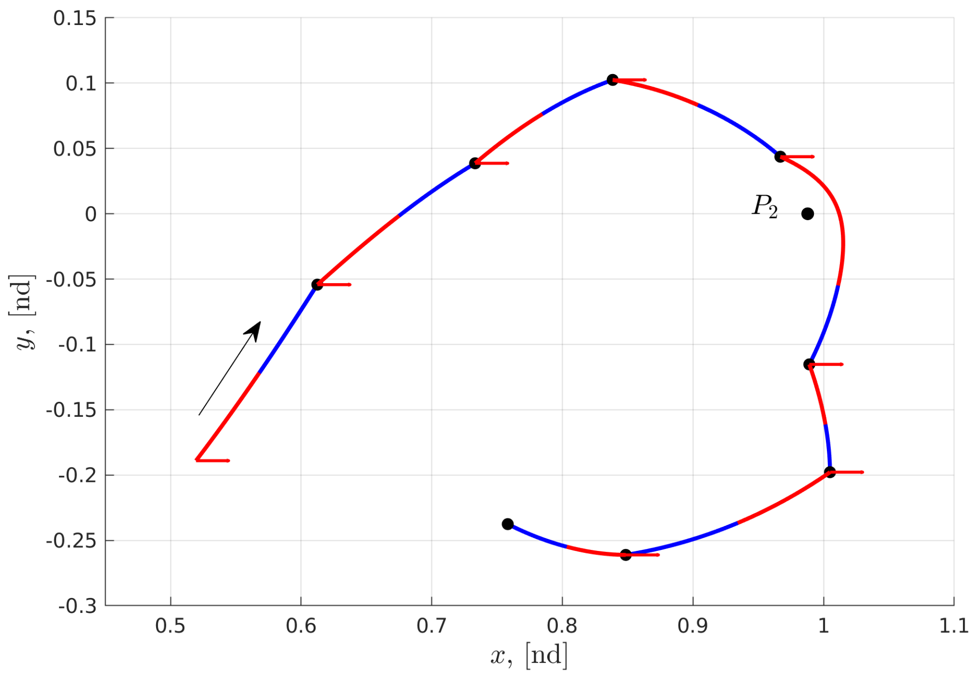

Figure 4.3. Position Continuity Following TLT-LT Level-I

4.2.2 Low Thrust Level-II

With the trajectory already continuous in position following Level-I, existing velocity discontinuities are corrected in Level-II. The TLT-LT Level-II process targets velocity continuity at all interior patch points, represented by the constraint vector,

$$\mathbf{F}_{II} = \begin{bmatrix} \boldsymbol{v}_2^- - \boldsymbol{v}_2^+ \\ \vdots \\ \boldsymbol{v}_{k-1}^- - \boldsymbol{v}_{k-1}^+ \end{bmatrix} \tag{4.17}$$

This constraint is achieved by updating a design vector,

$$\mathbf{X}_{II} = \begin{bmatrix} \boldsymbol{\rho}_1 \\ t_1 \\ \vdots \\ \boldsymbol{\rho}_k \\ t_k \end{bmatrix} \tag{4.18}$$

consisting of positions and times at all patch points. Because Level-I reduces position discontinuities to within ϵ_I, position continuity is assumed for the formulation of Level-II. Under this assumption, superscripts denoting incoming and outgoing position at a patch point are removed.

As with the impulsive Level-II derivation, the Jacobian $D\mathbf{F}_{II}$ is assembled in pieces. An interior patch point is denoted $\mathcal{P}_p$ with $\mathcal{P}_o$ and $\mathcal{P}_f$ as the preceeding and following patch points, respectively. States at $\mathcal{P}_p$ are assumed to be a function only of $\mathcal{P}_o$, $\mathcal{P}_p$, and $\mathcal{P}_f$. Using this notation, the constraint vector is rewritten

$$\mathbf{F}_{II} = \begin{bmatrix} \vdots \\ \boldsymbol{v}_p^- - \boldsymbol{v}_p^+ \\ \vdots \end{bmatrix} \tag{4.19}$$

focusing only on the patch point of interest. A corresponding reformulation of the design vector,

$$\mathbf{X}_{II} = \begin{bmatrix} \vdots \\ \boldsymbol{\rho}_o \\ t_o \\ \boldsymbol{\rho}_p \\ t_p \\ \boldsymbol{\rho}_f \\ t_f \\ \vdots \end{bmatrix} \tag{4.20}$$

includes only those design variables affecting the present constraint. The Level-II Jacobian,

$$\mathrm{D}\mathbf{F}_{II} = \begin{bmatrix} \vdots \\ \frac{\partial(\boldsymbol{v}_p^- - \boldsymbol{v}_p^+)}{\partial \mathbf{X}_{II}} \\ \vdots \end{bmatrix} = \begin{bmatrix} \vdots \\ \frac{\partial \boldsymbol{v}_p^-}{\partial \mathbf{X}_{II}} - \frac{\partial \boldsymbol{v}_p^+}{\partial \mathbf{X}_{II}} \\ \vdots \end{bmatrix} \tag{4.21}$$

is assembled row by row for each interior patch point $\mathcal{P}_p$ to complete the differential corrections procedure. To produce a row of the Jacobian matrix, arcs are propagated away from $\mathcal{P}_p$ to $\mathcal{P}_o$ and $\mathcal{P}_f$, and the resulting STMs provide contemporaneous variational mappings.

First, an arc is propagated backward in time from $\mathcal{P}_p$ to $\mathcal{P}_o$. Since forward-time arcs consist of a thrust then coast subarc, backward propagation will encounter these subarcs in reverse order. Rather than numerically integrating the equations of motion from t_p to $t_{o,T}$, a reasonable approximation,

$$\Phi(t_{o,T}, t_p) = \Phi(t_p, t_{o,T})^{-1} \tag{4.22}$$

from the property of STMs in Equation (3.29) allows the algorithm to propagate only forward in time for simplicity. For any patch point $\mathcal{P}_i$, position continuity is assumed following Level-I, i.e.,

$$\boldsymbol{\rho}_i = \boldsymbol{\rho}_i^- = \boldsymbol{\rho}_i^+ \tag{4.23}$$

and positon, velocity, and mass continuity is enforced through the burn point, i.e.,

$$\begin{aligned} \boldsymbol{\rho}_{i,T} &= \boldsymbol{\rho}_{i,T}^- = \boldsymbol{\rho}_{i,T}^+ \\ \boldsymbol{v}_{i,T} &= \boldsymbol{v}_{i,T}^- = \boldsymbol{v}_{i,T}^+ \\ m_{i,T} &= m_{i,T}^- = m_{i,T}^+ \end{aligned} \tag{4.24}$$

Another assumption holds burn times fixed, implying $\mathrm{d}t_{i,T} = 0$, throughout the Level-II corrections process. Using these assumptions, the STM supplies a mapping, described by

$$\begin{bmatrix} \mathrm{d}\boldsymbol{\rho}_{o,T} \\ \mathrm{d}\boldsymbol{v}_{o,T} \end{bmatrix} = \begin{bmatrix} \bar{A}_{po} & \bar{B}_{po} \\ \bar{C}_{po} & \bar{D}_{po} \end{bmatrix} \begin{bmatrix} \mathrm{d}\boldsymbol{\rho}_p - \boldsymbol{v}_p^- \,\mathrm{d}t_p \\ \mathrm{d}\boldsymbol{v}_p^- - \boldsymbol{a}_p^- \,\mathrm{d}t_p \end{bmatrix} \tag{4.25}$$

between variations across the coast subarc.

With variations across the coast subarc defined, variations over the preceeding thrust subarc are examined. The STM from $t_{o,T}$ to t_o along the thrust subarc provides the next transformation,

$$\begin{bmatrix} \mathrm{d}\boldsymbol{\rho}_o - \boldsymbol{v}_o^+ \,\mathrm{d}t_o \\ \mathrm{d}\boldsymbol{v}_o^+ - \boldsymbol{a}_o^+ \,\mathrm{d}t_o \\ \mathrm{d}m_o^+ - \dot{m}_o^+ \,\mathrm{d}t_o \\ \mathrm{d}\gamma_o^+ - \dot{\gamma}_o^+ \,\mathrm{d}t_o \\ \mathrm{d}\alpha_o^+ - \dot{\alpha}_o^+ \,\mathrm{d}t_o \\ \mathrm{d}\beta_o^+ - \dot{\beta}_o^+ \,\mathrm{d}t_o \end{bmatrix} = \begin{bmatrix} A_{po} & B_{po} & E_{po} & F_{po} & G_{po} & H_{po} \\ C_{po} & D_{po} & I_{po} & J_{po} & K_{po} & L_{po} \\ \vdots & & & & & \vdots \end{bmatrix} \begin{bmatrix} \mathrm{d}\boldsymbol{\rho}_{o,T} - \boldsymbol{v}_{o,T} \,\mathrm{d}t_{o,T} \\ \mathrm{d}\boldsymbol{v}_{o,T} - \boldsymbol{a}_{o,T}^- \,\mathrm{d}t_{o,T} \\ \mathrm{d}m_{o,T} - \dot{m}_{o,T}^- \,\mathrm{d}t_{o,T} \\ \mathrm{d}\gamma_{o,T}^- - \dot{\gamma}_{o.T}^- \,\mathrm{d}t_{o,T} \\ \mathrm{d}\alpha_{o,T}^- - \dot{\alpha}_{o,T}^- \,\mathrm{d}t_{o,T} \\ \mathrm{d}\beta_{o,T}^- - \dot{\beta}_{o,T}^- \,\mathrm{d}t_{o,T} \end{bmatrix} \tag{4.26}$$

mapping variations back to $\mathcal{P}_o$. However, further assumptions offer a more compact variational model. Again, burn times are fixed, setting their associated variations to zero. Additionally, thrust parameters are constant within Level-II, so all variations associated with γ, α, and β are set to zero. Noting that $\dot{m}_i^+$ is always negative or zero since the spacecraft is either expending mass or on a ballistic trajectory, the relationship between variations in time and mass is simplified by assuming the mass flow rate is constant in a CSI propulsion system. A positive change in t_o represents a shorter burn duration due to the constant burn end time $t_{o,T}$. Therefore, the contemporaneous variation in mass at $t_{o,T}$, is represented

$$\delta m_{o,T}^- = -\dot{m}_o^+ \,\mathrm{d}t_o \tag{4.27}$$

By including the above assumptions, a simplified relationship for variations across the thrust subarc may be determined, i.e.,

$$\begin{bmatrix} \mathrm{d}\boldsymbol{\rho}_o - \boldsymbol{v}_o^+ \,\mathrm{d}t_o \\ \mathrm{d}\boldsymbol{v}_o^+ - \boldsymbol{a}_o^+ \,\mathrm{d}t_o \\ \mathrm{d}m_o^+ - \dot{m}_o^+ \,\mathrm{d}t_o \end{bmatrix} = \begin{bmatrix} A_{po} & B_{po} & E_{po} \\ C_{po} & D_{po} & I_{po} \\ \vdots & & \vdots \end{bmatrix} \begin{bmatrix} \mathrm{d}\boldsymbol{\rho}_{o,T} \\ \mathrm{d}\boldsymbol{v}_{o,T} \\ -\dot{m}_o^+ \,\mathrm{d}t_o \end{bmatrix} \tag{4.28}$$

Extracting the components related to the design variables $\boldsymbol{\rho}_o$ and t_o results in a linear equation,

$$\begin{aligned} \mathrm{d}\boldsymbol{\rho}_o - \boldsymbol{v}_o^+ \, \mathrm{d}t_o = A_{po}(\bar{A}_{po}(\mathrm{d}\boldsymbol{\rho}_p - \boldsymbol{v}_p^- \, \mathrm{d}t_p) + \bar{B}_{po}(\mathrm{d}\boldsymbol{v}_p^- - \boldsymbol{a}_p^- \, \mathrm{d}t_p)) + ... \\ B_{po}(\bar{C}_{po}(\mathrm{d}\boldsymbol{\rho}_p - \boldsymbol{v}_p^- \, \mathrm{d}t_p) + \bar{D}_{po}(\mathrm{d}\boldsymbol{v}_p^- - \boldsymbol{a}_p^- \, \mathrm{d}t_p)) - E_{po}\dot{m}_o^+ \, \mathrm{d}t_o \end{aligned} \tag{4.29}$$

where substitutions for $\mathrm{d}\boldsymbol{\rho}_{o,T}$ and $\mathrm{d}\boldsymbol{v}_{o,T}$ originate with the coast subarc variational relationships in Equation (4.25). By grouping terms, the partial derivatives of $\boldsymbol{v}_p^-$ with respect to the design variables,

$$\begin{aligned} \frac{\partial \boldsymbol{v}_p^-}{\partial \boldsymbol{\rho}_o} &= (A_{po}\bar{B}_{po} + B_{po}\bar{D}_{po})^{-1} \\ \frac{\partial \boldsymbol{v}_p^-}{\partial \boldsymbol{\rho}_p} &= -(A_{po}\bar{B}_{po} + B_{po}\bar{D}_{po})^{-1}(A_{po}\bar{A}_{po} + B_{po}\bar{C}_{po}) \\ \frac{\partial \boldsymbol{v}_p^-}{\partial t_p} &= (A_{po}\bar{B}_{po} + B_{po}\bar{D}_{po})^{-1}(A_{po}\bar{A}_{po} + B_{po}\bar{C}_{po})\boldsymbol{v}_p^- + \boldsymbol{a}_p^- \\ \frac{\partial \boldsymbol{v}_p^-}{\partial t_o} &= (A_{po}\bar{B}_{po} + B_{po}\bar{D}_{po})^{-1}(E_{po}\dot{m}_o^+ - \boldsymbol{v}_o^+) \end{aligned} \tag{4.30}$$

are elements of the Jacobian corresponding to $\frac{\partial \boldsymbol{v}_p^-}{\partial \mathbf{X}_{II}}$.

To derive the partial derivatives of $\boldsymbol{v}_p^+$ that are required to complete the Jacobian $\mathrm{D}\mathbf{F}_{II}$, the trajectory from $\mathcal{P}_p$ to $\mathcal{P}_f$ is propagated forward in time. The general linear map of variations across the thrust subarc are modelled by the STM, mathematically described,

$$\begin{bmatrix} \mathrm{d}\boldsymbol{\rho}_{p,T} - \boldsymbol{v}_{p,T} \, \mathrm{d}t_{p,T} \\ \mathrm{d}\boldsymbol{v}_{p,T} - \boldsymbol{a}_{p,T}^- \, \mathrm{d}t_{p,T} \\ \mathrm{d}m_{p,T} - \dot{m}_{p,T}^- \, \mathrm{d}t_{p,T} \\ \mathrm{d}\gamma_{p,T}^- - \dot{\gamma}_{p,T}^- \, \mathrm{d}t_{p,T} \\ \mathrm{d}\alpha_{p,T}^- - \dot{\alpha}_{p,T}^- \, \mathrm{d}t_{p,T} \\ \mathrm{d}\beta_{p,T}^- - \dot{\beta}_{p,T}^- \, \mathrm{d}t_{p,T} \end{bmatrix} = \begin{bmatrix} A_{pf} & B_{pf} & E_{pf} & F_{pf} & G_{pf} & H_{pf} \\ C_{pf} & D_{pf} & I_{pf} & J_{pf} & K_{pf} & L_{pf} \\ \vdots & & & & & \vdots \end{bmatrix} \begin{bmatrix} \mathrm{d}\boldsymbol{\rho}_p - \boldsymbol{v}_p^+ \, \mathrm{d}t_p \\ \mathrm{d}\boldsymbol{v}_p^+ - \boldsymbol{a}_p^+ \, \mathrm{d}t_p \\ \mathrm{d}m_p^+ - \dot{m}_p^+ \, \mathrm{d}t_p \\ \mathrm{d}\gamma_p^+ - \dot{\gamma}_p^+ \, \mathrm{d}t_p \\ \mathrm{d}\alpha_p^+ - \dot{\alpha}_p^+ \, \mathrm{d}t_p \\ \mathrm{d}\beta_p^+ - \dot{\beta}_p^+ \, \mathrm{d}t_p \end{bmatrix} \tag{4.31}$$

before any simplifying assumptions. The thrust parameters and the burn time $t_{p,T}$ are again considered fixed throughout the Level-II procedure; therefore, their variations are set equal to zero. Similar to the mass relation described by Equation (4.27), the contemporaneous variation in mass at $\mathcal{P}_p$ is given by

$$\delta m_p^+ = -\dot{m}_p^+ \,\mathrm{d}t_p \tag{4.32}$$

Substituing in the mass relationship defined in Equation (4.32) and removing terms that are equal to zero, Equation (4.31) is expressed

$$\begin{bmatrix} \mathrm{d}\boldsymbol{\rho}_{p,T} \\ \mathrm{d}\boldsymbol{v}_{p,T} \\ \mathrm{d}m_{p,T}^- \end{bmatrix} = \begin{bmatrix} A_{pf} & B_{pf} & E_{pf} \\ C_{pf} & D_{pf} & I_{pf} \\ \vdots & & \vdots \end{bmatrix} \begin{bmatrix} \mathrm{d}\boldsymbol{\rho}_p - \boldsymbol{v}_p^+ \,\mathrm{d}t_p \\ \mathrm{d}\boldsymbol{v}_p^+ - \boldsymbol{a}_p^+ \,\mathrm{d}t_p \\ -\dot{m}_p^+ \,\mathrm{d}t_p \end{bmatrix} \tag{4.33}$$

and represents the reduced variational relationship across the thrust subarc from $\mathcal{P}_p$ to $\mathcal{P}_f$. The mapping of varations across the subsequent coast subarc, i.e.,

$$\begin{bmatrix} \mathrm{d}\boldsymbol{\rho}_f - \boldsymbol{v}_f^- \,\mathrm{d}t_f \\ \mathrm{d}\boldsymbol{v}_f^- - \boldsymbol{a}_f^- \,\mathrm{d}t_f \end{bmatrix} = \begin{bmatrix} \bar{A}_{pf} & \bar{B}_{pf} \\ \bar{C}_{pf} & \bar{D}_{pf} \end{bmatrix} \begin{bmatrix} \mathrm{d}\boldsymbol{\rho}_{p,T} \\ \mathrm{d}\boldsymbol{v}_{p,T} \end{bmatrix} \tag{4.34}$$

is expressed in a reduced form with $\mathrm{d}t_{p,T} = 0$.

An expression for the constraint variables in terms of the design variables is sought using substitution on components of Equations (4.33) and (4.34), representing the evolution of variations across the thrust and coast subarcs. The first row of the right side of Equation (4.34), i.e.,

$$\mathrm{d}\boldsymbol{\rho}_f - \boldsymbol{v}_f^- \,\mathrm{d}t_f = \bar{A}_{pf} \,\mathrm{d}\boldsymbol{\rho}_{p,T} + \bar{B}_{pf} \,\mathrm{d}\boldsymbol{v}_{p,T} \tag{4.35}$$

is expanded by substituting in Equation (4.33). This expansions yields a single linear expression relating variations in only the design and constraint variables, i.e.,

$$\begin{aligned} \mathrm{d}\boldsymbol{\rho}_f - \boldsymbol{v}_f^- \,\mathrm{d}t_f = \bar{A}_{pf}(A_{pf}(\mathrm{d}\boldsymbol{\rho}_p - \boldsymbol{v}_p^+ \,\mathrm{d}t_p) + B_{pf}(\mathrm{d}\boldsymbol{v}_p^+ - \boldsymbol{a}_p^+ \,\mathrm{d}t_p) - E_{pf}\dot{m}_p^+ \,\mathrm{d}t_p) + ... \\ \bar{B}_{pf}(C_{pf}(\mathrm{d}\boldsymbol{\rho}_p - \boldsymbol{v}_p^+ \,\mathrm{d}t_p) + D_{pf}(\mathrm{d}\boldsymbol{v}_p^+ - \boldsymbol{a}_p^+ \,\mathrm{d}t_p) - I_{pf}\dot{m}_p^+ \,\mathrm{d}t_p) \end{aligned} \tag{4.36}$$

By grouping terms, partial derivatives for $\boldsymbol{v}_p^+$ in terms of the design variables are expressed as

$$\begin{aligned}
\frac{\partial \boldsymbol{v}_p^+}{\partial \boldsymbol{\rho}_f} &= (\bar{A}_{pf}B_{pf} + \bar{B}_{pf}D_{pf})^{-1} \\
\frac{\partial \boldsymbol{v}_p^+}{\partial \boldsymbol{\rho}_p} &= -(\bar{A}_{pf}B_{pf} + \bar{B}_{pf}D_{pf})^{-1}(\bar{A}_{pf}A_{pf} + \bar{B}_{pf}C_{pf}) \\
\frac{\partial \boldsymbol{v}_p^+}{\partial t_f} &= -(\bar{A}_{pf}B_{pf} + \bar{B}_{pf}D_{pf})^{-1}\boldsymbol{v}_f^- \\
\frac{\partial \boldsymbol{v}_p^+}{\partial t_p} &= (\bar{A}_{pf}B_{pf} + \bar{B}_{pf}D_{pf})^{-1}((\bar{A}_{pf}A_{pf} + \bar{B}_{pf}C_{pf})\boldsymbol{v}_p^+ + (\bar{A}_{pf}E_{pf} + \bar{B}_{pf}I_{pf})\dot{m}_p^+) + \boldsymbol{a}_p^+
\end{aligned} \tag{4.37}$$

With partial derivatives for $\boldsymbol{v}_p^+$ and $\boldsymbol{v}_p^-$ expressed in terms of the design variables, a row of the Jacobian, defined in Equation (4.21) is constructed. This process is repeated for all interior patch points to construct the entire Jacobian for the multiple shooting corrections process. Similar to the impulsive TLT, a single Level-II correction is completed before returning to the iterative Level-I process. The dispersion of the patch points in position and time is illustrated in Figure 4.4, and the subsequent Level-I process significantly reduces velocity discontinuties when position continuity is acheived, as shown in Figure 4.5.

To simplify the addition of constraints to the Level-II process, a *hybrid* method is developed and employed by Harden and Spreen [11, 12]. The Level-II Jacobian is represented as the product of two matrices, mathematically described by

$$\mathrm{D}\mathbf{F}_{II} = UV \tag{4.38}$$

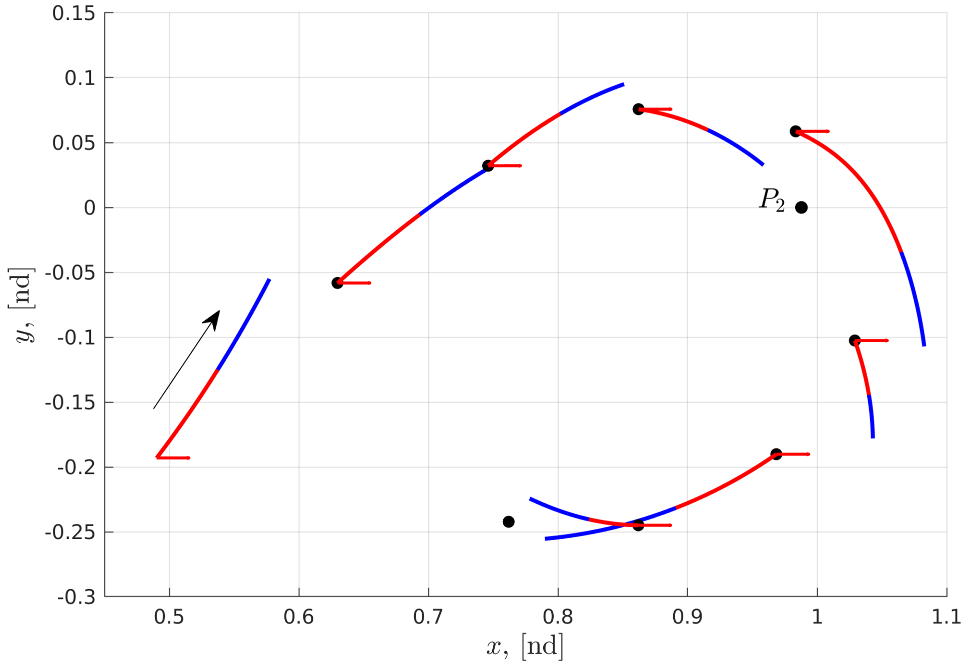

Figure 4.4. Patch Points Adjustment Following TLT-LT Level-II

which allows use of the chain rule of differentiation. An intermediate vector is introduced, i.e.,

$$\boldsymbol{\mathcal{X}}_{II} = \begin{bmatrix} \boldsymbol{v}_1^- \\ \boldsymbol{\rho}_1 \\ \boldsymbol{v}_1^+ \\ \vdots \\ \boldsymbol{v}_k^- \\ \boldsymbol{\rho}_k \\ \boldsymbol{v}_k^+ \\ t_1 \\ \vdots \\ t_k \end{bmatrix} \tag{4.39}$$

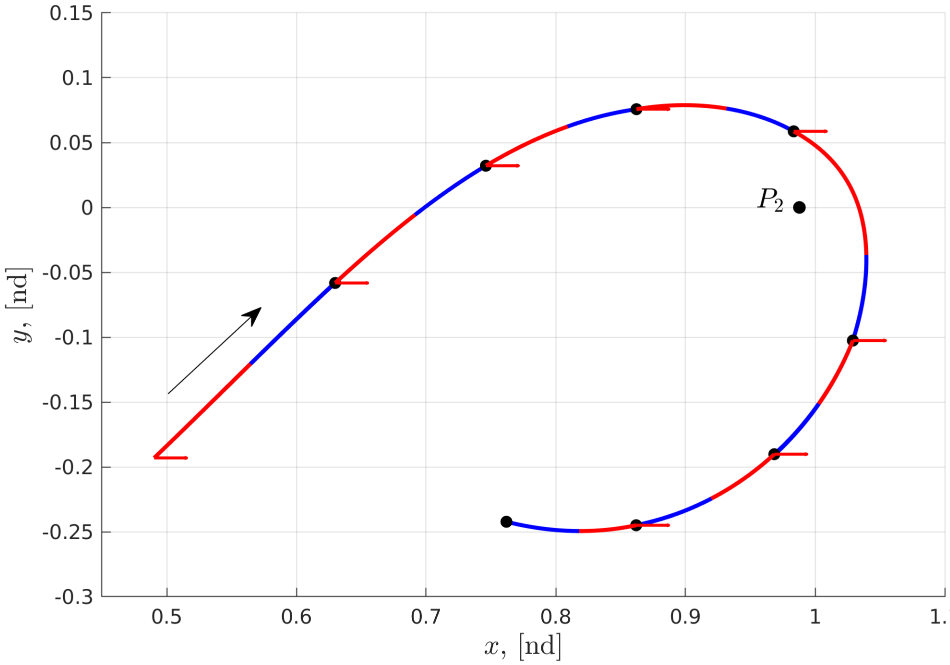

Figure 4.5. Position Continuity Following Second TLT-LT Level-I Iteration

including the complete set of state variables and times. The Jacobian of this intermediate vector with respect to $\mathbf{X}_{II}$, expressed

$$V = \frac{\partial \boldsymbol{\mathcal{X}}_{II}}{\partial \mathbf{X}_{II}} \tag{4.40}$$

consists of the partial derivatives already determined in Equations (4.37) and (4.30) as well as identities for trivial derivatives of states with respect to themselves. The Jacobian of $\mathbf{F}_{II}$ with respect to $\boldsymbol{\mathcal{X}}_{II}$ is defined

$$U = \frac{\partial \mathbf{F}_{II}}{\partial \boldsymbol{\mathcal{X}}_{II}} \tag{4.41}$$

as the explicit partial derivatives of the constraints with respect to the intermediate vector. For the baseline example constraining the interior patch point velocity continuity, elements of U consist only of positive and negative values of the identity matrix and zeros. Additional constraints formulated as functions of all states and times, i.e.,

$\boldsymbol{\mathcal{X}}$, may be appended to $\mathbf{F}_{II}$, resulting in changes only to U. With proper selection of the intermediate vector, the matrix V remains unchanged with the addition of constraints.

4.3 Additional Level-II Constraints

In addition to velocity continuity constraints, application-specific constraints are appended to the Level-II constraint vector. In this investigation, two constraints of interest are fixing a patch point to occur at an apse with respect to a primary body and defining a minimum altitude from a primary at a patch point. When combined, these constraints define a closest approach altitude for a fly-by of the primary.

First, the apse constraint is examined. An apse point with respect to a primary body is defined as a point where the position and velocity vectors with respect to that primary are orthogonal, i.e.,

$$F_{apse} = (\boldsymbol{\rho} - \boldsymbol{r}_i)^T \boldsymbol{v} = 0 \tag{4.42}$$

where $\boldsymbol{r}_i$ is the non-dimensional position vector from the barycenter to the primary of interest, P_i, and F_{apse} is defined as the apse constraint appended to $\mathbf{F}_{II}$. To construct the U matrix defined in Equation (4.41), the partial derivatives $\frac{\partial F_{apse}}{\partial \boldsymbol{\rho}}$ and $\frac{\partial F_{apse}}{\partial \boldsymbol{v}}$ are derived, i.e.,

$$\frac{\partial F_{apse}}{\partial \boldsymbol{\rho}} = \boldsymbol{v}^T \tag{4.43}$$

$$\frac{\partial F_{apse}}{\partial \boldsymbol{v}} = (\boldsymbol{\rho} - \boldsymbol{r}_i)^T \tag{4.44}$$

Thus, the Jacobian of the apse constraint with respect to design variables is defined.

An altitude constraint is defined as a minimum height, represented by the constant h, above the surface of P_i when the primary is modeled as a spherical body with radius R_i. Mathematically, this constraint is represented by the inequality

$$\sqrt{(\boldsymbol{\rho} - \boldsymbol{r}_i)^T (\boldsymbol{\rho} - \boldsymbol{r}_i)} \geq R_i + h \tag{4.45}$$

Without altering the function of the inequality, both sides are squared and multiplied by a factor of one half to aid in later differentiation steps, i.e.,

$$\frac{1}{2}(\boldsymbol{\rho} - \boldsymbol{r}_i)^T(\boldsymbol{\rho} - \boldsymbol{r}_i) \geq \frac{1}{2}(R_i + h)^2 \tag{4.46}$$

eliminating the need for computationally costly square root functions. However, the constraint does not appear in the form $F = 0$, and a new variable, ψ, denoted a *slack variable*, is introduced to formulate an equivalent equality constraint. The slack variable is appended to both $\mathcal{X}_{II}$ and $\mathbf{X}_{II}$. The product of any scalar and itself is a non-negative value; therefore, the inequality defined in Equation (4.46) has a valid reformulation

$$\frac{1}{2}(\boldsymbol{\rho} - \boldsymbol{r}_i)^T(\boldsymbol{\rho} - \boldsymbol{r}_i) - \frac{1}{2}(R_i + h)^2 = \frac{1}{2}\psi^2 \tag{4.47}$$

Rearranging such that the constraint takes the form $F = 0$ produces

$$F_{alt} = \frac{1}{2}(\boldsymbol{\rho} - \boldsymbol{r}_i)^T(\boldsymbol{\rho} - \boldsymbol{r}_i) - \frac{1}{2}(R_i + h)^2 - \frac{1}{2}\psi^2 = 0 \tag{4.48}$$

where F_{alt} denotes the altitude constraint scalar appended to the $\mathbf{F}_{II}$ vector. To append the U matrix, the partial derivatives of F_{alt} with respect to the design variables are given by

$$\frac{\partial F_{alt}}{\partial \boldsymbol{\rho}} = (\boldsymbol{\rho} - \boldsymbol{r}_i)^T \tag{4.49}$$

$$\frac{\partial F_{alt}}{\partial \psi} = -\psi \tag{4.50}$$

A similar procedure of reformulating inequality constraints into equality constraints in terms of slack variables is conducted for any similar inequality constraint.

5. Implementation Strategies

Along with the problem forumulation and derivation of partial derivatives outlined in previous chapters, the functional implementation of differential corrections algorithms plays a significant part in the calculated solution. Even with similar mathematical derivations, methods invoked in the algorithm to select a singular solution to underdetermined systems, deal with maintaining the forward progession of time between subarcs, and prime initial guesses to aid in covergence will yield different final trajectories. Applications of weighted minimum-norm solutions, attentuation factors, and forward-feeding state information are some examples of implementation choices that affect the converged trajectory solution.

Convergence behavior of a particular differential corrections strategy, consisting of constraint formulation methods, design variable weightings, and other algorithmic design choices, is highly dependent on the dynamical environment, patch point placement, initial discontinuity, and other factors inherent in the initial guess. Due to this sensitivity to the initial guess, this investigation does not endeavor to propose a single TLT-LT implementation strategy for all initial guesses. Rather, this investigation details several design options that may be employed to aid in determining suitable trajectories on a case-by-case basis.

5.1 Arc-Type Permanency

Whereas nearly-impulsive finite burn applications frequently leverage split arcs to model propulsive events, traditional low-thrust trajectory designs incorporate segments of entirely thrusting or coasting motion. In order to develop an algorithm appropriate for both paradigms, this investigation assumes that arc types remain fixed throughout the corrections process. For example, a thrust arc cannot be updated to a split or coast arc by this implementation of the TLT-LT algorithm. This feature of the algorithm is termed *arc-type permanency.*

With this design choice, the instananeous subarc, illustrated in Figure 4.1, that allows thrust and coast arcs to be modeled as special cases of a split arc requires further refinement, so additional assumptions on the accelerations within the instantaneous portions are applied. For a thrust arc originating at $\mathcal{P}_i$, accelerations over the infinitesmal time duration between $t_{i,T}^-$ and t_{i+1}^- are set equal to the value $\boldsymbol{a}_{i,T}^-$, reflecting the influencing of the acceleration due to thrust for the entire arc, i.e.,

$$\boldsymbol{a}_{i,T}^- = \boldsymbol{a}_{i,T}^+ = \boldsymbol{a}_{i+1}^-, \quad \text{for thrust arcs} \tag{5.1}$$

Similarly, accelerations from t_i^+ to $t_{i,T}^+$ are set equal to the value $\boldsymbol{a}_{i,T}^+$ if a coast arc originates from $\mathcal{P}_i$, i.e.,

$$\boldsymbol{a}_i^+ = \boldsymbol{a}_{i,T}^- = \boldsymbol{a}_{i,T}^+, \quad \text{for coast arcs} \tag{5.2}$$

Without these assumptions, the partial derivatives in Equations (4.30) and (4.37) from the TLT-LT Level-II include acceleration terms that do not accurately reflect the dynamics.

Along with reflecting current trajectory design practices, the implementation of arc-type permanency and its associated acceleration assumptions allow a single formulation of the TLT-LT Level-I D$\mathbf{F}_I$ matrix, given by Equation (4.4), which is applicable for all arc types. While all Level-I design variables are leveraged for split arcs, the thrust and coast arcs only benefit from a subset of the available variables, marked in Table 5.1. By implementing the assumptions defined in Equations (5.1) and (5.2), TLT-LT Level-I does not yield an update to $t_{p,T}$ for thrust and coast arcs, because the accelerations cancel out in the partial derivative, i.e.,

$$\frac{\partial \boldsymbol{\rho}_f}{\partial t_{p,T}} = \bar{B}_{pf}(\boldsymbol{a}_{p,T}^- - \boldsymbol{a}_{p,T}^+) = \mathbf{0} \tag{5.3}$$

Additionally, the Level-I update to thrust parameters (i.e., γ_p, α_p, β_p) is equal to zero for coast arcs, because the associated elements of the STM contain only zeros. Together, these features reflect the design variable limitations in Table 5.1 while keeping a fixed construction of the D$\mathbf{F}_I$ matrix.

Table 5.1. Applicable Level-I design variables by arc type

Arc Type	$\boldsymbol{v}_p^+$	γ_p	α_p	β_p	$t_{p,T}$
Thrust	•	•	•	•	
Coast	•				
Split	•	•	•	•	•

5.2 Local Lyapunov Exponent Weighted Corrections

The minimum-norm solution of an underconstrained linear system outlined in Equation (3.12) may not yield the appropriate change to the design vector for all applications, so additional methods to select from the infinite set of solutions are explored. By applying a symmetric positive definite weighting matrix, W, the optimization problem representing the weighted minimum-norm solution is formulated

$$\begin{aligned} &\text{Minimize} && \mathrm{d}\mathbf{X}^T W \,\mathrm{d}\mathbf{X} \\ &\text{Subject to} && \mathbf{F} = -\mathrm{D}\mathbf{F}\,\mathrm{d}\mathbf{X} \end{aligned} \tag{5.4}$$

to minimize the weighted norm of the design variable update vector while still satisfying the linear map derived from the Newton's method algorithm. The weighted norm is decomposed into

$$\begin{aligned} \mathrm{d}\mathbf{X}^T W \,\mathrm{d}\mathbf{X} &= \mathrm{d}\mathbf{X}^T W^{\frac{1}{2}} W^{\frac{1}{2}} \,\mathrm{d}\mathbf{X} \\ &= (W^{\frac{1}{2}} \,\mathrm{d}\mathbf{X})^T (W^{\frac{1}{2}} \,\mathrm{d}\mathbf{X}) \end{aligned} \tag{5.5}$$

where $W^{\frac{1}{2}}$ is the symmetric matrix inverse of W. This decomposition allows reformulation of the optimization problem in Equation (5.4), i.e.,

$$\begin{aligned} &\text{Minimize} && (W^{\frac{1}{2}} \,\mathrm{d}\mathbf{X})^T (W^{\frac{1}{2}} \,\mathrm{d}\mathbf{X}) \\ &\text{Subject to} && \mathbf{F} = -\mathrm{D}\mathbf{F}\,\mathrm{d}\mathbf{X} \end{aligned} \tag{5.6}$$

A cost functional, J_W, for the weighted minimum-norm optimization problem is defined

$$J_W = (W^{\frac{1}{2}} \,\mathrm{d}\mathbf{X})^T (W^{\frac{1}{2}} \,\mathrm{d}\mathbf{X}) + \boldsymbol{\lambda}^T (\mathrm{D}\mathbf{F}\,\mathrm{d}\mathbf{X} + \mathbf{F}) \tag{5.7}$$

with Lagrange multipliers, $\boldsymbol{\lambda}$. The derivatives of the cost functional with respect to the design vector update and Lagrange multipliers are set to zero, i.e.,

$$\left(\frac{\partial J_W}{\partial(\mathrm{d}\mathbf{X})}\right)^T = 2W\,\mathrm{d}\mathbf{X} - \mathrm{D}\mathbf{F}^T\boldsymbol{\lambda} = \mathbf{0} \tag{5.8}$$

$$\left(\frac{\partial J_W}{\partial\boldsymbol{\lambda}}\right)^T = \mathrm{D}\mathbf{F}\,\mathrm{d}\mathbf{X} + \mathbf{F} = \mathbf{0} \tag{5.9}$$

are set to zero. Rearranging Equation (5.8) into

$$\mathrm{d}\mathbf{X} = \frac{W^{-1}\mathrm{D}\mathbf{F}^T\boldsymbol{\lambda}}{2} \tag{5.10}$$

yields an expression for $\mathrm{d}\mathbf{X}$ which is substituted into Equation (5.9) to generate an expression for $\boldsymbol{\lambda}$, i.e.,

$$\boldsymbol{\lambda} = -2(\mathrm{D}\mathbf{F}W^{-1}\mathrm{D}\mathbf{F}^T)^{-1}\mathbf{F} \tag{5.11}$$

Equation (5.10), after algebriac manipulation to solve for the vector of Lagrange multipliers, is substituted into Equation (5.11) to generate the weighted minimum-norm solution which solves the optimization problem, expressed

$$\mathrm{d}\mathbf{X} = -W^{-1}\mathrm{D}\mathbf{F}^T(\mathrm{D}\mathbf{F}W^{-1}\mathrm{D}\mathbf{F}^T)^{-1}\mathbf{F} \tag{5.12}$$

By setting W equal to the identity matrix, the solution simplifies to the minimum-norm solution defined by Equation (3.12).

One strategy explored in this investigation for constructing a weighting matrix considers the sensitivity of each patch point to perturbations through the application of dynamical systems theory. While higher sensitivity to perturbations means smaller deviations from the initial guess are required to correct large discontinuities downstream, it is also frequently accompanied by higher nonlinearity and, therefore, more difficulty in applying linear corrections procedures to satisfy constraints. For this reason, making pertubations in highly sensitive regions of the trajectory more costly than those in less sensitive regions may aid in convergence.

Lyapunov exponents quantify the principal rates of expansion and contraction of infinitesimal perturbations from a reference trajectory over an infinite horizon time. Trajectories with larger Lyapunov exponents exhibit higher sensitivity and more chaotic downstream behavior due to small perturbations. Though theoretically significant, the numerical calculation of Lyapunov exponents over infinite horizon times is impractical, so an approximation over a finite horizon time, called the finite-time Lyapunov exponent (FTLE), provides a useful surrogate for sensitivity analysis. Explored by Harden and Spreen for its use in patch point placement algorithms [11, 12], the local Lyapunov exponent (LLE) is the maximum value within the FTLE spectrum, governing the dominant expansion mode. The LLE, Λ, is mathematically represented as

$$\Lambda = \frac{1}{|T_h|} \ln \|\Phi(T_h + t_0, t_0)\| \tag{5.13}$$

where T_h is the horizon time. The norm of the STM, defined

$$\|\Phi(T_h + t_0, t_0)\| = \sqrt{\max \operatorname{eig}(\Phi(T_h + t_0, t_0)^T \Phi(T_h + t_0, t_0))} \tag{5.14}$$

is the square root of the maximum eigenvalue calculated from the product of the transpose of the STM and itself. The LLE provides a useful metric for assessing the relative sensitivities of patch points and constructing weighting matrices.

Since the Level-II process involves simultaneous updates to several patch points through multiple shooting, the application of LLE-weighted corrections to Level-II is effective in biasing perturbations due to $\mathrm{d}\mathbf{X}_{II}$ toward less sensitive patch points in regions where linear approximations are generally more accurate. A weighting matrix, W_Λ, defined

$$W_\Lambda = \begin{bmatrix} \Lambda_1 I_{4\times4} & & 0 \\ & \ddots & \\ 0 & & \Lambda_k I_{4\times4} \end{bmatrix} \tag{5.15}$$

is constructed with Λ_i, the LLE value associated with each patch point $\mathcal{P}_i$, along the diagonal. Each LLE value is multiplied by the identity matrix, $I_{4\times4}$, to apply the weight to the three position components and one time variable. For interior patch points, Λ_i incorporates the trajectory ahead of and behind $\mathcal{P}_i$, reflecting the forward and backward propagation steps within Level-II, i.e.,

$$\Lambda_i = \frac{1}{|t_{i+1} - t_{i-1}|} \ln\|\Phi(t_{i+1}, t_i)\Phi(t_i, t_{i-1})\| \tag{5.16}$$

Since the first and final patch points exist at the boundaries of the trajectory, the LLE values associated with Λ_1 and Λ_k only incorporate the STM and horizon time for the first and final arcs, respectively.

5.3 Line Search Attentuation

In regions where nonlinear effects contribute significantly to the dynamics, the full design variable update vector calculated from the linear approximation of the system may negatively impact convergence behavior [13]. Modifying Equation (3.3), the attenuation factor, s, is a scalar applied to the update to the design vector that preserves the direction of the vector $\mathrm{d}\mathbf{X}$ while adjusting the magnitude, i.e.,

$$\mathbf{X}_{i+1} = \mathbf{X}_i + s\,\mathrm{d}\mathbf{X} \tag{5.17}$$

By adjusting the attenuation factor to reduce the magnitude of the correction in highly nonlinear regimes, the design vector is held to within a region that is more closely approximated by the linear system and more likely to result in a reduction in the constraint vector.

The process of selecting an appropriate value for s is called *line search attenuation*, because design vector is translated along the line generated by the vector $\mathrm{d}\mathbf{X}$. In this investigation, s is selected through an iterative process to ensure the Euclidean norm, $|\cdot|$, of the constraint vector is always reduced by an update to the design vector, i.e.,

$$|\mathbf{F}(\mathbf{X}_i + s\,\mathrm{d}\mathbf{X})| < |\mathbf{F}(\mathbf{X}_i)| \tag{5.18}$$

Starting with an initial value of $s = 1$ that represents a full step in $\mathrm{d}\mathbf{X}$, the constraint vector after the proposed update, $\mathbf{F}(\mathbf{X}_i + s\,\mathrm{d}\mathbf{X})$, is calculated and compared to the unperturbed vector, $\mathbf{F}(\mathbf{X}_i)$. If the current value of s does not result in satisfaction of the inequality defined in Equation (5.18), s is reduced, and the comparison is repeated. Until the inequality is satisfied, the values of $\mathbf{X}_i$ and d$\mathbf{X}$ remain fixed; only the value of s is updated.

Line search attenuation is most effectively applied to Level-I, where an immediate monotonic decrease in the constraint vector is expected. Because line search attenuation requires calculation of a new potential constraint vector and, therefore, propagation of the equations of motion with each iteration on s, the computational load of the algorithm is increased. It is recommended that the numerical integration of the states is implemented such that calculation of the STM, whether through numerical integration or finite difference methods, is optionally included, reducing the overall processing time when calculation of the STM is not required. In this investigation, an exponential equation for s in terms of the line search iteration, j, i.e.,

$$s = 0.8^j, \; j = 0, 1, 2, \ldots \tag{5.19}$$

is employed. Unlike a linear equation in terms of j, this formulation allows for an arbitrarily large number of iterations. Since the benefits of Level-II are generally only realized after reconvergence in position by a subsequent Level-I process, Level-II is not as well-suited for line search attenuation.

5.4 Design Variable Constraints

For a corrected solution to be a feasible spacecraft trajectory, the times associated with each subsequent patch point, t_i, and burn node, $t_{i,T}$, must increase, reflecting the forward flow of time. This necessary condition for time variables is mathematically described by

$$\ldots t_{i-1} \leq t_{i-1,T} \leq t_i \leq t_{i,T} \ldots \tag{5.20}$$

with the equality allowing for the instantaneous subarcs associated with thrust and coast arcs. Since this relationship between nodes and time is not captured in the governing differential equations or the general formulation of constraints in Level-I and Level-II of the TLT-LT, a method must be selected to enforce the constraint. In practice, there are multiple strategies for enforcing the inequality described in Equation (5.20). In particular, three methods are examined for suitability in this investigation: arc-type conversion, negligible offset, and design variable removal.

If a Level-I differential corrections step calculates a recommended update to the design vector that causes, for example, $t_{p,T}$ to exceed t_f on a split arc, then one option, denoted *arc-type conversion*, for handling this violation of the time inequality constraint is to have the burn fully saturate the segment as a thrust arc terminating at $t_f = t_{p,T}$. This method resolves the violation of Equation (5.20) by converting the arc type from split to thrust. However, this change in arc type violates the established assumption of arc-type permanency. Additionally, the acceleration assumptions described in Equations (5.1) and (5.2) do not allow for conversion of thrust or coast arcs into split arcs in subsequent iterations, because the partial derivative associated with updating the burn time $t_{p,T}$ is equal to zero. For these reasons, arc-type conversion is excluded from this investigation.

Another method, termed *negligible offset*, for enforcing the forward progression of time is by not applying the full update to the time variable if the constraint would be violated, and offseting it from its restricting neighbor by an arbitrarily small time increment. For example, the Level-I process recommends an update to the design vector, $\mathrm{d}\mathbf{X}_I$, which would cause $t_{p,T} > t_f$, violating the time constraint in Equation (5.20); instead, the algorithm sets $t_{p,T} = t_f - \epsilon_t$, where ϵ_t is an arbitrarily small time offset. A significant benefit of the negligible offset method is the ease of implementation. A simple logical test is required to determine if the full design vector update would violate the time constraint, and a truncated update is applied to the offending variable. However, one drawback is that the negligible offset method employs a suboptimal update to the design vector according to the linear approximation of the system, negatively impacting convergence behavior. Also, a violation of the forward time constraint may indicate a large flucuation in design variables and significant deviation from the initial guess. In this case, future iterations may be biased far away from the initial guess and toward split arcs with nearly all thrusting or coasting motion, which may not be preferred.

The *design variable removal* method addresses constraints on design variables by temporarily removing the the conflicting design variable from the design vector and calculating a new d$\mathbf{X}$ with the reduced set of variables. In the previous example, the original Level-I update caused $t_{p,T} > t_f$, violating Equation (5.20). To address this conflict, a new d$\mathbf{X}_I$ is determined without the influence of $t_{p,T}$. This action may be performed through reconstructing a new $\mathbf{X}_I$ vector and a new D$\mathbf{F}_I$ matrix. Alternatively, setting the elements of D$\mathbf{F}_I$ describing $\frac{\partial \mathbf{F}_I}{\partial t_{p,T}} = \mathbf{0}$, i.e.,

$$\begin{aligned} \mathrm{D}\mathbf{F}_I &= \begin{bmatrix} \frac{\partial \mathbf{F}_I}{\partial \gamma_p^+} & \frac{\partial \mathbf{F}_I}{\partial \alpha_p^+} & \frac{\partial \mathbf{F}_I}{\partial \beta_p^+} & \frac{\partial \mathbf{F}_I}{\partial \boldsymbol{v}_p^+} & \frac{\partial \mathbf{F}_I}{\partial t_{p,T}} \end{bmatrix} \\ &= \begin{bmatrix} \frac{\partial \mathbf{F}_I}{\partial \gamma_p^+} & \frac{\partial \mathbf{F}_I}{\partial \alpha_p^+} & \frac{\partial \mathbf{F}_I}{\partial \beta_p^+} & \frac{\partial \mathbf{F}_I}{\partial \boldsymbol{v}_p^+} & \mathbf{0} \end{bmatrix} \end{aligned} \tag{5.21}$$

produces the same result without requiring a full reconstruction of the matrix. A substantial benefit of design variable removal is that the recomputed design vector update produces the optimal linear correction to satisfy the constraint vector, improving convergence behavior. However, the recalculation of d$\mathbf{X}$ requires an additional matrix inversion and is more computationally intensive than the negligible offset method. Another benefit of design variable removal is that it is easily extendable to design variable constraints on other states. If a given application requires a position vector $\boldsymbol{\rho}_i$ to be fixed for example, the Level-II corrections procedure is altered to produce no update to d$\boldsymbol{\rho}_i$ by constructing the D$\mathbf{F}_{II}$ matrix as usual and then artificially setting $\frac{\partial \mathbf{F}_{II}}{\partial \boldsymbol{\rho}_i} = 0$. For these reasons, the design vector removal method for design variable constraints is employed when appropriate in this investigation.

6. Mission Applications

Since an objective of developing the TLT-LT is to produce an algorithm that is robust to a wide range of thrust magnitudes and mission types, three differing applications are selected for investigation. Additionally, the strategies employed to correct trajectories for the chosen mission scenarios explore a range of the implementation options detailed in the previous section. First, the motion of a spacecraft operating with a traditionally low-thrust propulsion system is corrected to depart from and arrive at periodic orbits about the L_1 and L_2 points. This example demonstrates robustness to long burn durations, boundary constraints, and the formulation of one method to calculate the partial derivatives for all arc types. The L_1-to-L_2 orbit transfer also illustrates the positive effect of LLE-weighted minimum-norm corrections for some applications. Next, a scenario based on NASA's Exploration Mission 1 trajectory [12] is examined to ensure the TLT-LT algorithm appropriately targets split arc solutions from impulsive initial guesses. The corrected trajectory achieves state continuity as well as additional operational constraints on flight path angle and altitude at fly-by maneuvers. Finally, a continuation of the finite burn EM-1 trajectory in spacecraft engine parameters to simulate a transition toward low-thrust solutions is performed. This application of the TLT-LT illustrates the power of the algorithm to apply two-level differential corrections engine parameters.

6.1 Lyapunov Low-Thrust Transfer

To demonstrate the effectiveness of the TLT-LT, a traditional low-thrust design for a transfer trajectory from a planar periodic orbit about the L_1 point point to a planar periodic orbit about the L_2 point within the CR3BP, defined by the dynamical model in Equation (2.23), is selected as a representative mission scenario. Obtained through methods described by Pritchett, Zimovan, and Howell [14], the initial guess, consisting of 53 patch points, is considered continuous in the CR3BP for a system defined by the characteristic quantities in Table 6.1 when thrust directions are arc-constant in an inertial reference frame. The transfer is performed by a low-thrust

Table 6.1. Characteristic Quantities for L_1-to-L_2 Transfer

Characteristic Length, l^*	Characteristic Time, t^*	Mass Parameter, μ
381,218.6885503592 km	4.2886837354572 days	0.012150584270572

spacecraft with mass and engine parameters described in Table 6.2. In this hypo-

Table 6.2. L_1-to-L_2 Transfer Spacecraft Parameters

Initial Mass, m_s^*	Specific Impulse, $\tilde{I}_{sp}$	Max. Thrust, $\tilde{T}_{max}$
1,000 kg	2,000 s	200 mN

thetical mission scenario, suppose operational constraints require thrust direction to instead be arc-constant in the P_1-P_2 rotating frame. This change introduces an initial guess, illustrated in Figure 6.1, with discontinuities in position and velocity at the patch points, so targeting with the TLT-LT is necessary. For translation into the TLT-LT framework, this trajectory consists only of thrust and coast arc types, reflecting existing trends in low thrust trajectory design, and employs the arc-type permanency assumption, requiring all thrust and coast arcs remain such throughout the corrections process.

The trajectory is constrained in both the internal state continuity as well as the boundary conditions. Level-I and Level-II of the TLT-LT deliver convergence of internal position and velocity discontinuities to within specified convergence tolerances, respectively. The initial norms of the discontinuities in position and velocity at each patch point are plotted in Figures 6.2 and 6.3. The maximum initial position and

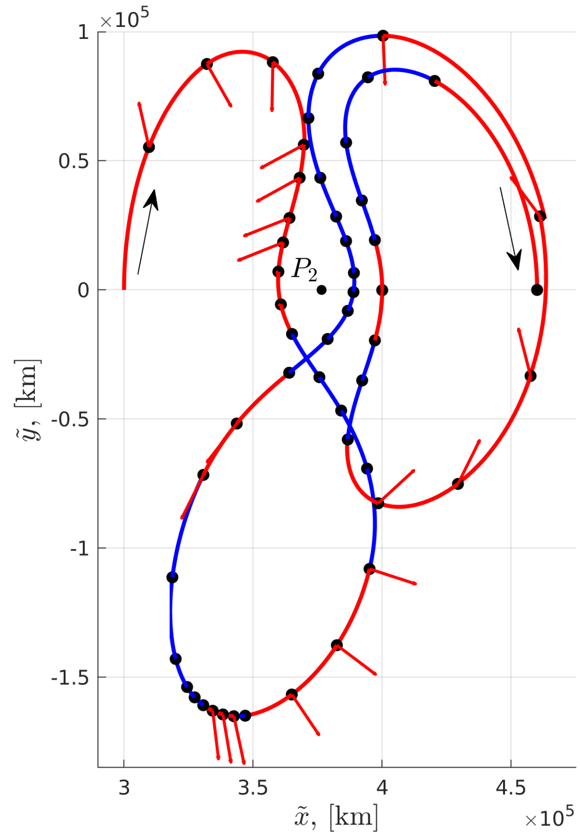

Figure 6.1. Low-Thrust Transfer Between Periodic Orbits About L_1 and L_2 with Arc-Constant Thrust Direction in the Rotating Frame

velocity discontinuities are approximately $2,201.029$ km and 23.526 m/s, respectively. Constraints on the position and velocity boundary conditions are enforced to ensure the initial patch point, $\mathcal{P}_1$, is located on the L_1 Lyapunov orbit with a Jacobi Constant of 3.03339347 non-dimensional units and the final patch point, $\mathcal{P}_k$, is located on the L_2 Lyapunov orbit with a Jacobi Constant of 3.05089416 non-dimensional units. To address these boundary constraints, multiple techniques are employed. Velocity

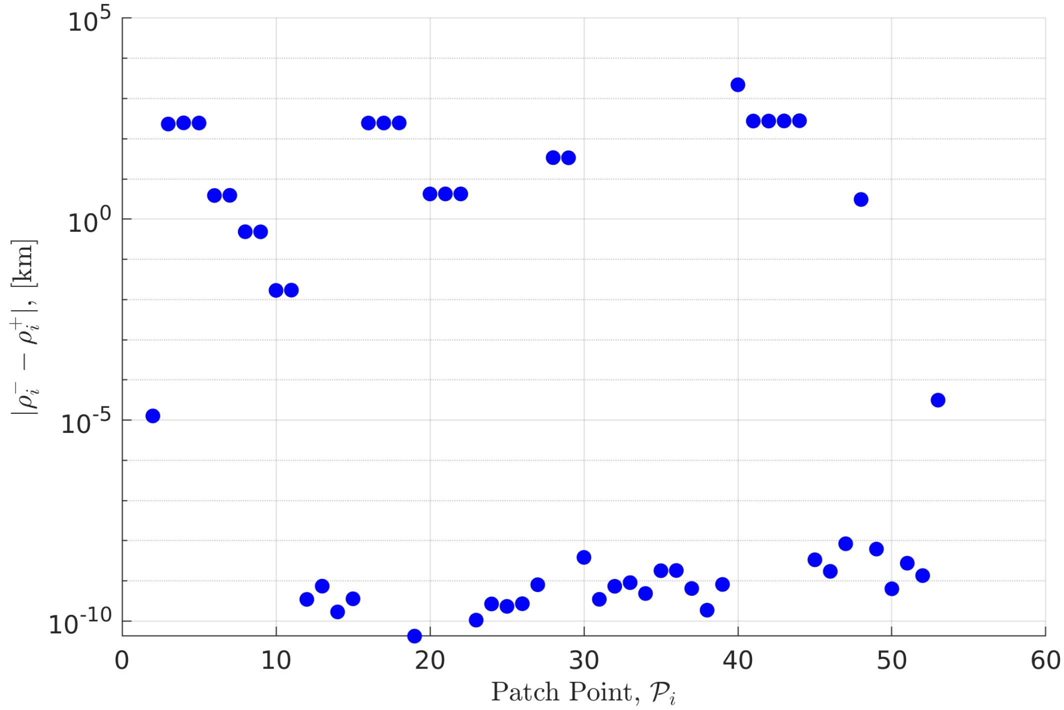

Figure 6.2. Norm of the Initial Position Discontinuity at each Patch Point, $\mathcal{P}_i$, for the Low-Thrust Transfer between Periodic Orbits About L_1 and L_2 in Dimensional Units

continuity at the initial and final patch points is enforced in Level-II by supplementing the F_{II} vector with the initial and final velocity contraints, i.e.,

$$\begin{aligned} \boldsymbol{v}_{1,d}^- - \boldsymbol{v}_1^+ &= \mathbf{0} \\ \boldsymbol{v}_k^- - \boldsymbol{v}_{k,d}^+ &= \mathbf{0} \end{aligned} \tag{6.1}$$

where $\boldsymbol{v}_{1,d}^-$ represents the desired departing velocity on the L_1 periodic orbit, and $\boldsymbol{v}_{k,d}^+$ denotes the desired arriving velocity on the L_2 periodic orbit. To fix the initial and final position states, the design variable removal method is employed on the D$\mathbf{F}_{II}$ matrix, setting all partial derivatives related to $\boldsymbol{\rho}_1$ and $\boldsymbol{\rho}_k$ to 0. Therefore, the update to the design vector calculated in the Level-II process will not include any updates to $\boldsymbol{\rho}_1$ or $\boldsymbol{\rho}_k$. For this application, the TLT-LT iterates until the norm of each

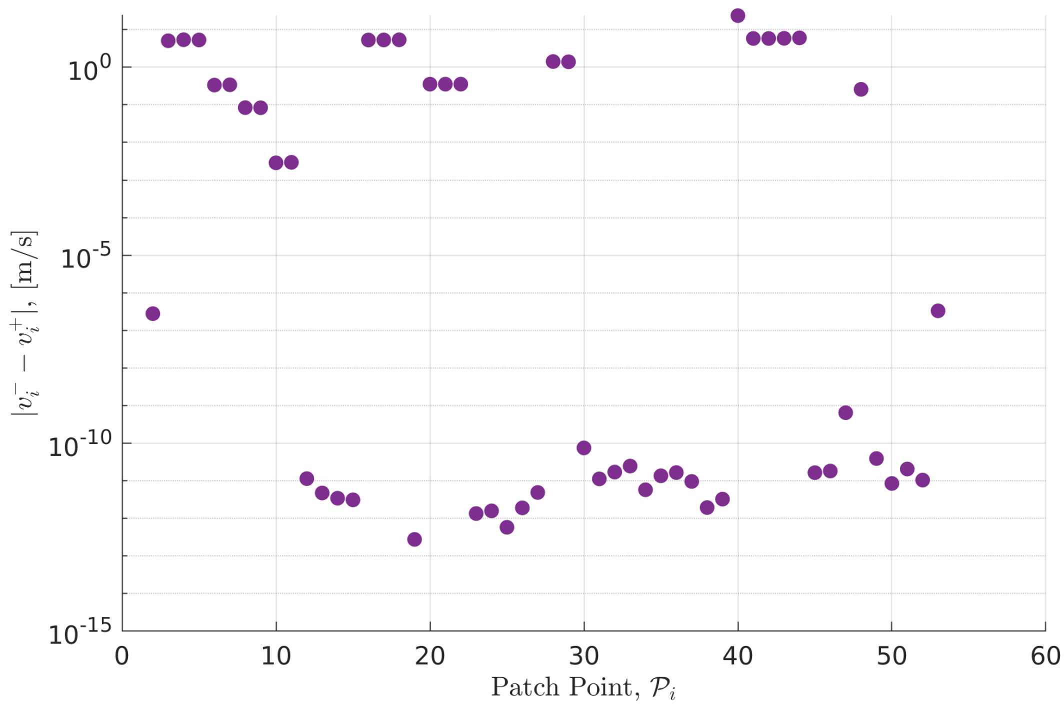

Figure 6.3. Norm of the Initial Velocity Discontinuity at Each Patch Point, $\mathcal{P}_i$, for the Low-Thrust Transfer Between Periodic Orbits About L_1 and L_2 in Dimensional Units

position and velocity discontinuity falls below the position and velocity discontinuity tolerances, ρ_{tol} and v_{tol}, respectively, provided in Table 6.3 in dimensional and non-dimensional units. By formulating constraints and tolerances for the problem in this

Table 6.3. State Discontinuity Tolerances for the L_1-to-L_2 Low-Thrust Transfer

Tolerance	Non-Dimensional	Dimensional (approx.)
ρ_{tol}	1×10^{-8} n.d.	3.812 m
v_{tol}	1×10^{-6} n.d.	1.029 mm/s

way, the resulting trajectory is a functionally-continuous low-thrust transfer between the two desired periodic orbits.

The convergence behavior and solutions of two design variable weighting strategies are compared for this mission scenario. First, a solution is determined by executing the TLT-LT process without applying any additional weights to the design variables. Second, LLE weighting, defined in Equation (5.15), is applied to the Level-II corrections procedure, and another solution is calculated from the original initial guess. The LLE values, Λ_i, applied at each patch point $\mathcal{P}_i$ are normalized by the lowest LLE, Λ_{min}, and plotted in Figure 6.4. This normalization allows for direct comparison with

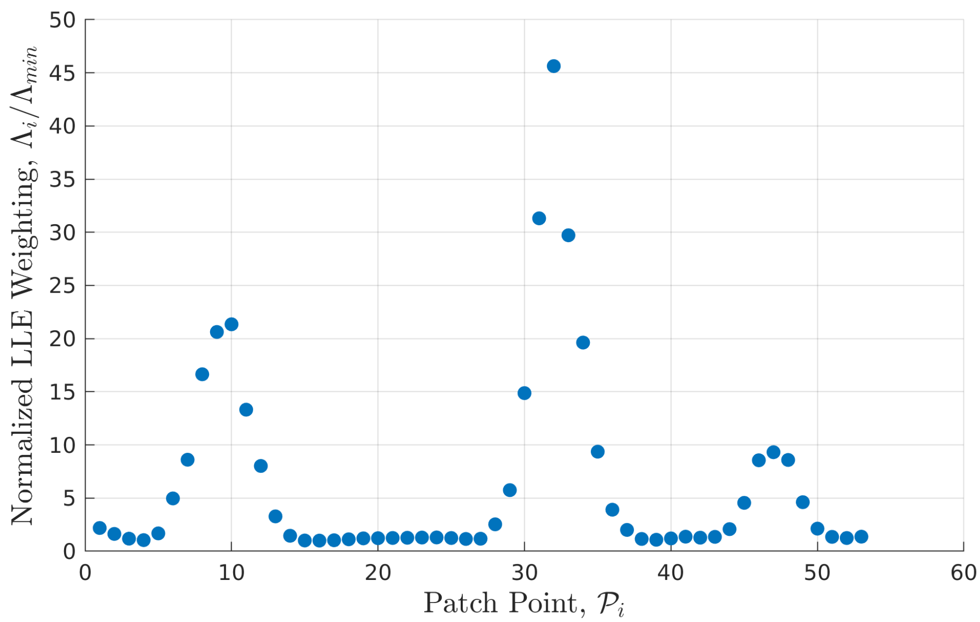

Figure 6.4. Normalized LLE Weights

the unweighted case that is equivalent to a weight of $\Lambda_i = 1$ for all patch points. The three peaks evident in the plot correspond to the high dynamical sensitivity of the three close approaches of P_2. By weighting changes in design variables at these patch points more heavily through Λ_i, the differential corrections process is expected to move these patch points less in the weighted solution.

Though the forms of the solutions are similar, the effect of weighting the Level-II process according to the LLEs is reflected in the resulting trajectories and their convergence behavior. The unweighted and weighted solutions appear in Figures 6.5(a) and 6.5(b), respectively. The movement of patch points between the initial guess and

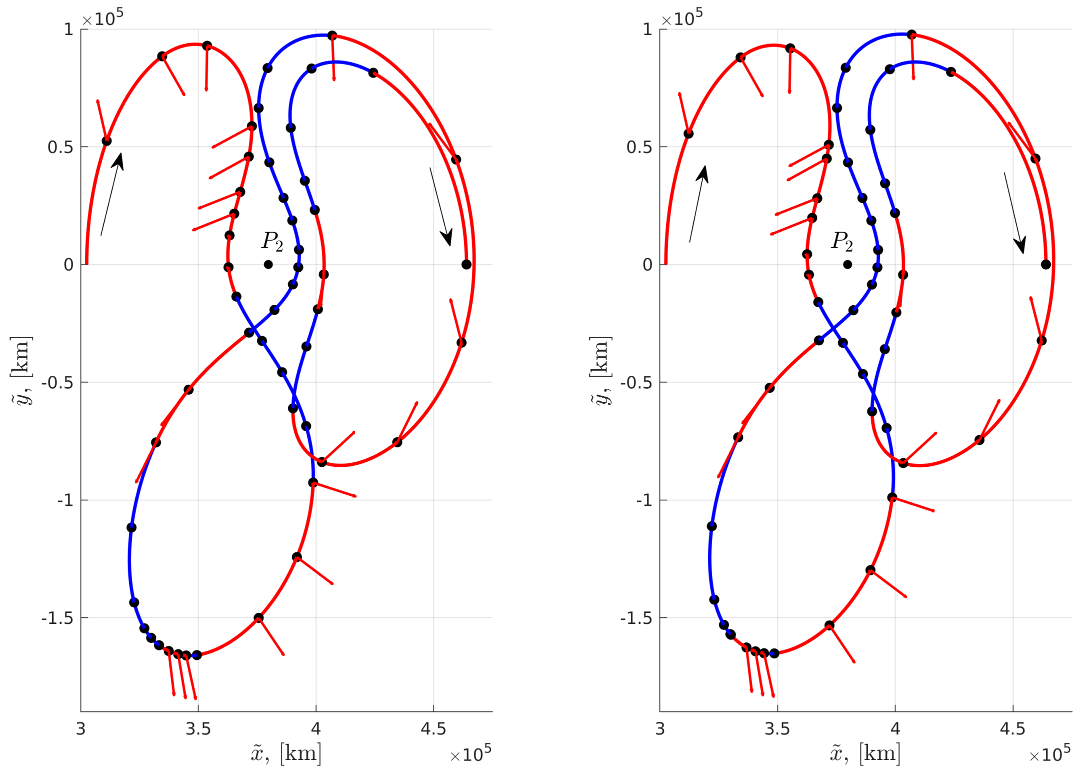

(a) No LLE Weighting

(b) LLE Weighting

Figure 6.5. Corrected Transfers from L_1 to L_2 Periodic Orbits in the CR3BP with and without LLE Weighting

converged solution follows the expected behavior, where the LLE-weighted corrections process results in less change for the patch points in dynamically sensitive regions. This behavior is demonstrated by visually comparing the patch point locations on the first close approach to P_2. In this region, the weighted patch points in Figure 6.5(b) show less deviation from the initial guess, shown in Figure 6.1, than their unweighted counterparts in Figure 6.5(a). In terms of mass expenditure, a critical metric for comparing trajectories, both the unweighted and weighted solutions perform similarly, as shown in Table 6.4. For this application, however, convergence behavior tends to

Table 6.4. Mass Expenditure and Convergence Performance for the L_1-to-L_2 Low-Thrust Transfer

Weighting	Mass Expended, kg	Iterations
Unweighted	21.846011	6
LLE-Weighted	21.759307	5

improve with the inclusion of LLE-weighting in the Level-II corrections process. The trajectory calculated through LLE-weighting converges on a trajectory which satisfies the constraints within their tolerances in one fewer iteration, also described in Table 6.4.

Overall, the L_1-to-L_2 low-thrust transfer application demonstrates the ability of the TLT-LT to sucessfully correct discontinuous low-thrust trajectories with interior and boundary constraints. In addition, this example validates the modelling of thrust and coast arcs with generalized partial derivatives as special cases of split arcs. Finally, the reduction in iterations required to obtain a corrected trajectory through the inclusion of an LLE-weighted minimum norm solution in the Level-II process suggests that some applications benefit from this dynamical systems-based approach.

6.2 Translunar Finite Burn Mission

To verify that the TLT-LT algorithm also effectively targets finite burn trajectories with high thrust magnitudes, a mission scenario similar to the first planned uncrewed mission for the Orion spacecraft, Exploration Mission 1 (EM-1), is investigated. Set in the CR3BP, the initial guess reflects existing models of the EM-1 trajectory [12,15–17]. The spacecraft, with mass and engine parameters are detailed in Table 6.5, follows a translunar path from near the Earth to an outbound powered fly-by (OPF) of the Moon and is inserted into a trajectory that approximates motion near a distant retrograde orbit (DRO) through a DRO insertion (DRI) maneuver. The subsequent

Table 6.5. EM-1 Spacecraft Parameters

Initial Mass, m_s^*	Specific Impulse, $\tilde{I}_{sp}$	Max. Thrust, $\tilde{T}_{max}$
25,000 kg	316 s	26.7 kN

DRO departure (DRD) burn puts the spacecraft on a path that leads to a return powered fly-by (RPF), which puts the vehicle on a return trajectory to the vicinity of Earth. Derived from the work of Spreen, an illustration of this trajectory with burns modeled as impulsive changes in velocity and marked as red patch points is shown in Figure 6.6 [12]. With characteristic quantities of the CR3BP system outlined in

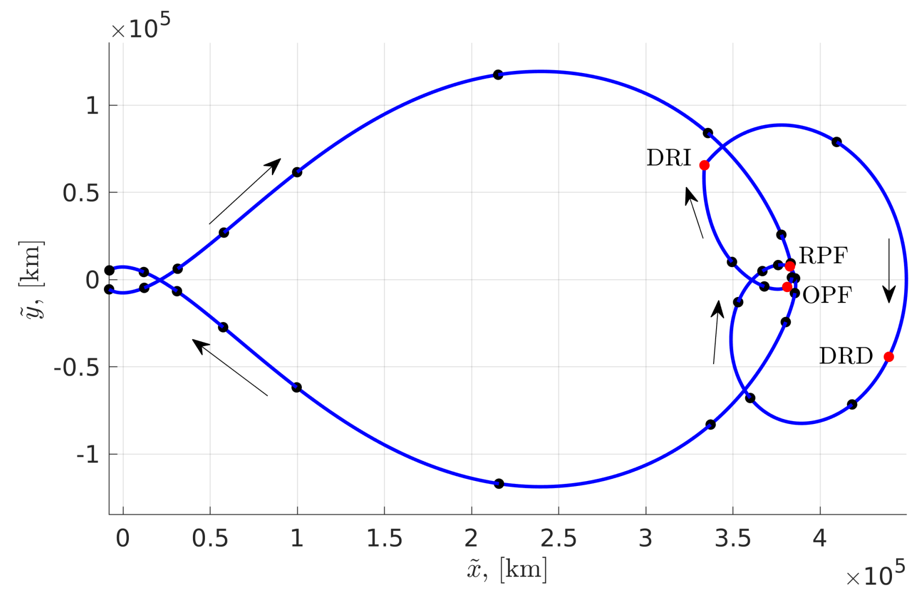

Figure 6.6. Impulsive EM-1 Initial Guess

Table 6.6, this impulsive representation of the EM-1 trajectory is determined through the use of the impulsive TLT by allowing velocity discontinuities at the patch points associated with the OPF, DRI, DRD, and RPF burns.

Table 6.6. EM-1 Characteristic Quantities

Characteristic Length, l^*	Characteristic Time, t^*	Mass Parameter, μ
384,400 km	4.3424798440226 days	0.012150586550569

For this sample mission scenario, the TLT-LT is used to determine a solution with finite burn durations from the impulsive initial guess shown in Figure 6.6. The resulting trajectory is constrained to be contininuous in position, velocity, and mass for the interior patch points. Additional constraints at the boundary conditions and close approaches to the Moon at OPF and RPF are added to the problem to simulate operational constraints on a spacecraft trajectory. First, the F_{II} constraint vector is augmented with a constraints, defined in Equation (4.42), which force the OPF and RPF burns to begin at apse points. Additionally, altitude constraints, defined in Equation (4.48) with slack variables, force the OPF and RPF burns to occur at the minimum lunar altitude $h = 100$ km. Representing an in-flight autonomous spacecraft leaving the vicinity of Earth, the initial position and velocity, detailed in Table 6.7, are fixed. The initial velocity, $\boldsymbol{v}_1^+$, is removed from the available set of design variables

Table 6.7. EM-1 Initial Conditions

Component	$\tilde{\boldsymbol{\rho}}_1^+$, km	$\tilde{\boldsymbol{v}}_1^+$, km/s
$\hat{x}$	$-8,059.936$	9.348311
$\hat{y}$	$-5,612.074$	-5.645644

for the Level-I process, and the algorithm only updates thrust parameters and burn duration at the first patch point, mimicking the control inputs available to a spacecraft in operation. This additional burn at the beginning of the trajectory is named the post-translunar injection (Post-TLI) correction burn. Defined in Table 6.8, the final patch point is constrained to have a constant position, $\boldsymbol{\rho}_k^-$, but variable velocity, $\boldsymbol{v}_k^-$, simulating the freedom to move along a target line at reentry. The fixing of $\boldsymbol{\rho}_1$ and

Table 6.8. EM-1 Terminal Conditions

Component	$\tilde{\boldsymbol{\rho}}_k^+$, km	$\tilde{\boldsymbol{v}}_k^+$, km/s
$\hat{x}$	$-7,886.840$	-9.607406
$\hat{y}$	$5,256.335$	-5.896723

$\boldsymbol{\rho}_k$ is done through design variable removal in the Level-II process.

The TLT-LT determines that convergence has been achieved when inequalities related to the above constraints have been satisified, i.e.,

$$\begin{gathered} |\boldsymbol{\rho}_i^- - \boldsymbol{\rho}_i^+| < \rho_{tol} \\ |\boldsymbol{v}_i^- - \boldsymbol{v}_i^+| < v_{tol} \\ \frac{(\boldsymbol{\rho}_j - \boldsymbol{\rho}_{P_2})^T \boldsymbol{v}_j}{|\boldsymbol{\rho}_j - \boldsymbol{\rho}_{P_2}| v_j} < \epsilon_{apse} \\ |\boldsymbol{\rho}_j - \boldsymbol{\rho}_{P_2}| - (R_{P_2} + h) > 0 \end{gathered} \tag{6.2}$$

with the position, velocity, and apse condition tolerances recorded in Table 6.9. The subscript j denotes only the applicable patch points for those constraints, i.e., OPF and RPF. By assuming RPF and OPF are already close to the apse condition, the

Table 6.9. EM-1 Tolerances

Tolerance	Non-Dimensional	Dimensional (approx.)
ρ_{tol}	1×10^{-8} n.d.	3.844 m
v_{tol}	1×10^{-6} n.d.	1.025 mm/s
ϵ_{apse}	1.7453×10^{-5} n.d.	0.001 deg

horizontal flight path angle satisfies the small angle approximation that the sine of angle is equal to the angle itself. Therefore, the formulation for the apse tolerance, ϵ_{apse}, in Equation (6.2) as the sine of the flight path angle is approximately equal to the flight path angle, and the apse tolerance holds the horizontal flight path angle to nearly ± 0.001 deg, as written in Table 6.9. Taken in combination, these constraints and tolerances are chosen to simulate a mission environment similar to EM-1.

Since the trajectory is thus far represented with impulsive velocity changes, additional work is required to generate a suitable initial guess for the TLT-LT corrections process. Since the burn durations are expected to be relatively short in relation to the total arc durations, the OPF, DRI, DRD, and RPF patch points are represented as split arcs, and the remaining patch points are modeled as coast segments. For the split arcs, the initial guess for the thrust magnitude parameter, $\gamma = 0.45\pi$, produces an initial guess for thrust, $\tilde{T} = 26.046604$ kN, that is near the maximum value but avoids the problem of thrust magnitude becoming fixed at $\gamma = 0.5\pi$ due to the sine-squared formulation for thrust defined in Equation (2.40). To calculate initial guesses for burn duration, a technique derived from the rocket equation is employed [10], i.e.,

$$t_{T,i} = \frac{m_i^+ I_{sp} g_0}{T_i^+} \left(1 - e^{\left(\frac{-\Delta v_i}{I_{sp} g_0} \right)} \right) + t_i \tag{6.3}$$

where Δv_i is the norm of the Delta-V vector,

$$\Delta \boldsymbol{v}_i = \boldsymbol{v}_i^+ - \boldsymbol{v}_i^- \tag{6.4}$$

which describes the instantaneous velocity change at a patch point in the impulsive reference trajectory. For simplicity, this investigation assumes $m_i^+ = 1$ as a reasonable approximation to calculate the initial guess for $t_{T,i}$ for all patch points. The burn durations, $\tilde{t}_{i,T} - \tilde{t}_i$, for the split arc segments are tablulated with their associated impulsive Delta-V values in Table 6.10. A higher fidelity initial guess would decrement mass as each burn duration and mass expenditure is calculated in series; however, this more advanced model is not found to be necessary for this investigation. The final thrust control parameters, angles α and β, are derived from the unit vector associated with each Δv_i. The in-plane angle relative to $\hat{\boldsymbol{x}}$ is used for α, and the

Table 6.10. Impulsive to Finite Duration Initial Guess

Manuever	Impulsive Delta-V, $\Delta\tilde{v}_i$	Burn Duration, $\tilde{t}_{i,T} - \tilde{t}_i$	Thrust, $\tilde{T}_i$
OPF	541.579 m/s	476.929 s	26.046604 kN
DRI	232.600 m/s	215.081 s	26.046604 kN
DRD	69.832 m/s	66.277 s	26.046604 kN
RPF	856.908 m/s	718.556 s	26.046604 kN

out-of-plane angle is supplied as an initial guess for β. Finally, the patch points are constructed such that the incoming velocity from the impulsive solution, $\boldsymbol{v}_i^-$, is used for the outgoing velocity, $\boldsymbol{v}_i^+$, in TLT-LT initial guess, ensuring that the thrust event is not counted twice, once as instantaneous and again in a finite duration.

The TLT-LT initial guess trajectory translated from the impulsive reference contains initial discontinuities and constraint violations that must be corrected. The initial guess, plotted in Figure 6.7, contains position and velocity discontinuities shown in Figures 6.8 and 6.9, respectively. For this initial guess, the maximum position and

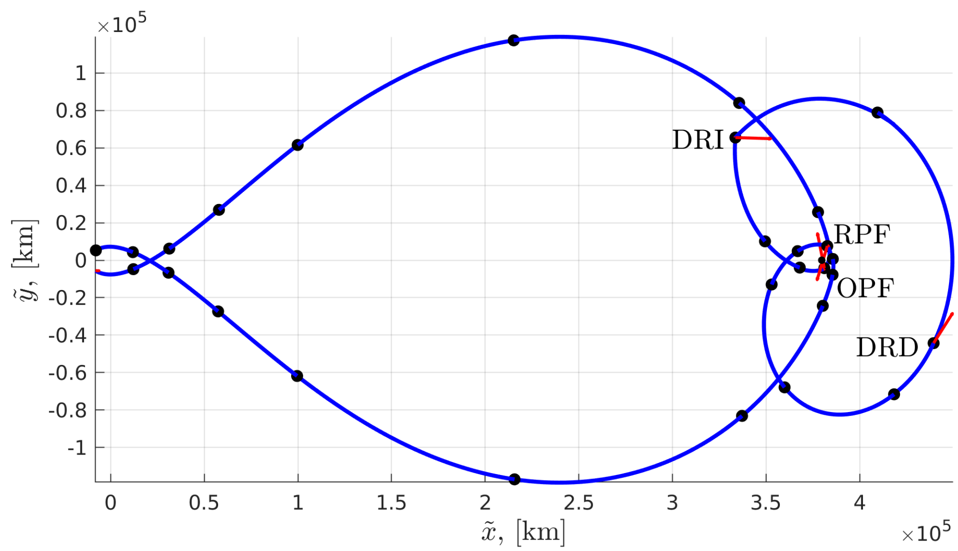

Figure 6.7. Unconverged EM-1 Initial Guess to the TLT-LT

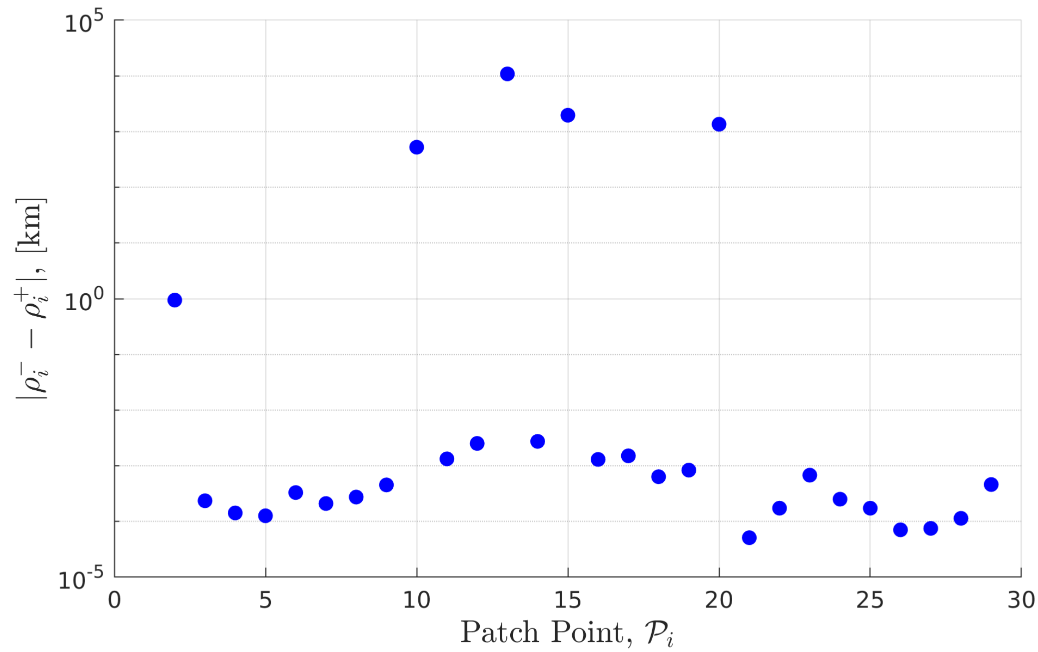

Figure 6.8. Norm of the Initial Position Discontinuity at Each Patch Point, $\mathcal{P}_i$, for the EM-1 Trajectory

velocity discontinuities are 10,868.336 km and 371.668 m/s, respectively, which represent substantial discontinuities in relation to the dynamical system's characteristic quantities.

Before executing the TLT-LT process in search of satsifactory solution, another assumption is applied to Level-I to aid in convergence. As shown in previous work by Scarritt, feeding forward velocity through a burn node helps improve convergence behavior for high-thrust examples, such as the EM-1 reference trajectory [9]. For this mission scenario, an option to override $\boldsymbol{v}_i^+$ with $\boldsymbol{v}_i^-$ at each split arc patch point is enabled and consistent with existing implementations of finite burn targeting algorithms for high-thrust applications [9].

After 6 iterations of the TLT-LT corrections procedure, a trajectory satisfying all interior continuity, boundary condition, and additional operational constraints to

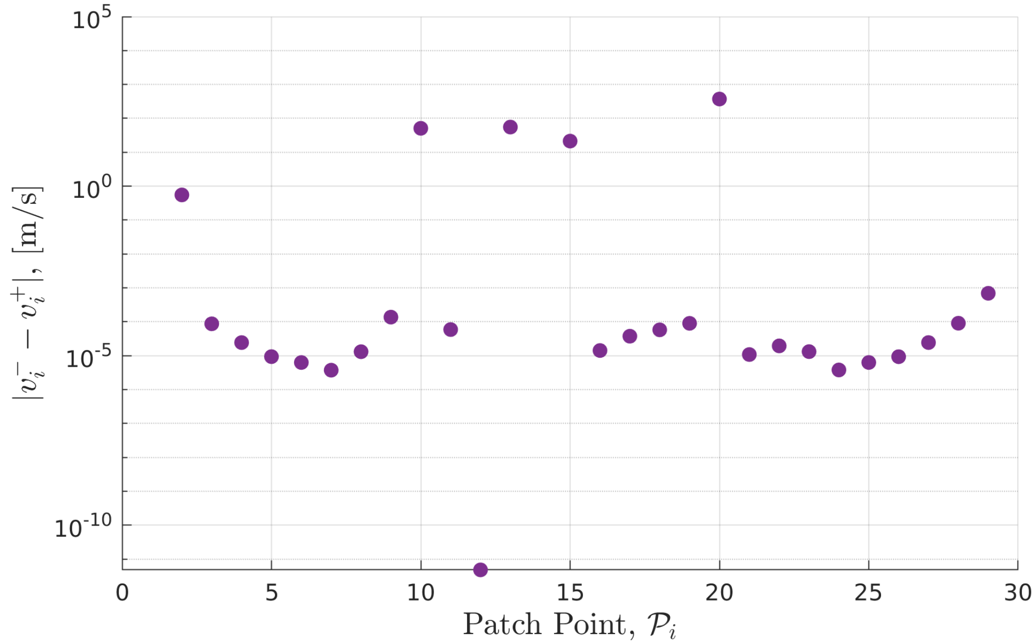

Figure 6.9. Norm of the Initial Velocity Discontinuity at Each Patch Point, $\mathcal{P}_i$, for the EM-1 Trajectory

within the tolerances in Table 6.9 is produced by the algorithm. The resulting trajectory, plotted in Figure 6.10, demonstrates the ability of the TLT-LT to correct trajectories for spacecraft with relatively high thrust magnitudes and low burn durations. Focusing on the area close to the Moon, Figure 6.11 illustrates the smooth, differentiable curve produced by the continuously-actuated thrust. The converged thrust magnitude and burn durations are recorded in Table 6.11 along with an additional performance metric for comparing impulsive and finite burn trajectories, equivalent Delta-V. Determined from the rocket equation, equivalent Delta-V, denoted $\Delta v_{i,eq}$, is a quantity analogous to impulsive Delta-V, defined in Equation (6.4), and is expressed as

$$\Delta v_{i,eq} = I_{sp} g_0 \ln\left(\frac{m_i^+}{m_{i+1}^-}\right) \tag{6.5}$$

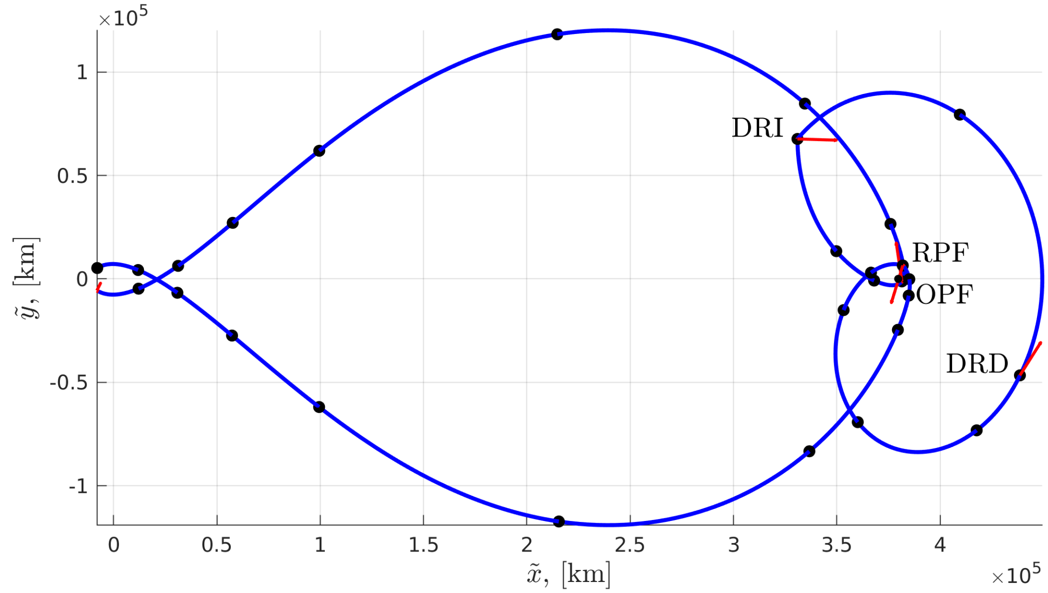

Figure 6.10. EM-1 Converged Trajectory

Table 6.11. EM-1 TLT-LT Converged Solution

Manuever	Equivalent Delta-V, $\Delta\tilde{v}_{i,eq}$	Burn Duration, $\tilde{t}_{i,T} - \tilde{t}_i$	Thrust, $\tilde{T}_i$
Post-TLI	19.833 m/s	90.045 s	5.488802 kN
OPF	260.211 m/s	237.990 s	26.050844 kN
DRI	280.794 m/s	235.398 s	26.046604 kN
DRD	82.277 m/s	65.030 s	26.046604 kN
RPF	836.244 m/s	571.624 s	26.046734 kN

Comparing the initial guess thrust parameters in Table 6.10 with the converged values in Table 6.11, the DRI and DRD values remain relatively similar while the OPF and RPF, which are located in regions of higher nonlinearity, see more drastic changes in thrust magnitude, duration, and equivalent Delta-V. This observation reflects the

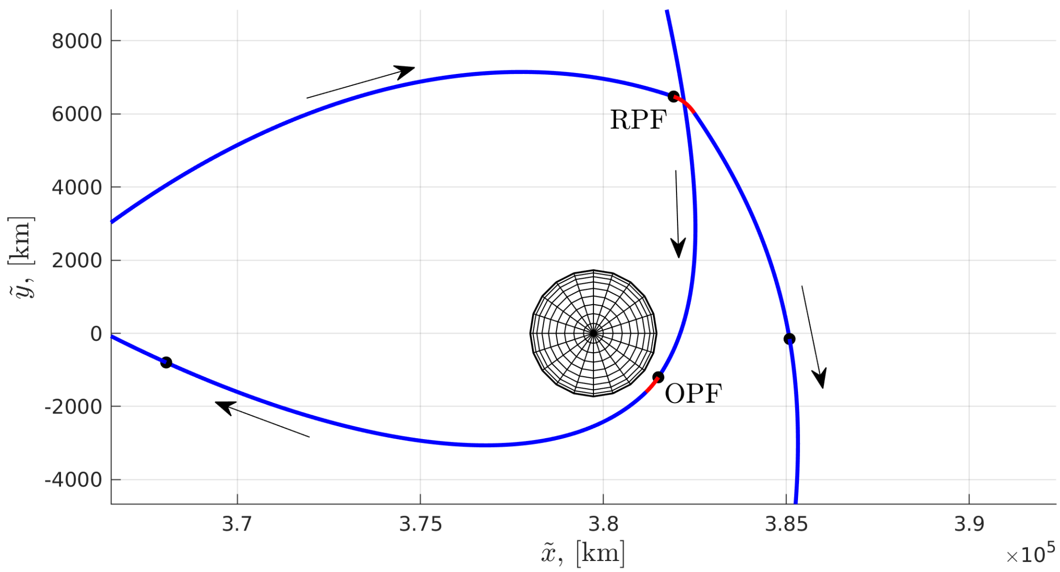

Figure 6.11. Smooth Trajectory in TLT-LT Corrected Solution

limited viability of using impulsive solutions as approximations of finite burn trajectories, especially in dynamically sensitive regimes.

The approximated EM-1 trajectory demonstrates the flexibility of the TLT-LT algorithm to correct nearly-impulsive trajectories in addition those with low thrust, such as the L_1-to-L_2 transfer. This application shows robustness to transitioning impulsive reference trajectories into successful initial guesses as well as the ability to implement constraints, e.g., altitude and apse, that are not satisfied by the reference solution.

6.3 Translunar Low-Thrust Continuation

To verify that the TLT-LT algorithm can successfully correct discontinuous trajectories that employ various levels of thrust magnitude, a family of solutions is produced from the EM-1 trajectory, detailed in the previous section, by incrementally lowering the maximum achieveable thrust, T_{max}, and increasing the engine specific impulse, I_{sp}, to transition the solution from a nearly-impuslive finite burn solution toward a more traditional low-thrust trajectory. In a dynamical system described by the same characteristic quantities in Table 6.6, the converged trajectory depicted in Figure 6.10 is used as the initial guess for the motion of a spacecraft with mass and engine parameters defined in Table 6.5. As T_{max} and I_{sp} are altered for each subsequent intermediate solution in the continuation process, the TLT-LT algorithm targets a solution which achieves position, velocity, and mass continuity at the interior patch points as well as fixed initial and final positions at the boundary conditions to within the tolerances outlined in Table 6.9.

When a solution is determined for a particular T_{max} and I_{sp}, the resulting patch points are used as the initial guess for the subsequent corrections following a change in T_{max} or I_{sp}. If the TLT-LT does not converge within 15 global iterations, adjustments to the patch points, including patch point removal and arc-type changes, are made to attempt to improve the likelihood of convergence. For example, if the TLT-LT fails to converge within 15 global iterations, a split arc consisting almost entirely of its thrust component may be converted to a thrust arc, and the corrections process is repeated. Since the objective of this work is to investigate the flexibilty of the TLT-LT algorithm to correct trajectories for a range of thrust magnitudes and to explore the utility of the three arc-type definitions, the process of generating and altering initial guesses is not explored in detail. However, a successful strategy for converting coast arcs to thrust or split arc types, as needed, is to replicate the thrust parameters of a neighboring thrust or split arc.

The transition from moving the thruster model from a chemical to low-thrust representation is completed by incrementing specific impulse and then decrementing thrust. First, the TLT-LT produces solutions as specific impulse is increased from 500 to 3,000 seconds in 500 second intervals. This change has the effect of decreasing the mass expenditure as the simulated propulsive element is modeled with higher mass efficiency, and the acceleration imparted on the spacecraft at later stages of the trajectory is lower due to the higher remaining mass. The number of iterations of the TLT-LT required to converge on a solution within the established tolerances for each specific impulse value is plotted in Figure 6.12. The differential corrections process

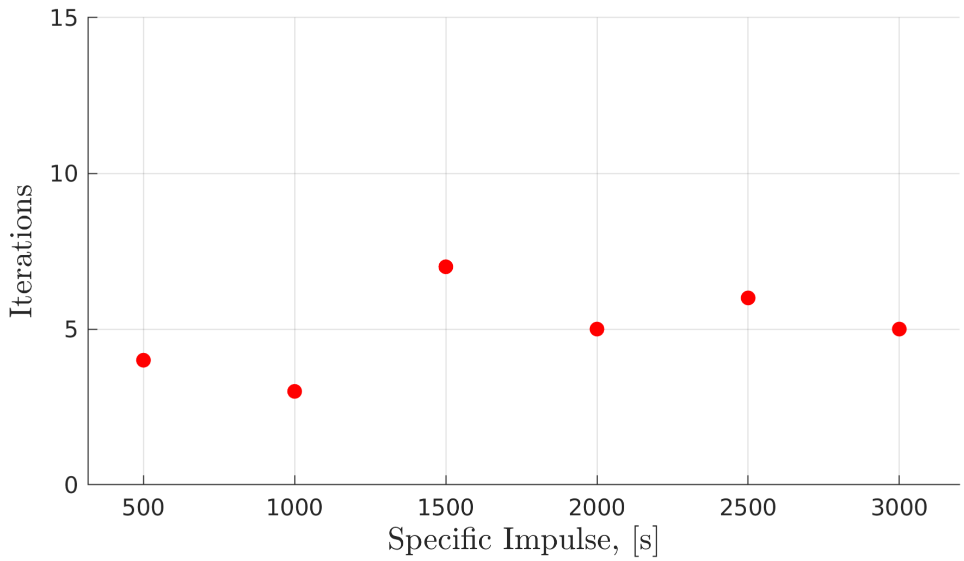

Figure 6.12. Relationship Between $\tilde{I}_{sp}$ Continuation and Number of Iterations for TLT-LT Convergence

takes between 3 and 7 iterations to determine a satisfactory solution, and the final converged trajectory with a specific impulse of 3,000 seconds is illustrated in Figure 6.13. Note the overall geometry of the trajectory appears relatively unchanged when compared to the reference trajectory, depicted in Figure 6.10, despite the fact that the spacecraft retains approximately 95.095% of its initial mass while the less-efficient reference retains only 62.041%. Overall, the increasing specific impulse in this way does not pose significant difficulty in determining a new solution with the TLT-LT.

With specific impulse held constant, the continuation process procedes by lowering the maximum thrust incrementally from 26.7 kN to 75 N. Through the case where $\tilde{T}_{max} = 1$ kN, shown in Figure 6.14, the thrust segments elongate as more time is required to achieve the same change in velocity; however, the geometry of the solutions remain similar, and the initial guess is only manually altered by removing

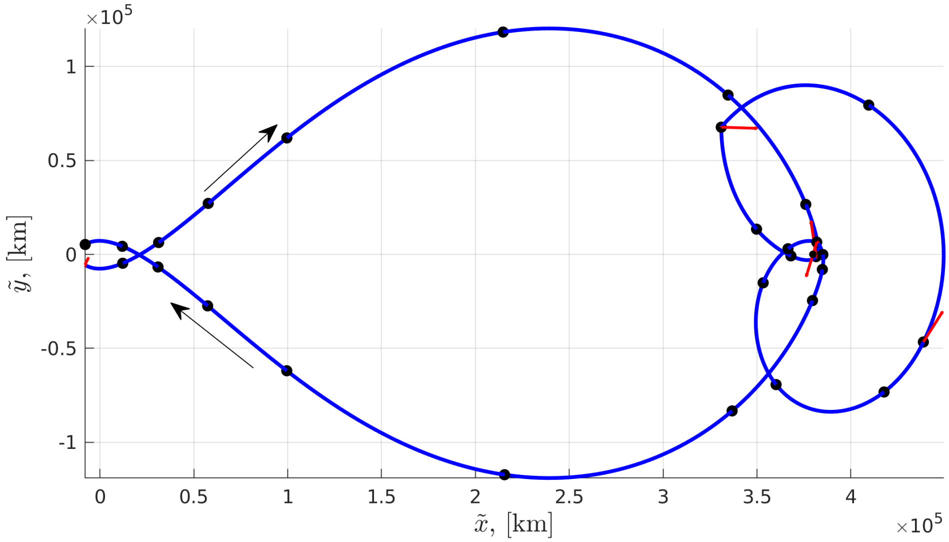

Figure 6.13. Converged Trajectory with $\tilde{T}_{max} = 26,700$ N and $\tilde{I}_{sp} = 3,000$ s

two coasting patch points. Represented in Figure 6.15, thrust is reduced significantly

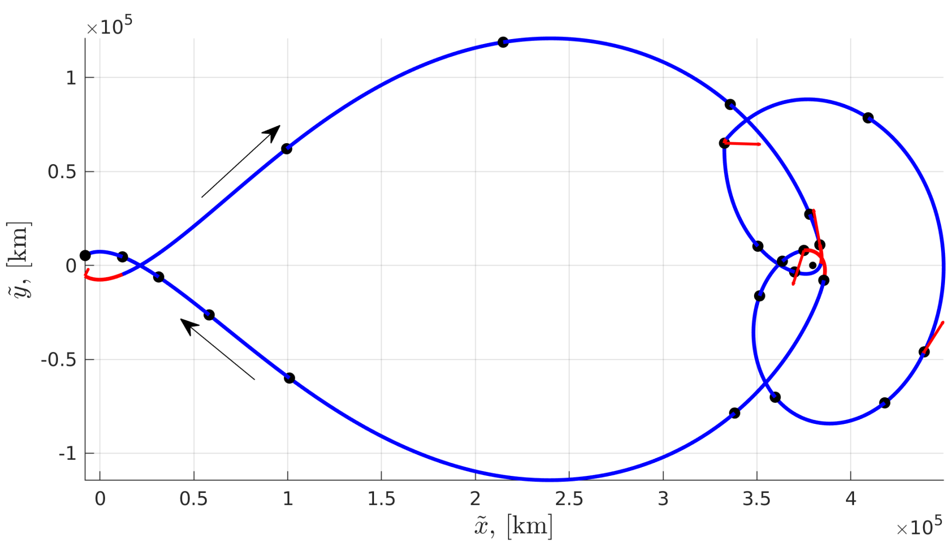

Figure 6.14. Converged Trajectory with $\tilde{T}_{max} = 1,000$ N and $\tilde{I}_{sp} = 3,000$ s

between the subsequent steps in the continuation process from 26.7 to 1 kN with generally consistent convergence behavior at around 5 iterations. However beyond

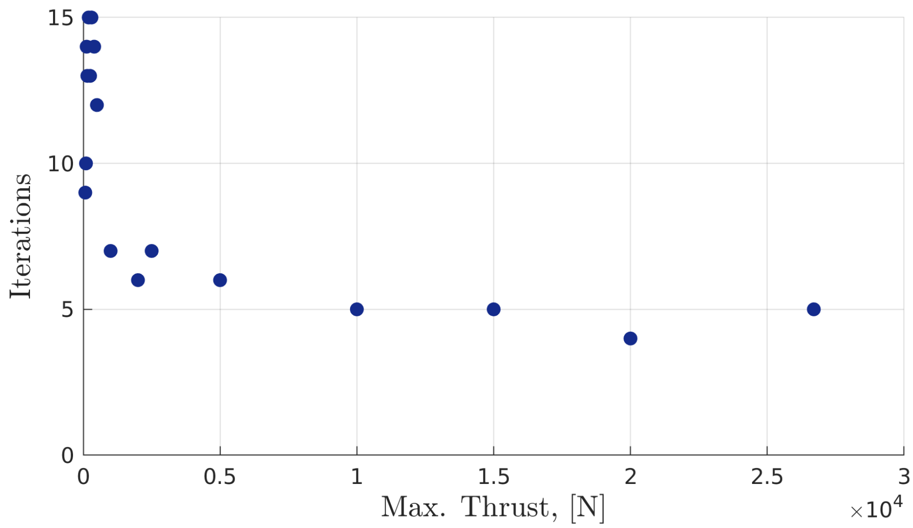

Figure 6.15. Relationship Between $\tilde{T}_{max}$ Continuation and Number of Iterations for TLT-LT Convergence

this threshold, the quality of the initial guess degrades substantially with fixed steps in thrust.

For continuation steps below 1 kN, a suitable continuation step size in thrust reduces drastically, and substantial work is required to manually adjust patch points, e.g., converting coast arcs to thrust and split arcs, to aid in convergence within the 15 iteration limit. Illustrated in Figures 6.16-6.18, the utility of employing combinations of thrust, coast, and split arcs is observed as the TLT-LT generates solutions for $\tilde{T}_{max} = 500$ N, 300 N, and 150 N. Decreasing $\tilde{T}_{max}$ further to 75 N, a 356-fold reduction from the original baseline solution, yields a solution, shown in Figure 6.19, whose form begins to deviate significantly from the EM-1 trajectory. The long time periods and low accelerations appear to be insufficient to maintain the original structure. Additional reduction in thrust requires reduced continuation step sizes and nontrivial alterations to the initial guess, signaling the continuation process is considered complete for this investigation.

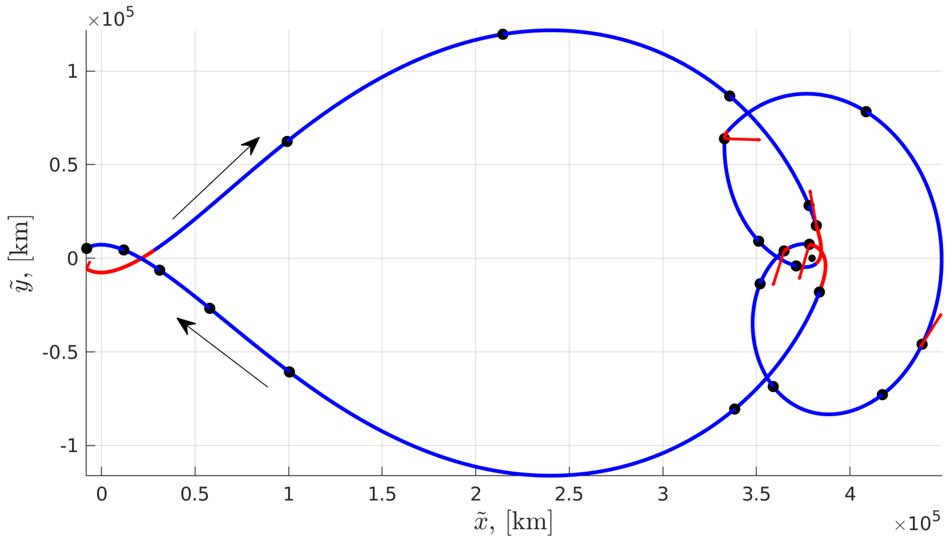

Figure 6.16. Converged Trajectory with $\tilde{T}_{max} = 500$ N and $\tilde{I}_{sp} = 3,000$ s

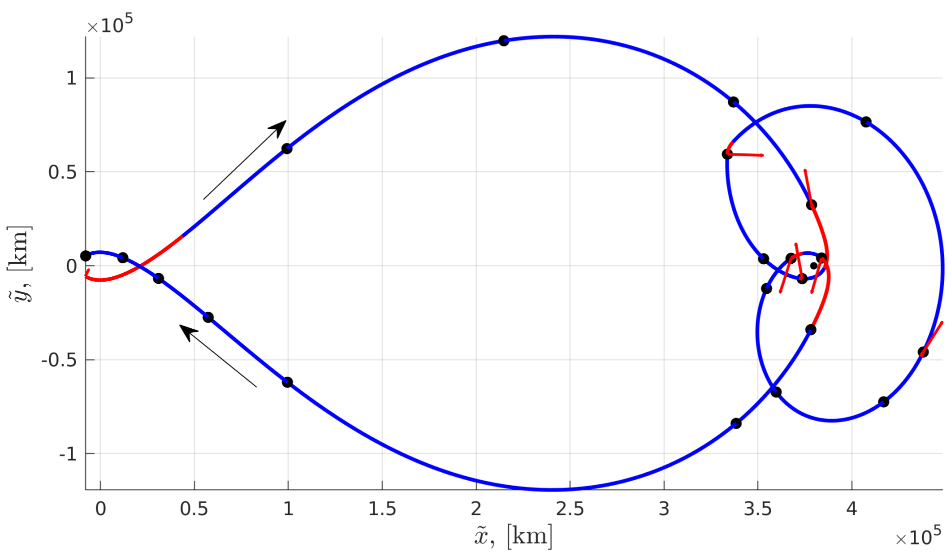

Figure 6.17. Converged Trajectory with $\tilde{T}_{max} = 300$ N and $\tilde{I}_{sp} = 3,000$ s

To understand the cause of difficulty in transitioning the EM-1 trajectory to maximum thrust values decreasing from 500 N to 75 N, the relationship between thrust

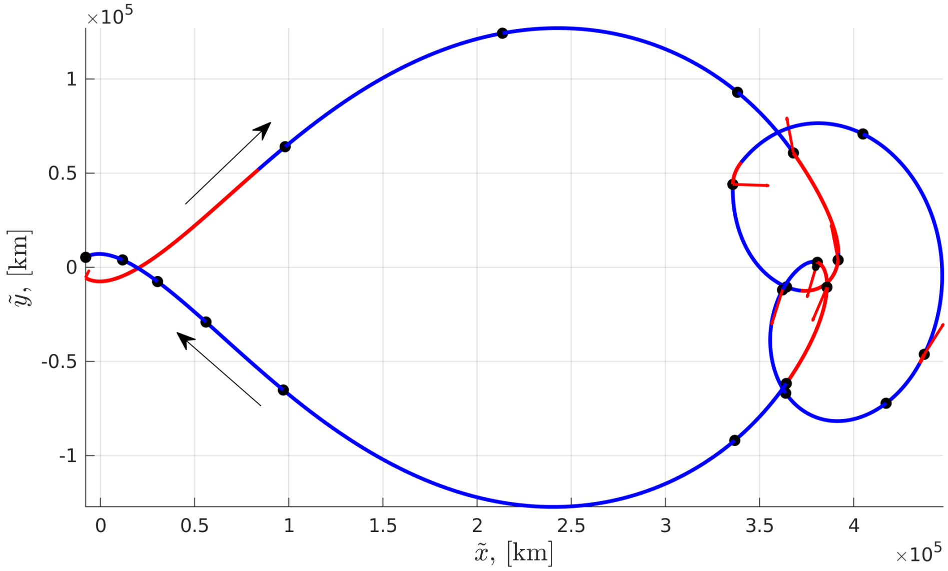

Figure 6.18. Converged Trajectory with $\tilde{T}_{max} = 150$ N and $\tilde{I}_{sp} = 3,000$ s

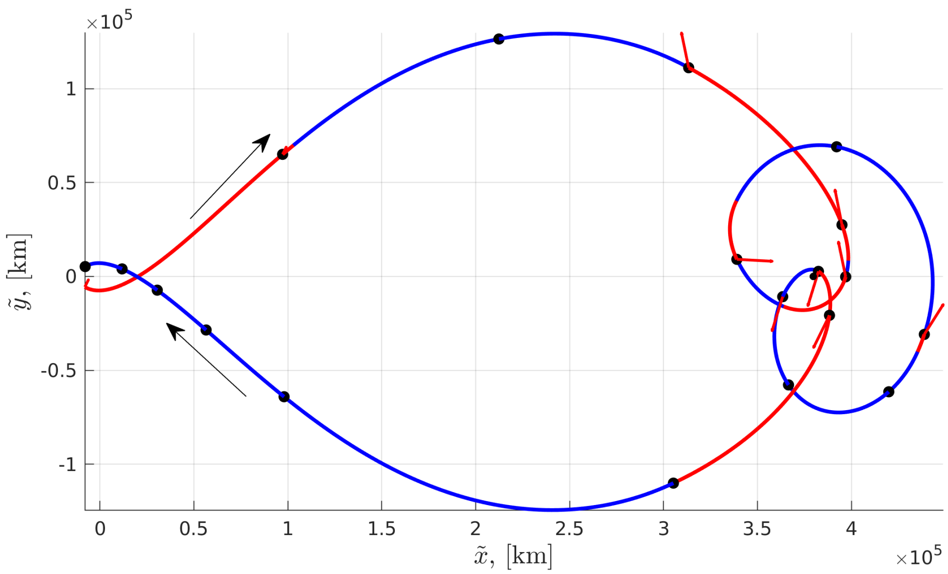

Figure 6.19. Converged Trajectory with $\tilde{T}_{max} = 75$ N and $\tilde{I}_{sp} = 3,000$ s

magnitude and burn duration is investigated. The total equivalent Delta-V, $\Delta v_{tot,eq}$, is defined as the sum of the magnitudes the equivalent Delta-Vs for each thrust subarc in a trajectory, i.e.,

$$\Delta v_{tot,eq} = \sum_{i=1}^{k-1} \Delta v_{i,eq} \tag{6.6}$$

Table 6.12 details selected thrust continuation solutions, the total equivalent Delta-V imparted by the thrust, and the number of TLT-LT iterations required to converge the constraints to within the specificed tolerances. As reflected in Table 6.12, $\Delta v_{tot,eq}$

Table 6.12. Equivalent Delta-V at Selected Thrust Values

Max. Thrust, $\tilde{T}_{max}$	Total Equivalent Delta-V, $\Delta v_{tot,eq}$	Iterations
26,700 N	1.479726 km/s	5
5,000 N	1.502419 km/s	6
2,000 N	1.534262 km/s	6
1,000 N	1.370538 km/s	7
500 N	1.297456 km/s	12
300 N	1.353982 km/s	15
200 N	1.476793 km/s	15
150 N	1.379078 km/s	13
125 N	1.408133 km/s	14
100 N	1.438329 km/s	10
75 N	1.606202 km/s	9

fluctuates but remains within ±15% of the baseline $\Delta v_{tot,eq}$ = 1.479360 km/s from the converged EM-1 trajectory in the previous example with $\tilde{I}_{sp}$ = 316 seconds and $\tilde{T}_{max}$ = 26.7 kN. Despite changing thrust and addition of burns along the trajectory, the velocity and energy changes to access and depart regions of the position and velocity space in the dynamical system remain constant, so the $\Delta v_{tot,eq}$ for each trajectory in the family of solutions remains relatively constant. As a rough approximation, an estimate of the time required to complete the velocity change in one continuous burn,

$t_{B,est}$, called the estimated total burn duration, is determined by dividing relating the approximate momentum change due to the thrust events by the force imparted by the propulsive element, mathematically expressed in terms of the non-dimensional quantities as

$$t_{B,est} = \frac{m_1^+ \Delta v_{tot,eq}}{T_{max}} \tag{6.7}$$

For this application, $\Delta v_{tot,eq}$ is assumed constant due to the minor fluctuations along the family of solutions. Additionally, the high I_{sp} values and corresponding low mass expenditure suggest that constant mass is a reasonable assumption. Therefore, $t_{B,est}$ is inversely proportional to T_{max}, and a graph of the two parameters produces the hyperbola displayed in Figure 6.20 with $\Delta v_{tot,eq} = 1.479360$ km/s, a constant equal to the original reference value. Approaching from the right, the slope of the curve begins

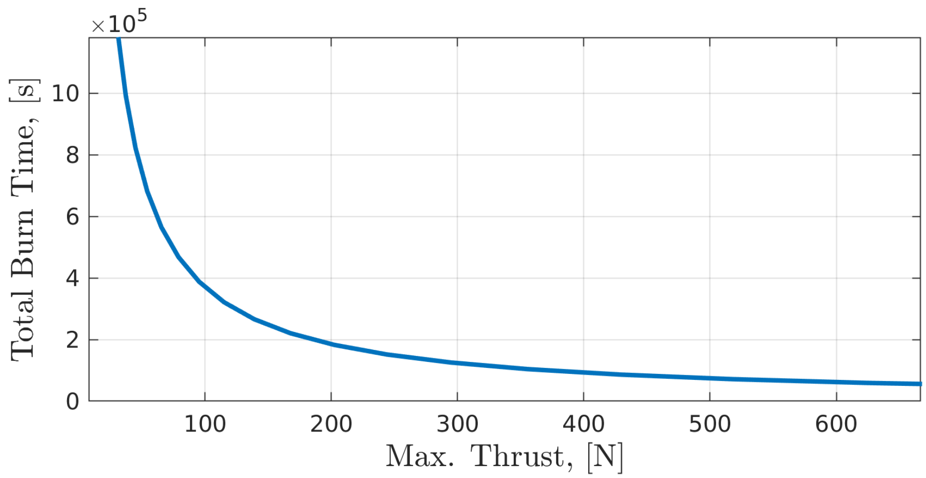

Figure 6.20. Estimated Total Burn Time

to increase as T_{max} reduces to the order of hundreds of Newtons, and the estimated total burn duration increases rapidly for small changes in thrust near 100 kN, similar to the onset of convergence issues in the continuation process. For high thrust values, the slope is relatively flat, signifying that large changes in thrust should produce small changes in the required burn times. This relationship translates directly to the effectiveness of using previously converged solutions at higher thrust values for initial guesses with lower thrust; rapid increases in burn duration correspond to poor initial guesses and less predictable impacts on the underlying dynamics. To confirm that estimated total burn duration is a meaningful calculation, the actual total burn duration, $t_{B,act}$, for a spacecraft along a trajectory, i.e.,

$$t_{B,act} = \sum_{i=1}^{k-1} t_{i,T} - t_i \tag{6.8}$$

is the total amount of time spent in thrust subarcs. Plotted on a log-log scale in Figure 6.21, the hyperbolic estimate and the actual total burn times have a strong correlation, despite the fact that $\Delta v_{tot,eq}$ and the number of burns varies for each actual total burn time. Note the analytic model for predicted values employs the total equivalent Delta-

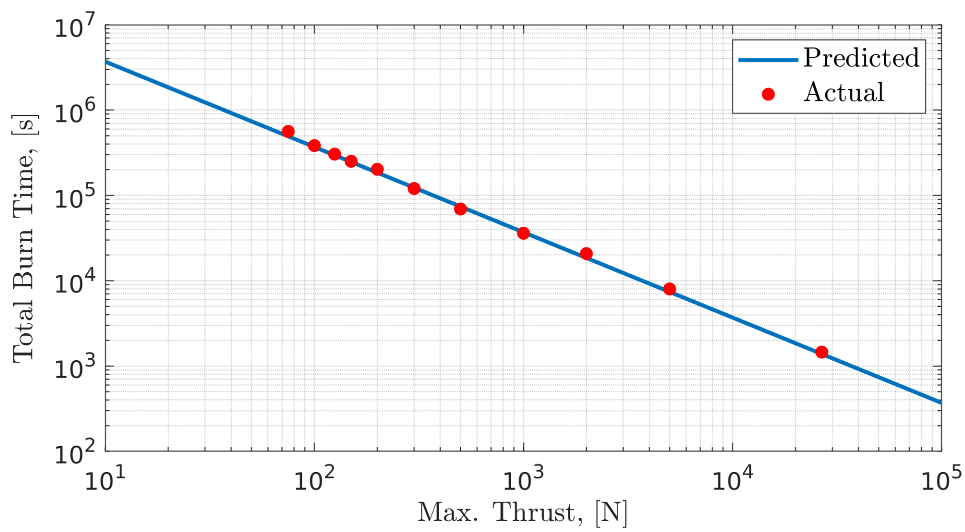

Figure 6.21. Log-Log Comparison of Predicted and Actual Total Burn Duration

V from the nearly-impulsive baseline trajectory and not the values for each individual converged value in the solution family. This result lends credibility to the attribution of changing convergence behavior and deviating trajectory geometry to the transition from flat to steep areas of the total burn time hyperbola.

If the degradation of the initial nearly-impulsive reference in generating progressive initial guesses with reduced thrust is correlated to the hyperbola defined in Equation (6.7), then the mathematical relationship may offer insight into a metric for approximating a boundary between traditionally low thrust and nearly-impulsive trajectories.

By differentiating Equation (6.7) with respect to T_{max}, an expression relating change in total burn time to maximum thrust is given by

$$\frac{\mathrm{d}t_{B,est}}{\mathrm{d}T_{max}} = \frac{-\Delta v_{tot,eq} m_1^+}{T_{max}^2} \tag{6.9}$$

In the non-dimensional system outlined in this mission scenario, the point where the hyperbola transitions from steep to flat, i.e., $\frac{\mathrm{d}t_{B,est}}{\mathrm{d}T_{max}} = -1$, corresponds with a dimensional thrust value of 85.478 N, which is very near the 75 N scenario that saw significant geometry change and difficulty in convergence. This investigation proposes further exploration of this mathematical relationship as potential future work.

7. Summary

7.1 Concluding Remarks

To support both the initial trajectory design and the autonomous path planning of spacecraft with a wide range of propulsive capabilities, this investigation derives and applies an extension of two-level targeting corrections that accommodates low-thrust considerations. The partial derivatives used in the variational mappings for the differential corrections are defined in a flexible way that captures trends in designing thrust, coast, and split segments for different applications, allowing the algorithm to compute suitable trajectories for a multitude of mission scenarios. The ability to vary or fix velocity in the Level-I process as well as to feed velocity forward across patch points are examples of mission-specific algorithm design options that allow the engineer to make trades between convergence behavior and design flexibility. Coupled with other tools at the trajectory designer's disposal, such as LLE-weighting and alternatives for dealing with chronological conflicts, this investigation presents an augmented two-level corrections framework that is intended to address the problems of low-thrust spaceflight in multi-body dynamical environments. Recognizing that the effectiveness of a differential corrections strategy strongly depends on the discontinuities and local dynamics of the initial guess, this investigation delivers examples of solutions converged by the TLT-LT for low-thrust motion near the L_1 and L_2 points and nearly-impulsive motion in cislunar space. Finally, the effect of continuing a family of trajectories with progressively decreasing thrust is characterized, and potential challenges in transitioning from high to low thrust are identified.

7.2 Recommendations for Future Work

While completing this research investigation, multiple potential avenues for future research are identified and listed as follows:

- Spacecraft attitude rate and throttling limits represent real constraints on the operability of a trajectory for a given spacecraft. Supplementation of the state vector with linear angular rates for thrust direction is explored by Scarritt for trajectories with short expected burn times [9]; however, opportunities exist to apply continuity constraints in thrust direction and magnitude at the patch points for long duration low-thrust burns. Additionally the arc-constant thrust magnitude assumption may be relaxed to explore the effect of the inclusion of linear throttling rates in the augmented state vector.

- Low-thrust spacecraft trajectories frequently operate with thrust directions and magnitudes that are a function of time as a result of direct and indirect optimization techniques [18]. The ability to incorporate the constraints and costates of indirect optimization in a multi-level targeting algorithm is a potential area of future research to better match the capabilities of the corrections strategy with trends in mission design.

- An increase in the fidelty of the low thrust engine model and expansion to include power output as a control for variable specific impulse engine (VSI) models is recommended as trends in low-thrust mission design increasingly incorporate VSI assumptions [18].

- Hyperbolic relationship between total burn time and thrust magnitude for an equivalent total momentum change demonstrated in Equation (6.7) correlates well with the onset of convergence difficulties and substantive geometry changes in the EM-1 thrust continuation example. Further research is recommended into the usefulness of the vertex of the hyperbola as a metric for the same behavior in other applications and, potentially, as a guiding metric for the transition between low-thrust versus nearly-impulsive characteristics.

REFERENCES

REFERENCES

[1] I. Newton. *The Principia: Mathematical Pricinciples of Natural Philosophy.* University of California Press, 1999. Translated by I. Bernard Cohen and Anne Whitman.

[2] J. Barrow-Green. Poincaré and the three body problem. In *History of Mathematics*, volume 11. American Mathematical Society, 1997.

[3] V. Szebehely. *Theory of Orbits: The Restricted Problem of Three Bodies.* Academic Press, New York and London, 1967.

[4] S. M. Roberts and J. S. Shipman. Continuation in shooting methods for two-point boundary value problems. *Journal of Mathematical Analysis and Applications*, Vol. 18 (No. 1):pp. 45–58, 1967.

[5] S. M. Roberts and J. S. Shipman. Justification for the continuation method in two-point boundary value problems. *Journal of Mathematical Analysis and Applications*, Vol. 21 (No. 1):pp. 23–30, 1968.

[6] H. B. Keller. *Numerical Solution of Two Point Boundary Value Problems.* SIAM, 1976.

[7] K. C. Howell and H. J. Pernicka. Numerical determination of lissajous trajectories in the restricted three-body problem. *Celestial Mechanics*, Vol. 41 (Nos. 1-4):pp. 107–124, 1988.

[8] B.G. Marchand, K. C. Howell, and R. S. Wilson. Improved corrections process for constrained trajectory design in the n-body problem. *Journal of Spacecraft and Rockets*, Vol. 44 (No. 4):pp. 884–897, 2007.

[9] S. K. Scarritt. *A Self-Contained Guidance and Targeting Algorithm for Spacecraft Applications.* PhD thesis, The University of Texas at Austin, 2012.

[10] S. K. Scarritt, B. G. Marchand, A. J. Brown, W. H. Tracy, and M.W. Weeks. A finite burn linear targeting algorithm for autonomous path planning and guidance. *Journal of Guidance, Control, and Dynamics*, Vol. 35 (No. 5):pp. 1605–1615, Sept.-Oct. 2012.

[11] G. Harden. Automated patch point placement for autonomous spacecraft trajectory targeting. Master's thesis, Purdue University, 2013.

[12] C. Spreen. *Automated Patch Point Placement Capability for Hybrid Trajectory Targeting.* PhD thesis, Purdue University, 2017.

[13] W. H. Press, S. A. Teukolsky, W. T. Vetterling, and B. P. Flannery. *Numerical Recipies in C: The Art of Scientific Computing.* Cambridge University Press, Cambridge, 2 edition, 1992.

[14] R Pritchett, E Zimovan, and K C Howell. Impulsive and low-thrust transfer design between stable and nearly stable periodic orbits in the restricted problem. *18th AIAA SciTech Forum*, 2018.

[15] B.G. Marchand, M. W. Weeks, C. W. Smith, and S. Scarritt. Onboard autonomous targeting for the trans-earth phase of orion. *Journal of Guidance, Control, and Dynamics*, Vol. 33 (No. 4):pp. 943–956, May-June 2010.

[16] B.G. Marchand, S. Scarritt, T. Pavlak, and K. C. Howell. Investigation of alternative return strategies for orion trans-earth injection design options. In *AAS/AIAA Space Flight Mechanics Meeting*, February 2010.

[17] T. F. Dawn, J. P. Gutkowski, A. L. Batcha, and S. M. Pedrotty. Trajectory design considerations for exploration mission 1. In *AAS/AIAA Space Flight Mechanics Meeting*, 2018.

[18] R. E. Pritchett. Numerical methods for low-thrust trajectory optimization. Master's thesis, Purdue University, 2016.